2016-01-01

Elucidating The Molecular Mechanism Of Action By Which RS1-208b Induces Apoptosis In Hematological Cancers

Ruben Israel Calderon
University of Texas at El Paso, ruben.israel.calderon@gmail.com

ELUCIDATING THE MOLECULAR MECHANISM OF ACTION BY WHICH RS1-208b INDUCES APOPTOSIS IN HEMATOLOGICAL CANCERS

RUBEN ISRAEL CALDERON

Master's Program in Biological Sciences

APPROVED:

Renato Aguilera, Ph.D., Chair

Giulio Francia, Ph.D.

Rachid Skouta, Ph.D.

Charles Ambler, Ph.D.
Dean of the Graduate School

Copyright ©

by

Ruben Israel Calderon

2016

Dedication

I dedicate this thesis to my parents.

ELUCIDATING THE MOLECULAR MECHANISM OF ACTION BY WHICH

RS1-208b INDUCES APOPTOSIS IN HEMATOLOGICAL CANCER

by

RUBEN ISRAEL CALDERON, B.A.

THESIS

Presented to the Faculty of the Graduate School of

The University of Texas at El Paso

in Partial Fulfillment

of the Requirements

for the Degree of

MASTER OF SCIENCE

Biological Sciences

THE UNIVERSITY OF TEXAS AT EL PASO

December 2016

Acknowledgements

Abstract

The 26S proteasome has been successfully targeted to treat multiple myeloma. However, the effect can sometimes be reversed as cells acquire resistance to chemotherapy. Recently, combining proteasome inhibitors with indirect proteasome inhibitors has been proposed in order to delay and even reverse resistance. Small molecules derived from 4-piperidinone that maintain an unsaturated β-carbonyl group are thought to interact with the thiol group of catalytically active cysteine residues in deubiquitinases that associate with the 26S proteasome, effectively inhibiting the proteasome.

RS1-208b was selected following a high-throughput screening of a small library of 4-piperidinone derived curcumin structural analogs due to its selectivity towards hematological cancers and its ability to inhibit inflammatory cytokine production. *In silico* docking experiments showed RS1-208b can inhibit cysteine deubiquitinases by bringing the unsaturated β-carbonyl in close proximity to the thiol group. AmpliSeq analysis revealed RS1-208b elicits a cellular response that is similar to that of proteasome inhibitors collected in the Connectivity Map. Treatment with RS1-208b leads to the rapid accumulation of poly-ubiquitinated proteins, which initiates a cellular response that culminates in cell death. RS1-208b up-regulated transcripts in the PERK-mediated unfolded protein response and the intrinsic pathway of apoptosis, which was verified using several fluorescence based assays. *In vivo,* RS1-208b delayed the tumor growth in RAMOS xenograft models and increased event-free survival time.

Table of Contents

List of Tables

List of Figures

List of Illustrations

1. Introduction

1.1 Cancer World Wide

Cancer refers to a group of diseases characterized by the dysregulation of pathways that control proliferation and subsequent invasion of abnormal cells, which can lead to death. Cancer is responsible for more deaths worldwide than AIDS, tuberculosis, and malaria combined, accounting for an estimated 8.2 million deaths in 2012[1]. The death estimate is expected to reach 13 million by the year 2030[1]. Moreover, the majority of the expected new cases (rising to 21.7 million world-wide by 2030) will occur in developing countries[1], where access to adequate medical care is limited, further driving health outcome disparities.

1.2 Childhood Cancer World Wide and in the U.S.

World-wide, leukemia and lymphoma account for the majority of childhood cancer cases[1]. Cancer in children and adolescents is rare, though it is one of the leading causes of death in children in developed countries[1], where incidence rates are higher than in developing countries[2]. However, mortality rates in developed countries are substantially lower than in developing countries[2], presumably due to access to medical care.

Leukemia is the most common childhood cancer world-wide, and accounts for about one third of all childhood cancer, with acute lymphoblastic leukemia (ALL) accounting for, roughly, 83% of all pediatric leukemia cases[1,3]. Non-Hodgkin's Lymphoma (NHL) is the third most common childhood cancer across all demographics in the U.S., though in the continent of Africa, it is the most common childhood cancer in the form of Burkitt's Lymphoma (BL)[1].

Developing countries do not generally invest resources into childhood cancer treatment[1] since other public health concerns, such as combating infectious diseases, are prioritized. In these

1

countries, as the number of deaths due to preventable diseases decreases, childhood cancers will emerge as one of the leading causes of death[1]. Furthermore, health outcomes appear to be more successful when treatment is managed by a children oncology specialist at a children's cancer center[1], suggesting an important role for medical infrastructure in determining availability of effective treatment and, ultimately, patient outcomes.

However, even in the U.S., outcome disparities between socio-economic and ethnic groups is observed[3,4], highlighting a need to improve the medical infrastructure world-wide to increase access to adequate medical care. In addition, it is important to note that even when access to chemotherapy is controlled in clinical trials, health disparities (between Hispanic and non-Hispanic White children in the U.S.) are readily observed[3], suggesting access to treatment will not be sufficient to improve outcomes around the world. Investment in basic research and clinical trials to target those populations who are not well served by the current standard of care for these childhood cancers. In Texas, the East and West parts of the state are roughly equally distributed (covering 50.9% and 49.1%, respectively), with East Texas containing 88.8% of the population and West Texas containing 11.2%[4] and childhood cancer incidences reflect the population distribution, with East Texas seeing 90.9% of pediatric cancer patients compared to 9.1% in West Texas[4]. Yet West Texas experiences 14.6% pediatric cancer patient mortality, roughly 1.5 times the mortality rate observed in East Texas[4]. And the difference in outcomes can be partially attributed to the disparities in number of pediatric oncologist (4.2% available in West Texas), the number of NCI-designated cancer centers (0 in West Texas, 4 in East Texas), and total grant funding (NCI, DOD, CPRIT) per person: $3.40 in West Texas compared to $35.50 in East Texas[4].

1.3 Hispanics in the U.S. and Childhood Cancer

The Hispanic population is the fastest growing demographic in the United States, growing by 43% between 2000 and 2010, four times the growth rate of the total population[3]. However, the distribution of the Hispanic population in the U.S. is not homogenously distributed, concentrated in the south western part of the country, along the U.S.-Mexico border. Among the general U.S. Hispanic population, cancer is the leading cause of death[3], having surpassed cardiovascular disease.

Hispanic children developing cancer in 2012 accounted for 2% of the new cases of cancer in the U.S. Hispanic population, compared to childhood cancers accounting for <1% of the total new cancer cases in the U.S. population[3]. Though this discrepancy might be accounted for by the difference in age demographics between the Hispanic and total U.S. population, Hispanic children have the highest incidence rates of ALL of any demographic in the U.S[3]. In addition, Hispanic children with ALL have higher mortality rates compared to non-Hispanic White children and African American children[3], and despite the similarity in the incidence rates for lymphoma between Hispanic children and non-Hispanic White children, survival rates for Hispanic children are markedly lower[3].

1.4 Standard of Care for Childhood Cancers

The past 30 years have witnessed many advances in cancer treatment and early detection which have combined to greatly improve health outcomes, as measured by the increase in 5 year survival rates[1,3]. However, for Hispanic children in the U.S., 5-year survival rates are statistically significantly below those of non-Hispanic White children for all childhood cancers combined[3]. One of the most dramatic differences in both incidence and survival rates between Hispanic and non-Hispanic children is observed in ALL. A possible explanation for this disparity

3

in both incidence rates and outcomes could be attributed to socio-economical differences that impede or restrict access to appropriate screening and medical treatment[1,4]. In Texas, for example, there are 4 NCI-designated cancer centers, but they are all concentrated in East Texas[4]. In order for a West Texas child to receive the same medical treatment as a child from East Texas, s/he would have to travel, possibly as much as 746 miles (from El Paso, TX to Houston, TX). Although improving access to adequate medical care has been correlated with improved survival rates world-wide[1], differences in survival rates between Hispanic and non-Hispanic white children are also apparent in some clinical trials where all patients receive equal treatment, suggesting the observed disparity in survival rates is also, partially, due to a disproportional number of high risk leukemia cases developing in Hispanic children[3] and that the currently accepted standard of care for these patients are simply not as effective.

Current treatment options approved by the U.S. Food and Drug Administration for both childhood leukemia and Non-Hodgkin's lymphoma may lead to acute and long term, unwanted side effects[5]. Chemotherapeutic regiments for leukemia and non-Hodgkin's lymphoma typically include the topoisomerase II inhibitor Doxorubicin, which has been shown to be effective against most hematological malignancies[6]; however, its use has been associated with myocardial tissue damage, which can lead to fatal congestive heart failure[7].

Considering the age distribution of the Hispanic population in the U.S., and the continued expected growth, safer, more effective treatments need to be developed in order to fight childhood cancer along the U.S.-Mexico border.

1.5 Curcumin Promises
Curcumin [1,7-bis(4 hydroxy-3-methoxyphenyl)-1E,6E-heptadiene-3,5-dione] is the most abundant curcuminoid derived from the rhizomes of the south Asian plant *Curcuma longa*[8]. It

4

has been used in Chinese and Indian traditional medicine for many centuries to treat a variety of illnesses and ailments including infections, burns, and certain diseases[8,9]. Curcumin has been described as having antioxidant, anti-microbial, anti-inflammatory, and anti-cancer properties. Research into curcumin over the past few decades has revealed it to be a pleiotropic molecule, capable of modulating a broad range of cell signaling pathways[8,10–13].

Many molecular targets of curcumin in a variety of cancer cell lines have been proposed and studied over the years. *In vitro*, curcumin has shown the potential to influence a wide range of cell signaling pathways through its antioxidant[12], anti-inflammatory[14], antiproliferative and proapoptotic properties[15], most notably the modulation of the p53 pathway, NF-kB pathway, MAPK pathway, Akt pathway, as well as JAK/STAT pathway [8,11,13,16].

In vitro, curcumin has been shown to selectively induce apoptosis in cancer cell, whereas non-cancerous cells treated with similar concentrations of curcumin remain unaffected[9,17]. Furthermore, in vivo studies using curcumin to treat mouse models bearing cancer have indicated curcumin is very well tolerated and does not induce the toxic effects normally associated with conventional chemotherapy[18]. There have been several clinical trials assessing the tolerance and efficacy of curcumin using doses as high as 12g per day with only mild side effects[19–21]. Curcumin has been shown to display protective effects, especially of the liver and kidney tissue[22,23], of organs heavily involved in chemotherapy metabolism and generally affected by harsh treatments. The selectivity, safety of consumption, and systemic protective effects make curcumin a viable candidate for chemotherapy option either as stand-alone therapy or as part of a chemotherapeutic regiment. However, despite its many promises, curcumin is not an approved treatment for cancer[10] and remains a poor option for chemotherapy, in large part owing to its bioavailability[19].

1.6 Curcumin Limitations

Turmeric has been a staple ingredient in Indian cuisine for many centuries, and thus, has been consumed on a regular basis by people in South Asia. In the clinical setting, no detrimental effects were reported in a dose escalating study where subjects consumed up to 12g of curcumin per day, with effective doses reported between 100mg-6g per day (reviewed in[19–21]).

Despite the low systemic toxicity[14,24] and encouraging *in vitro* results against a wide variety of cancers[12,15,17], bioavailability remains the biggest challenge to using curcumin as an effective alternative to current chemotherapy treatment options. Curcumin's poor absorption, rapid metabolism, and the rate at which it is systematically eliminated all contribute to its limited bioavailability[19].

Consistently low serum, plasma, and tissue concentrations of curcumin have been observed despite high doses of curcumin administered, with peak levels being reached by 1 hour, followed by rapid systemic clearance (reviewed in [19,20,25]). Oral delivery of curcumin has shown the lowest plasma concentrations. However, intraperitoneal or intravenous delivery only appears to marginally improve plasma concentrations[19].

There have been several approaches taken to increase curcumin's efficacy *in vivo* and improve its bioavailability[19]. The most frequently reported are delivery methods using either nanoparticles[20,25–27], liposomes, or phospholipid complexes and the synthesis of structural analogs[28–31]. Improving the delivery method through novel formulations using nanoparticles or liposomes could improve the permeability of curcumin and protect it from being metabolized into inactive metabolites, thereby increasing bioavailability. However, structural analogs of curcumin synthesized from 4-piperidinone have been previously reported to exert stronger cytotoxic effects *in vitro* and *in vivo* compared to curcumin, improved solubility, and are being evaluated in clinical trials for improved bioavailability and efficacy[28–35].

6

1.7 Structural Analogs of Curcumin

Curcumin's chemical structure is an important aspect in its ability to regulate and target a large variety of molecules[32]. The synthesis of structural analogs of curcumin has provided compounds with improved cytotoxic profiles and bioavailability[28–31,36,37]. Analysis of structure-activity relationships of curcumin analogs has identified the α,β-unsaturated ketone moiety as the most important property that confers cytotoxicity to these structural analogs[32].

The modulation of pathways exerted by curcumin that lead to cell death are thought to occur through molecular interactions involving its α,β-unsaturated di-ketone moiety[32]. Conjugated enones can act as Michael acceptors in a Michael reaction[38], allowing a strong nucleophile to attack the β-carbon. Thiols appear to be the preferred nucleophiles for a Michael reaction involving the α,β-unsaturated di-ketone moiety of curcumin, with early research focusing on curcumin's ability to induce cell death by inhibiting glutathione[32].

The hepta-carbon backbone of curcumin is shortened in mono-ketone structural analogs of curcumin that have been synthesized from 4-piperidinone, and the α,β-unsaturated di-ketone moiety of curcumin has been reduced to an α,β-unsaturated ketone moiety. Curcumin is a highly hydrophobic compound with poor water solubility that exhibits pH dependent keto-enol taumerism, being found predominantly in the keto form at neutral and acidic conditions, and in its enol form in alkaline conditions[11]. The 4-piperidinone synthesized structural analogs of curcumin have a nitrogen atom on the ring which contains the ketone, which, along with generally more numerous or stronger election withdrawing groups on the aromatic rings, increases the stability of the compound, shifting the keto-enol taumerism balance towards the keto side, and, thus, helping stabilize the α,β-unsaturated moiety and increasing the β-carbon's reactivity. Evaluation of these structural analogs has consistently shown increased cytotoxicity profiles compared to curcumin,

7

as well as improved solubility[29,30,37], suggesting the structural analogs have the potential to be better therapeutic options.

1.8 Research Rationale

Though survival rates for the most common childhood cancers have steadily increased across all demographics over the past few decades[1,3], the discrepancy in survival rates between Hispanic and non-Hispanic white children highlights the need for developing novel chemotherapy options for the high-risk cases of Hispanic children. Structural analogs of curcumin previously characterized in our laboratory indicated that these compounds have improved cytotoxicity profiles (compared to curcumin) and appear to selectively affect leukemia and lymphoma *in vitro*[28]. Despite clinical trials being out of the scope of this thesis project, we do hope to draw attention to the potential benefits of utilizing structural analogs of curcumin against hematological cancers by elucidating the molecular mechanism of action by which they induce programmed cell death.

8

2. High-Throughput Screening of a Library of Compounds on a Panel of Cancer Cell Lines

2.1 Initial Screening of Library of Compounds on Jurkat and Nalm-6

Initial screening of the library of curcumin analogs (Figure 1.) was performed by MTS (3-(4,5-dimethylthiazol-2-yl)-5-(3-carboxymethoxyphenyl)-2-(4-sulfophenyl)-2H-tetrazolium, inner salt) on two leukemia cell lines: Jurkat (T-cell ALL) and Nalm-6 (pre-B cell ALL). Cells were seeded at 10,000 cells/100μL/well in a 96-well plate and treated with 5-fold dilutions of the compounds (1μM, 0.2μM, 0.04μM) for 24 hours (biological replicates = 3). The MTS was added (20μL/well) at 20 hours and incubated for 4 hours. The plate was read using a spectrophotometer, subtracting the absorbance of 650nm wavelength from the 490nm wavelength, using complete media with MTS as the blank. Positive and negative controls (hydrogen peroxide treated and untreated wells, respectively) were included in a 96-well plate; the results were normalized to vehicle (DMSO) treated absorbance values in order to assess cell viability after 24-hour treatment. The results (normalized to the vehicle control, DMSO) of the assay are summarized in Table 1. IC_{50} values for the library of compounds over 1μM were extrapolated from available data. For reference, Curcumin and EF-24 IC_{50} values are included in the table. The concentrations tested for the reference compounds were 25μM, 12.5μM, and 6.25μM for Curcumin, and 1μM, 0.2μM, and 0.04μM for EF-24. EF-24, a structural analog of curcumin synthesized from 4-piperidinone, has shown great efficacy in treating cancer both *in vitro* and *in vivo*[32–34,39].

The MTS assay, which is a colorimetric assay, makes use of a tetrazolium compound that, in the presence of phenazine methosulfate (PMS), is reduced to form a soluble, colored formazan product in biologically active cells[40]. Though it is unclear whether the reduction is accomplished by NADPH or NADH[41], the formation of the formazan product and appreciable

9

color change in the media measures the metabolic activity and the reduction potential of

mitochondrial dehydrogenases maintained by viable cells.
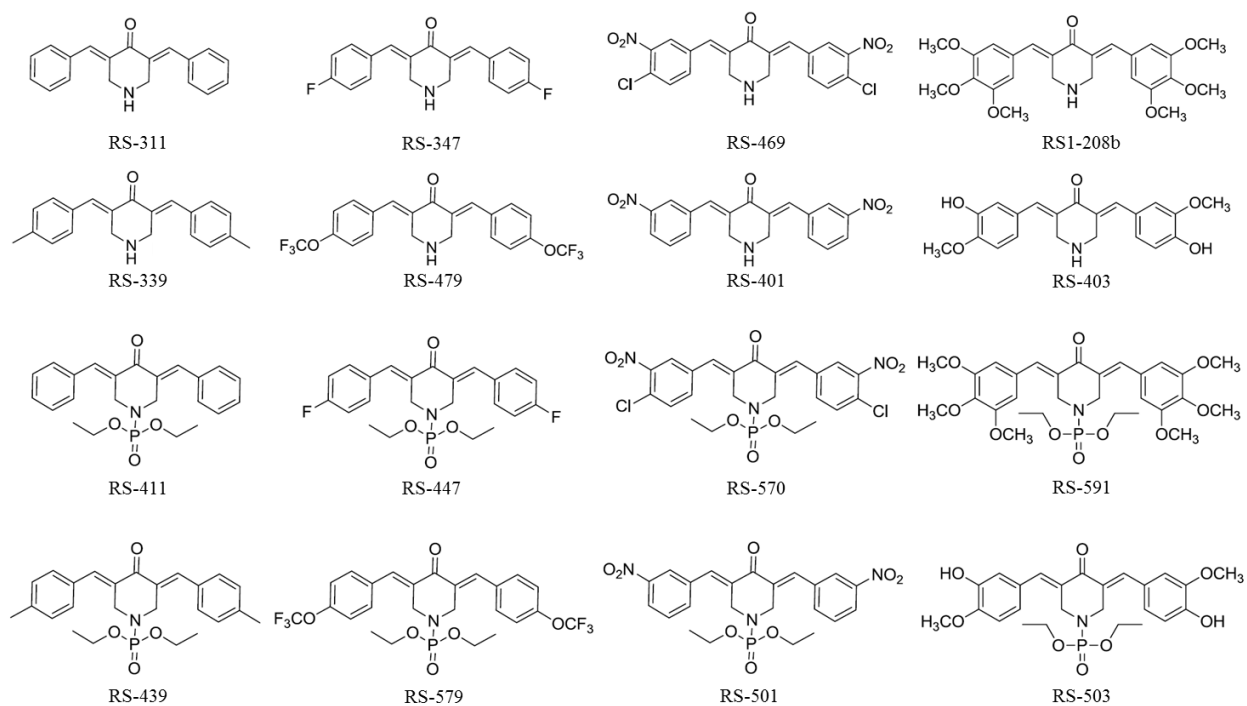
Figure 1. Library of Curcumin Analogs

Table 1. IC$_{50}$ Values Following 24 Hours of Treatment Obtained by MTS

Compound	Jurkat IC$_{50}$ (μM)	Nalm-6 IC$_{50}$ (μM)
RS-311	0.69 ± 0.07	0.62 ± 0.05
RS-347	0.17 ± 0.01	0.18 ± 0.04
RS-469	0.19 ± 0.02	0.19 ± 0.03
RS1-208b	0.17 ± 0.01	0.18 ± 0.07
RS-339	0.94 ± 0.10	1.26 ± 0.44
RS-479	0.66 ± 0.16	0.39 ± 0.06
RS-401	0.52 ± 0.31	0.15 ± 0.03
RS-403	1.57 ± 0.15	2.17 ± 1.21
RS-411	0.83 ± 0.26	0.79 ± 0.12
RS-447	0.75 ± 0.08	0.73 ± 0.02
RS-570	0.41 ± 0.20	0.29 ± 0.04
RS-591	0.77 ± 0.02	0.66 ± 0.04
RS-439	6.05 ± 6.06	29.25 ± 26.22
RS-579	0.78 ± 0.01	0.64 ± 0.04
RS-501	0.61 ± 0.19	0.16 ± 0.02
RS-503	5.84 ± 0.01	6.47 ± 0.56
EF-24	0.69 ± 0.07	0.78 ± 0.02
Curcumin	10.47 ± 2.76	14.12 ± 6.03

RS-347, RS-469, and RS1-208b we found to be the most biologically active compounds of the library tested, with IC$_{50}$ values of 0.17 ± 0.01, 0.19 ± 0.02, and 0.17 ± 0.01, respectively; though it is important to note that the majority of the functional group modifications made to the aromatic rings yielded IC$_{50}$ values below 1μM in the initial screening. With one exception in the Nalm-6 cell line, the IC$_{50}$ values of the library of compounds were significantly lower than Curcumin's ($p < 0.05$). Furthermore, the majority of the compounds screened on these two cell lines had standard deviations of the IC$_{50}$ values that overlapped the IC$_{50}$ of the reference drug, EF-24, indicating that in Jurkat and Nalm-6 cell lines, they were equally as effective

2.2 RS1-208b Against a Panel of Hematological Cancer Cell Lines

RS1-208b was selected from the library of compounds tested, and 1.5g was synthesized to provide enough compound to perform additional *in vitro* and *in vivo* assays, due to its low IC$_{50}$

11

values on both Jurkat and Nalm-6 cell lines, but also because the structure (synthesized and tested independently) has shown inhibition against IL-6 production[29] and thought to be an anti-inflammatory agent that could be used in combination therapy. Moreover, the compound was shown to protect mice from LPS-induced septic death[29]. The compound was then re-evaluated through MTS on a panel of hematological cancer cell lines, as well as two non-cancerous cell lines and PBMCs (see Table 2.). Cell density was adjusted to 200,000 cells/mL due to the minimum number of cells needed to extract sufficient RNA for sequencing, and maintained constant throughout the remaining *in vitro* experiments, unless explicitly stated otherwise. Five 5-fold dilutions (25μM, 5μM, 1μM, 0.2μM, 0.04μM) of RS1-208b were tested on the panel of cell lines. The IC_{50} values (normalized to DMSO) following 24 hours of treatment are summarized in Table 2. Burkitt's lymphoma (BJAB and RAMOS) was the disease most sensitive to RS1-208b, followed by ALL (CCRF-CEM, Jurkat, and Nalm-6), and AML (HL-60). Hs27, MCF-10A, and PBMCs were used as non-cancerous control cell lines.

Table 2. RS1-208b IC_{50} Values of a Panel of Cell Lines Following 24 Hours of Treatment

Cell Line	Cell Type	Disease	IC_{50} (μM)	SI	Age	Ethnicity	Sex
BJAB	B Lymphocyte	Burkitt's Lymphoma	0.29 ± 0.02	18.07	5	African	F
CCRF-CEM	T Lymphoblast	Acute Lymphoblastic Leukemia	0.33 ± 0.01	15.88	4	Caucasian	F
HL-60	Promyoblast	Acute Myelocytic Leukemia	0.52 ± 0.06	10.08	36	Caucasian	F
Hs27	Fibroblast	None	6.24 ± 0.99	-	Newborn	Black	M
Jurkat	T Lymphocyte	Acute Lymphocytic Leukemia	0.27 ± 0.03	19.41	14	-	M
MCF10-A	Epithelial	Fibrocystic Disease	8.76 ± 1.14	-	36	Caucasian	F
Nalm-6	pre-B cell	Acute Lymphoblastic Leukemia	0.36 ± 0.02	14.56	19	-	M
PBMC	PBMC	None	0.71 ± 0.11	-	-	-	-
RAMOS	B Lymphocyte	Burkitt's Lymphoma	0.23 ± 0.01	22.78	3	Caucasian	M

The selectivity index reported in Table 2. was calculated as SI = (Average IC_{50} of non-cancerous lines)/(IC_{50} value of the cell line)[28]. Selectivity index values above 1 indicate that a compound selectively inhibits half of the cells of a particular cancer cell lines at a concentration

12

that is lower than the concentration which inhibits half of the cells of non-cancerous cell lines. This provided a rationale for moving forward with RS1-208b to assays aimed at identifying its molecular mechanism of action and *in vivo* studies since, at most biologically achievable plasma concentrations (based on available curcumin data[19]), the compound is more likely to affect rapidly dividing cancer cells but not the majority of somatic cells.

2.3 RS1-208b Against a Panel of Adherent Cancerous Cell Lines

RS1-208b was also evaluated against a panel of adherent cancer cell lines (breast cancer cell lines: EMT-6, HCC-1419, MCF-7, MDA-MB-231, MDA-MB-231-LM2, MDA-MB-468, T47-D; colorectal cancer cell line: COLO-205; non-cancerous cell lines: Hs27, MCF-10A), though at the concentrations evaluated (up to 25µM) the majority of the cell lines did not reach an IC_{50} value after 24 hours of treatment. Therefore, the time point for evaluation of IC_{50} values through MTS for this panel of cell lines was extended to 72 hours. The results are summarized in Table 3 (normalized to DMSO).

Table 3. RS1-208b IC_{50} Values on a Panel of Adherent Cell Lines Following 72 Hours of Treatment

Cell Line	Disease	IC_{50} (µM)	Selectivity Index
Hs27	None	0.59 ± 0.01	-
COLO-205	Colorectal Cancer	0.50 ± 0.26	1.42
EMT-6	Breast Cancer	0.56 ± 0.02	1.27
HCC-1419	Breast Cancer	$0.91^{¥}$	0.78
MCF-7	Breast Cancer	0.58 ± 0.03	1.22
MCF-10A	Fibrocystic Disease	0.83 ± 0.02	-
MDA-MB-231	Breast Cancer	0.47 ± 0.13	1.51
MDA-MB-231-LM2	Breast Cancer	0.48 ± 0.04	1.48
MDA-MB-468	Breast Cancer	0.33 ± 0.1	2.15
T47-D	Breast Cancer	$0.87^{¥}$	0.82

¥standard deviations not available

13

Though the majority of the breast cancer cell lines and the one colorectal cancer cell line tested had selective indices above 1, the selectivity was not as pronounced as with the leukemia and lymphoma cell lines. Taken together, the data indicates that RS1-208b is selective against cancer cell lines, but more precisely, it displays stronger selection and sensitivity (low IC_{50} values) against leukemia and lymphoma cancer cells.

14

3. Evaluating Activity of RS1-208b on Hematological Cancers

3.1 Assessment of Cytotoxicity Induced by RS1-208b

The MTS is an assay that has been optimized for high-throughput screening, as it is able to quickly evaluate whether or not compounds in question have an effect on cells. However, the results obtained are relative to the vehicle control and the assay itself only detects a colorimetric difference that is produces by the reduction of the tetrazolium compound. Because of this, the MTS assay is not able to differentiate between compounds that cause cell cycle arrest and cytotoxic compounds that induce cell death.

Therefore, to verify that treatment of cells with the compound resulted in cell death, we investigated the cytotoxicity induced by RS1-208b on select, hematological cancer cell lines CCRF-CEM, HL-60, Jurkat, and RAMOS. RAMOS was the most sensitive cell line to RS1-208b in the panel and we had successfully grown a subcutaneous xenograft tumor in a mouse model. Jurkat and CCRF-CEM were selected due to the low IC_{50} values, and to provide experimental data that RS1-208b could also be used against ALL, the most common childhood cancer. The AML cell line HL-60 was evaluated because it is one of the original cell lines in the panel from which the Broad Institute developed the Connectivity Map[42], a resource that helps elucidate the mechanism of action of any particular compound by comparing its molecular signature against those collected from well-known anti-cancer compounds.

Cytotoxicity was detected with the Propidium Iodide Exclusion Assay, which makes use of a fluorescent dye that intercalates double stranded nucleic acids of dead or dying cells. Propidium Iodide (PI), intercalates DNA and double stranded RNA segments, with little sequence preference, at every 4-5 base pairs[43]. The dye is impermeable to viable cells with intact membranes; however, upon death, the membrane becomes permeabilized and PI is able to intercalate previously inaccessible double stranded nucleotides[43].

15

For this assay, 200,000 cells/mL/well were incubated in a 24-well plate (biological

replicates = 3) and treated with 0.5µM, 1µM, and 2µM of RS1-208b for 24 hours. Also included

in the plate were hydrogen peroxide treatments (positive control), untreated cells (negative

control, and vehicle treated cells (for this assay, PEG-400 was used as the vehicle). Following

incubation, 500µL of each well were removed from the plate and placed into a 5mL culture tube

along with 5µL of PI dye. The tubes were incubated in the dark at room temperature for 5

minutes then analyzed via flow cytometry using a 488nm[43] OPSL Sapphire laser to excite the

fluorescent dye. The emission wavelength of PI was detected through the FL2 channel. We

interpret the percentage of the cell population fluorescing red as having compromised cell

membranes, and therefore, equivalent to percentage of cell death. Below are graphical

representations of the data acquired for the Propidium Iodide Exclusion Assay.
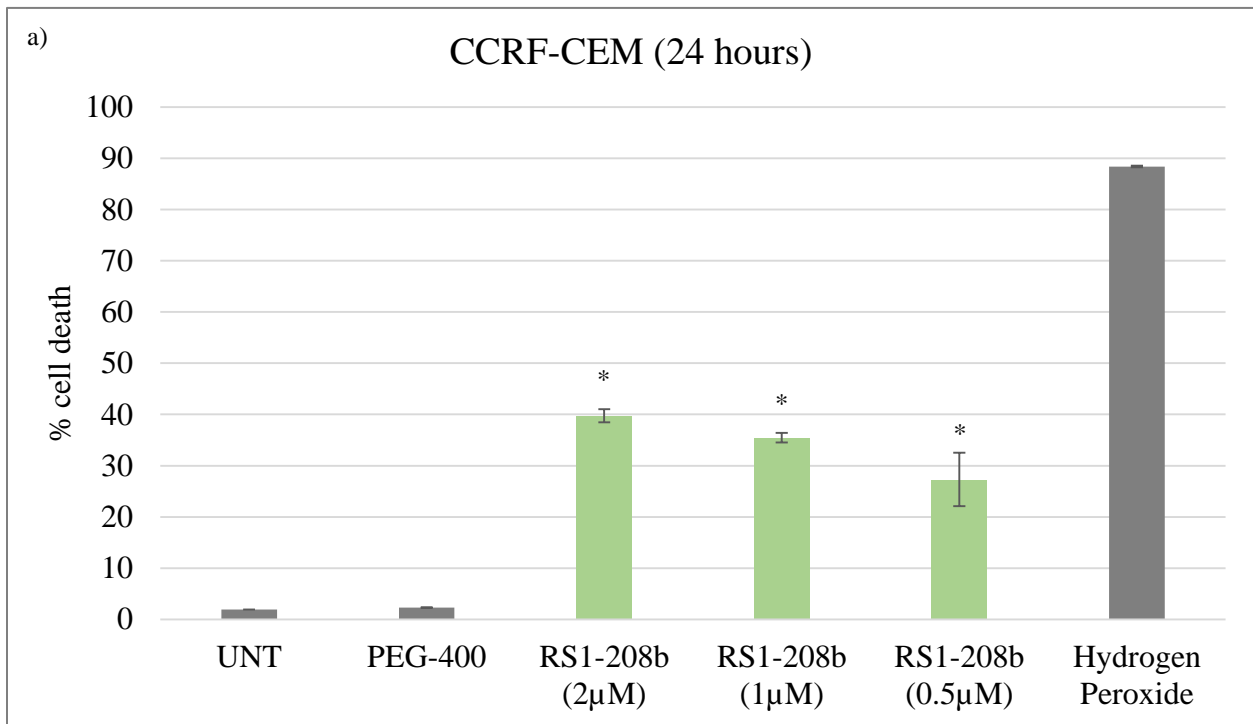
Figure 2. RS1-208b Induces Cell Death in Hematological Cancer Cells
a) Average values (± standard deviation) of percentage of CCRF-CEM cells stained with PI are summarized above.
Three different concentrations (doubling dilutions) were tested ($p < 0.05$). Cytotoxicity in response to RS1-208b was
concentration dependent in the CCRF-CEM cell line.

المنارة للاستشارات

www.manaraa.com
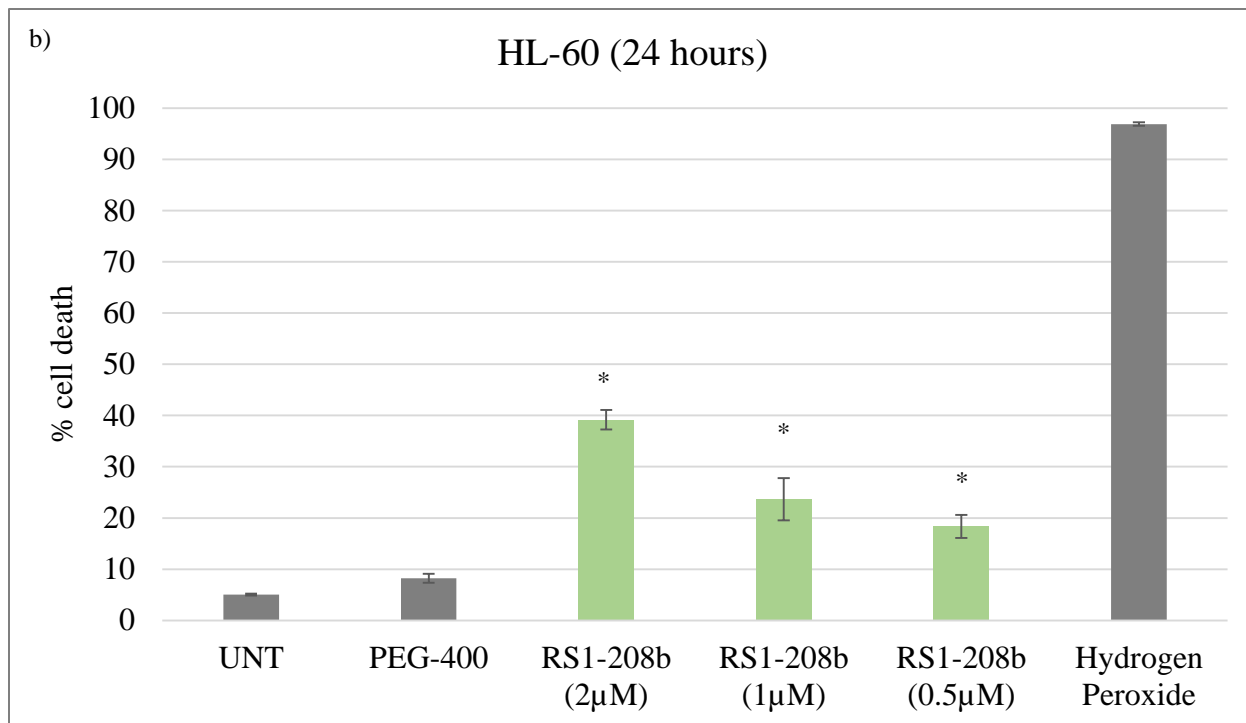
b) Average values (± standard deviation) of percentage of HL-60 cells stained with PI are summarized above. Three different concentrations (doubling dilutions) were tested ($p < 0.05$). Cytotoxicity in response to RS1-208b was concentration dependent in the HL-60 cell line.
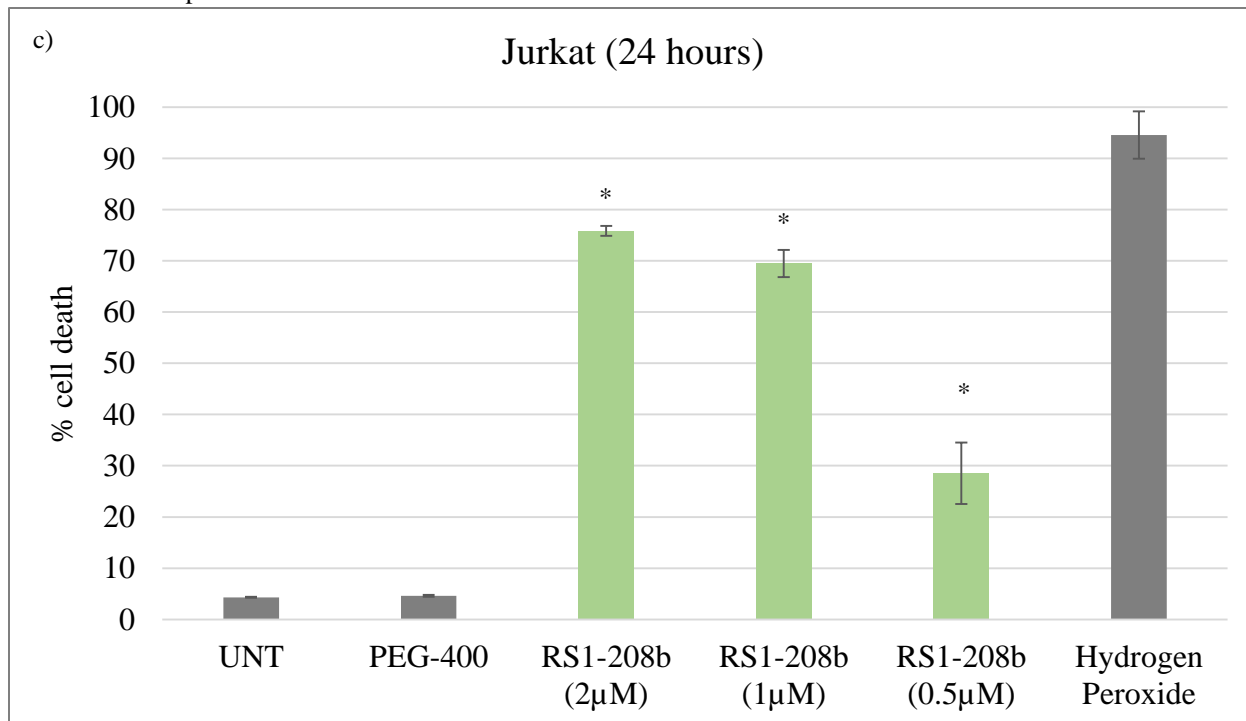
c) Average values (± standard deviation) of percentage of Jurkat cells stained with PI are summarized above. Three different concentrations (doubling dilutions) were tested ($p < 0.05$). Cytotoxicity in response to RS1-208b was concentration dependent in the Jurkat cell line.

RAMOS (24 hours)
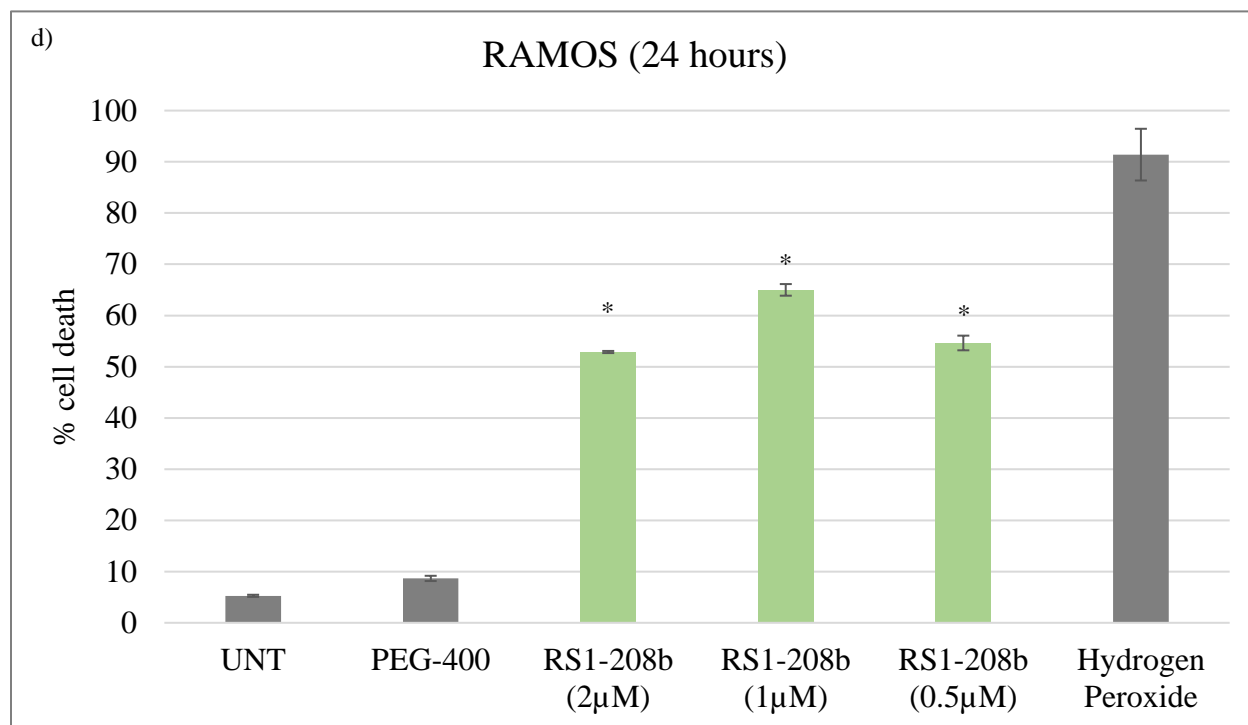
d) Average values (± standard deviation) of percentage of Jurkat cells stained with PI are summarized above. Three different concentrations (doubling dilutions) were tested ($p < 0.05$). Cytotoxicity in response to RS1-208b was concentration dependent in the RAMOS cell line.

Cytotoxicity induced by RS1-208b was observed across all the cell lines and concentrations tested ($p < 0.05$). Unlike the MTS assay, the PI assay does not normalize the results to the vehicle control. Furthermore, the PI assay interrogates individual cells in the population to assess the percentage of cells that have undergone RS1-208b induced cell death, as opposed to comparing the reduction potential of a population of cells. However, the results confirmed the concentration dependent effect observed by MTS (data not shown) and pointed to cytotoxicity as the main effect induced by RS1-208b in hematological cancers.

3.2 Assessment of the Effect RS1-208b Has on the Cell Cycle

Due to the slight disagreement between IC_{50} values obtained through MTS and the calculated concentration needed to induce cytotoxicity in half of the population of cells, we used the cell cycle assay to determine whether, apart from inducing cell death, RS1-208b caused cell

cycle arrest. An arrest in the cell cycle could reconcile the difference in concentration needed to inhibit half the cell population and that needed to kill half the population. Moreover, with this assay, if RS1-208b caused cell cycle arrest, it would be possible to narrow down molecular targets by focusing our attention on the events required to pass the checkpoint of the phase in the cell cycle at which the cell is halted.

An arrest in cell cycle is generally observed as a result of DNA damage[44], where the cell experiencing the damage initiates a cascade of events in an attempt to repair the damage (though compounds can have an effect on other intracellular targets that will result in cell cycle arrest). When the damage is irreversible, the cell can initiate programmed cell death through apoptosis.

The cell cycle assay determines the percentage of cells in an asynchronous population found at each stage of the cell cycle based on DNA content. As a cell progresses through the cell cycle, its DNA content increases accordingly. A daughter cell begins to increase its DNA content in the synthesis phase of the cell cycle so that by the time the cell reaches the G2 phase, there is double the amount of DNA inside the membrane of the cell than there was at the G1 phase. One of the hallmarks of apoptosis is DNA fragmentation and the formation of apoptotic bodies[44,45], membrane bound remnants of a complete cell that encapsulate fragments of the cellular contents of the original cell. Therefore, the cell cycle assay provides experimental data about which phase of the cell cycle a particular compound interferes with, while also providing some evidence of whether RS1-208b induces cell death through apoptosis.

For this assay, we opted for staining with DAPI (4',6-diamidino-2-phenylindole, dihydrochloride), as opposed to PI, effectively avoiding treatment with an RNase, thereby speeding up the procedure. DAPI is a membrane impermeable dye that intercalates AT rich

sequences, intercalating DNA but not RNA, which does not contain thymine[43]. The detergent NP-40 permeabilizes the cell membrane and allows for the intercalation of DAPI to the DNA.

Cells were seeded at 200,000 cells/mL/well in 24-well plates and treated with RS1-208b for 24 hours. Hydrogen peroxide, untreated cells, and DMSO treated cells were included as positive, negative, and vehicle controls, respectively. Following 24 hours of treatment, cells were collected in a 5mL culture tube and centrifuged for 5 minutes at 1200rpm. The supernatant was decanted and the cell pellet re-suspended in 200µL of the NIM-DAPI solution. The tubes were incubated for 5 minutes in the dark at room temperature then 300µL PBS was added to each tube prior to reading by flow cytometry equipped with a 405nm Solid-State Violet Diode laser to excite DAPI and the emission was detected through the FL9 channel. Below are graphical representations of the histograms obtained. G0/G1 represents diploid cells (2n); S represents cells undergoing DNA synthesis (2n-4n); G2/M represents tetraploid cells (4n); and <G0/G1 represents apoptotic bodies containing fragments of DNA.

Curcumin and some of its structural analogs have been reported to induce cell cycle arrest at the G2/M phase[31,33]. RS1-208b shows no appreciable arrest at the G2/M phase, compared to vehicle. However, there is a significant ($p < 0.05$) increase in the <G0/G1 phase in the RS1-208b treated cells, and a significant ($p = 0.05$) decrease in the G0/G1 phase, compared to vehicle. Given the rapid replication rates of the cell lines used for this assay, it is possible that the time point selected masks the effect on the cell cycle the compounds has on these cell lines. An earlier time point might demonstrate an arrest at the G2/M phase due to the effect of the compound, and if the damage induced by the compound is irreparable, the arrested cells initiate apoptosis, which we are able to detect at 24 hours.

20

CCRF-CEM Cell Cycle (24 hours)

■ <G0/G1 ■ G0/G1 ■ S ■ G2/M

a)

Hydrogen Peroxide

RS1-208b (0.35µM)   *

RS1-208b (1µM)   *

DMSO

UNT

0   20   40   60   80   100

% of cell population
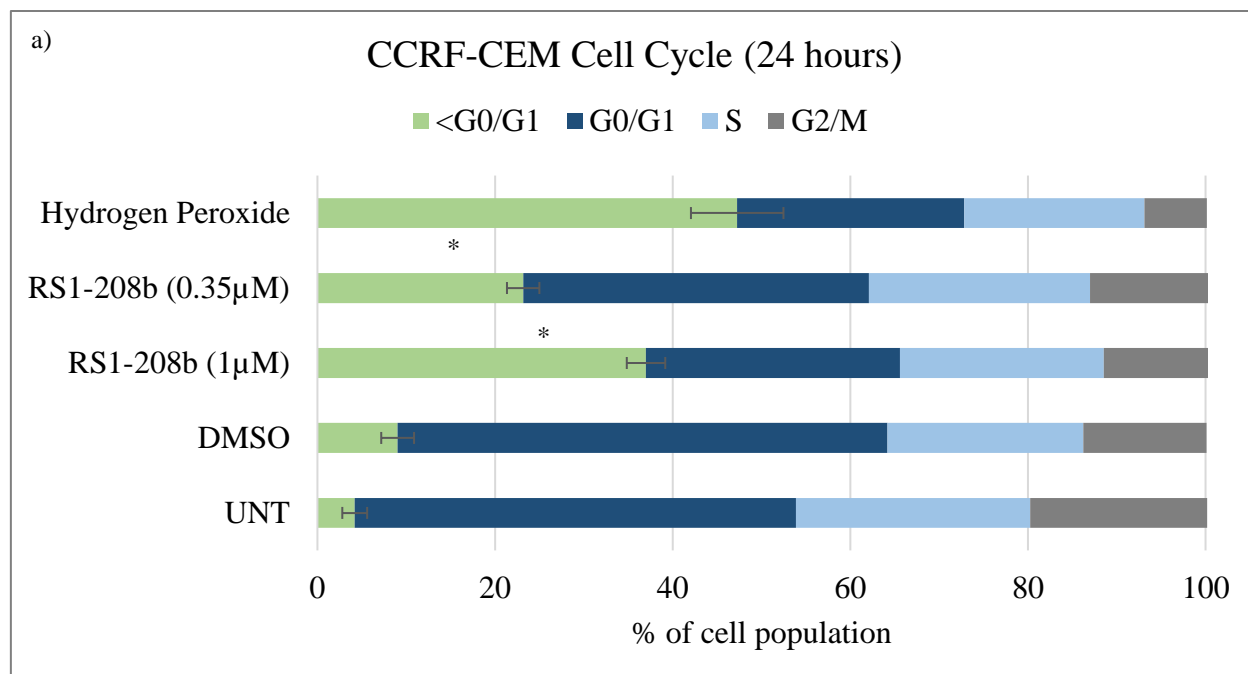
Figure 3. RS1-208b Does Not Induce Cell Cycle Arrest

a) Bar graphs represent average values (biological replicates = 3) of histograms. The <G0/G1 in RS1-208b treated cells was significantly higher than the DMSO control, indicating that the compound induces apoptosis in CCRF-CEM cells after 24 hours of treatment. The G0/G1 peak was significantly smaller ($p < 0.05$) in the RS1-208b treated cells than DMSO control, suggesting that cells did not re-enter the cell cycle following mitosis. The percentage of cells in the S phase and G2/M phase was similar between RS1-208b treated cells and DMSO control. Standard deviations were included for the <G0/G1 peak.

HL-60 Cell Cycle (24 hours)

b)

■ <G0/G1 ■ G0/G1 ■ S ■ G2/M

Hydrogen Peroxide

RS1-208b (2µM)   *

DMSO

UNT

0   10   20   30   40   50   60   70   80   90   100

% of cell population
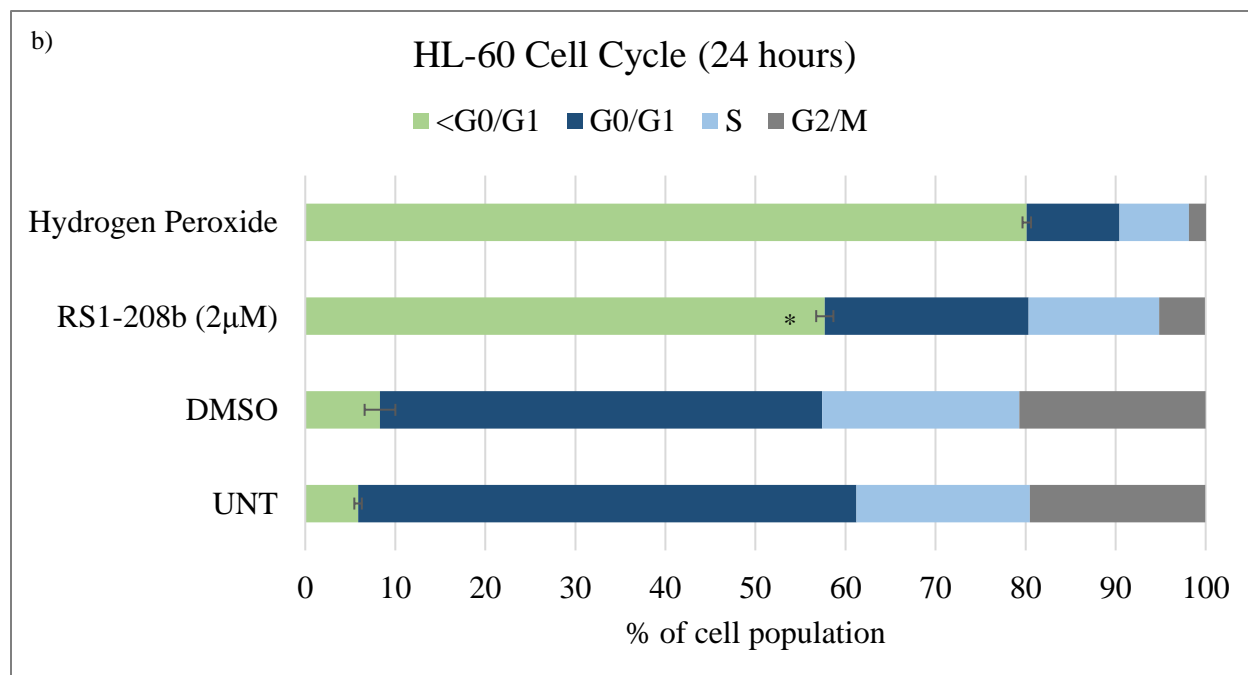
b) Bar graphs represent average values (biological replicates = 3) of histograms. The <G0/G1 in RS1-208b treated cells was significantly higher than the DMSO control, indicating that the compound induces apoptosis in HL-60 cells after 24 hours of treatment. The G0/G1 peak was significantly smaller ($p < 0.05$) in the RS1-208b treated cells than DMSO control, suggesting that cells did not re-enter the cell cycle following mitosis. The percentage of cells in the S phase and G2/M phase was similar between RS1-208b treated cells and DMSO control. Standard deviations were included for the <G0/G1 peak.

c)

RAMOS Cell Cycle (24 hours)

■ <G0/G1   ■ G0/G1   ■ S   ■ G2/M
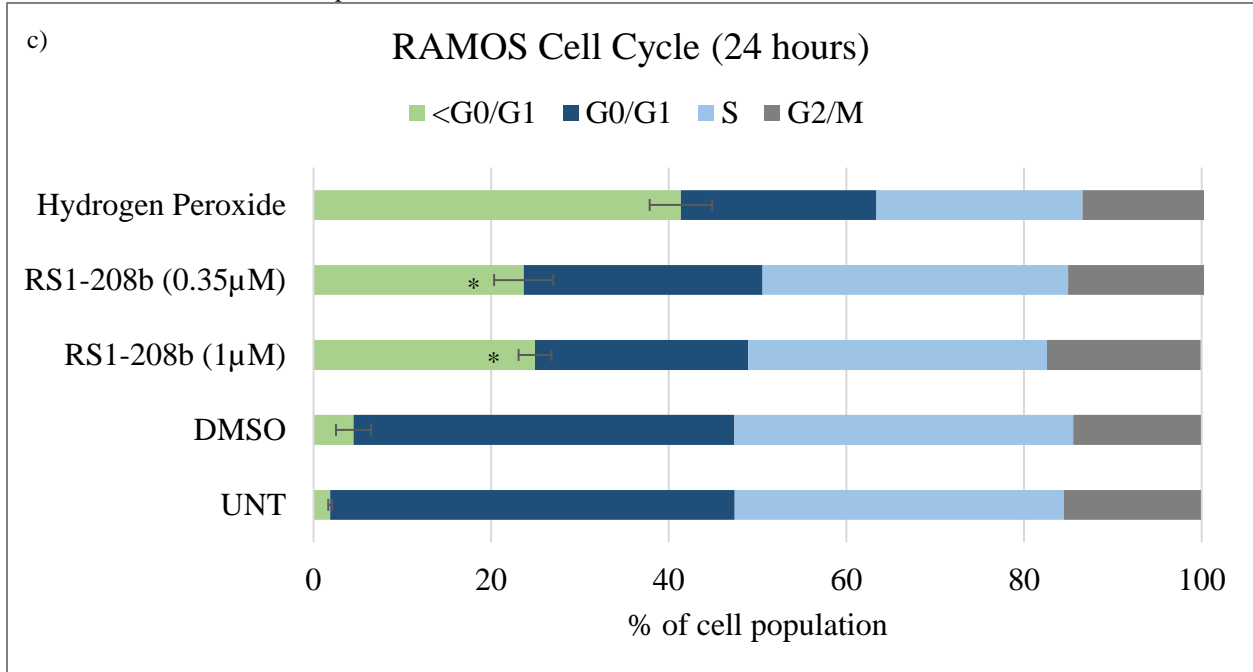
c) Bar graphs represent average values (biological replicates = 3) of histograms. The <G0/G1 in RS1-208b treated cells was significantly higher than the DMSO control, indicating that the compound induces apoptosis in RAMOS cells after 24 hours of treatment. The G0/G1 peak was significantly smaller ($p < 0.05$) in the RS1-208b treated cells than DMSO control, suggesting that cells did not re-enter the cell cycle following mitosis. The percentage of cells in the S phase and G2/M phase was similar between RS1-208b treated cells and DMSO control. Standard deviations were included for the <G0/G1 peak.

The formation of apoptotic bodies was concentration dependent in the CCRF-CEM cell line ($p < 0.05$). Interestingly, the results from CCRF-CEM and RAMOS cell lines indicate that RS1-208b does not affect the S or G2/M phases, as there was no appreciable difference in these phases across treatments. However, in the HL-60 cell line there was a decrease in the percentage of cells in both the S and G2/M phase.

Though we did not observe an arrest in the progression through the cell cycle in any of the cell lines tested, we were able to narrow down the pathway of cell death treatment with RS1-208b initiated.

22

4. Evaluating Apoptosis Induced by R1-208b

4.1 Assessment of Phosphatidylserine Externalization Induced by RS1-208b

Phosphatidylserine (PS) is a phospholipid that, in viable cells, is only found on the inner leaflet of the mammalian cell membrane[44,45]. The asymmetry is maintained by ATP-dependent flippases that quickly internalize PS that has been exposed to the outer leaflet[46]. Externalization of PS occurs when a cell is undergoing apoptosis and it serves to recruit macrophages[47] to facilitate the cell's degradation and subsequent removal from the system. During apoptosis, calcium is released from the endoplasmic reticulum and mitochondria which activates Ca^{+2}-dependent scramblases[46,47] that externalize the PS and mark the cell for degradation by macrophages[48]. Furthermore, under apoptotic conditions, cells decrease ATP production, leading to the inactivation of ATP-dependent flippases that would otherwise internalize PS.

The Annexin V assay was used in order to confirm the results of the cell cycle assay that the cytotoxicity induced by RS1-208b was occurring through apoptosis. Annexin V is a small protein with high affinity to PS[47]. The assay employs an Annexin V that is conjugated to FITC (fluorescein isothiocyanate), a fluorescent dye, which, upon Annexin V binding of PS, undergoes a conformational change in structure that allows for excitation and emission. Annexin V is impermeable to the cell membrane only capable of binding to externalized PS[47], thus the percentage of cells fluorescing green are considered to be undergoing cell death through apoptosis. The assay also makes use of PI (which intercalates DNA and double stranded RNA in cells whose membranes have become compromised[43]) to distinguish between early apoptosis (only externalization of PS) and late apoptosis (externalized PS and also compromised membrane). Furthermore, cells that only fluoresce red (stained only with PI) are thought to have experienced cell death through a mechanism other than apoptosis.

23

Cells were seeded at 200,000 cells/mL/well in a 24-well plate and treated with RS1-208b for 24 hours. Hydrogen peroxide treated cells, untreated cells, and DMSO treated cells were used as positive, negative, and vehicle controls, respectively. Following 24 hours of treatment, cells were collected in 5mL culture tubes and centrifuged for 5 minutes at 1200rpm. The supernatant was discarded and the cells were re-suspended in 100µL of ice-cold 1x Binding Buffer containing 1µL of Annexin V-FITC and 2.5µL of PI. The tubes were then incubated on ice in the dark for 15 minutes. After the incubation, 400µL of ice-cold 1x Binding Buffer was added to each tube and read using a flow cytometer equipped with a 488nm OPSL Sapphire laser. FITC signal was detected through the FL1 channel and propidium iodide was detected through the FL2 channel. Below are graphical representations of the percentage of cells stained with either FITC (cells with externalized PS; early and late apoptosis) or only PI.

The results from the Annexin V assay confirm that RS1-208b induces apoptosis in hematological cancer cell lines. However, they also point to a non-apoptotic mechanism of cell death that is also induced by the compound. There was a correlation between increasing the concentration of RS1-208b and externalization of phosphatidylserine that was not apparent between the concentration of RS1-208b and the other mechanism of cell death (presumably, necrosis).
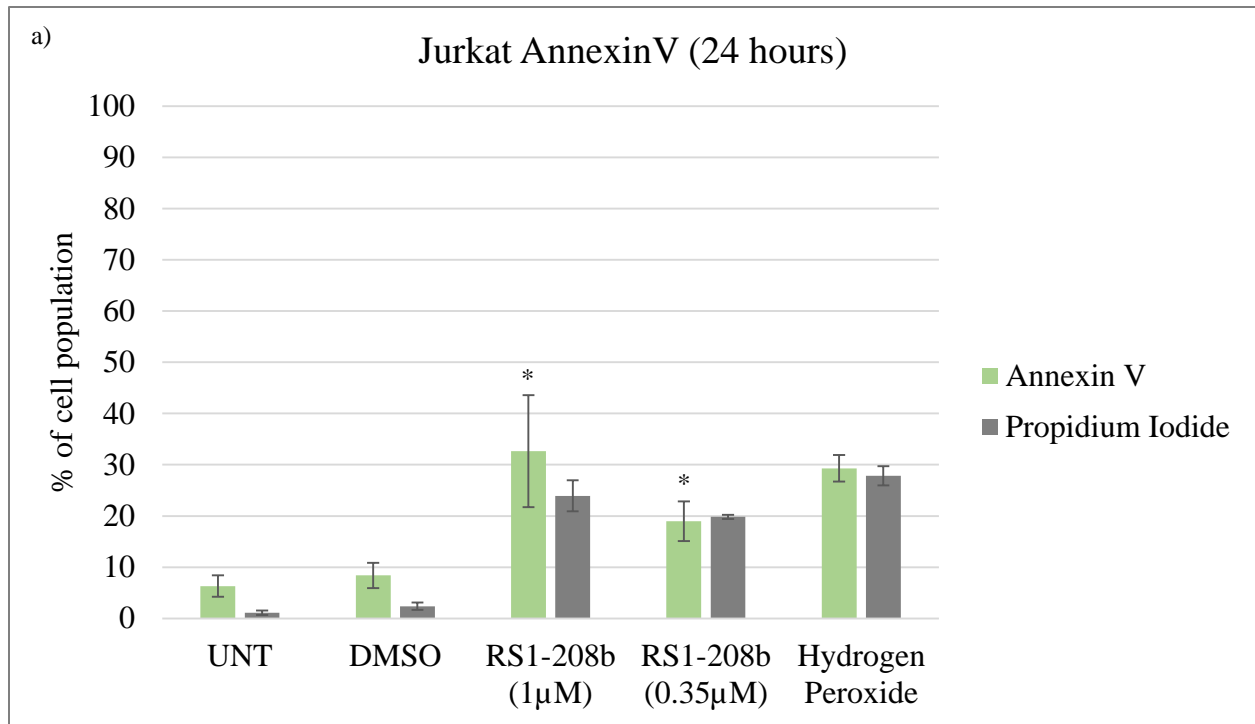
Figure 4. RS1-208b Induces Phosphatidylserine Externalization

a) Bar graphs (± standard deviation) represent average values (biological replicates = 3) of the percentage of Jurkat (ALL) cells stained with FITC (cells undergoing apoptosis) and cells stained with only PI. RS1-208b induces phosphatidylserine externalization ($p < 0.05$) in a concentration dependent manner in Jurkat cells.
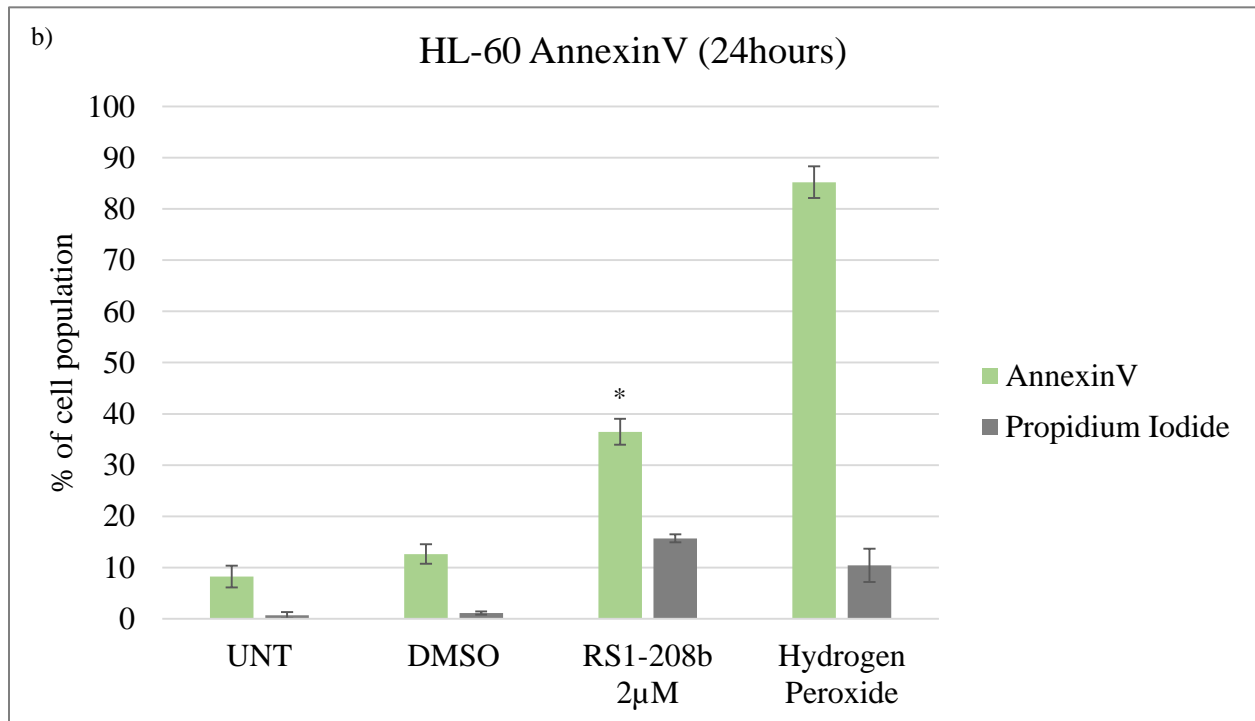
b) Bar graphs (± standard deviation) represent average values (biological replicates = 3) of the percentage of HL-60 (ALL) cells stained with FITC (cells undergoing apoptosis) and cells stained with only PI. In HL-60 cells, RS1-208b induces the externalization of phosphatidylserine. The difference between RS1-208b treated and vehicle treated is statistically significant ($p < 0.05$).

c) RAMOS AnnexinV (24hours)
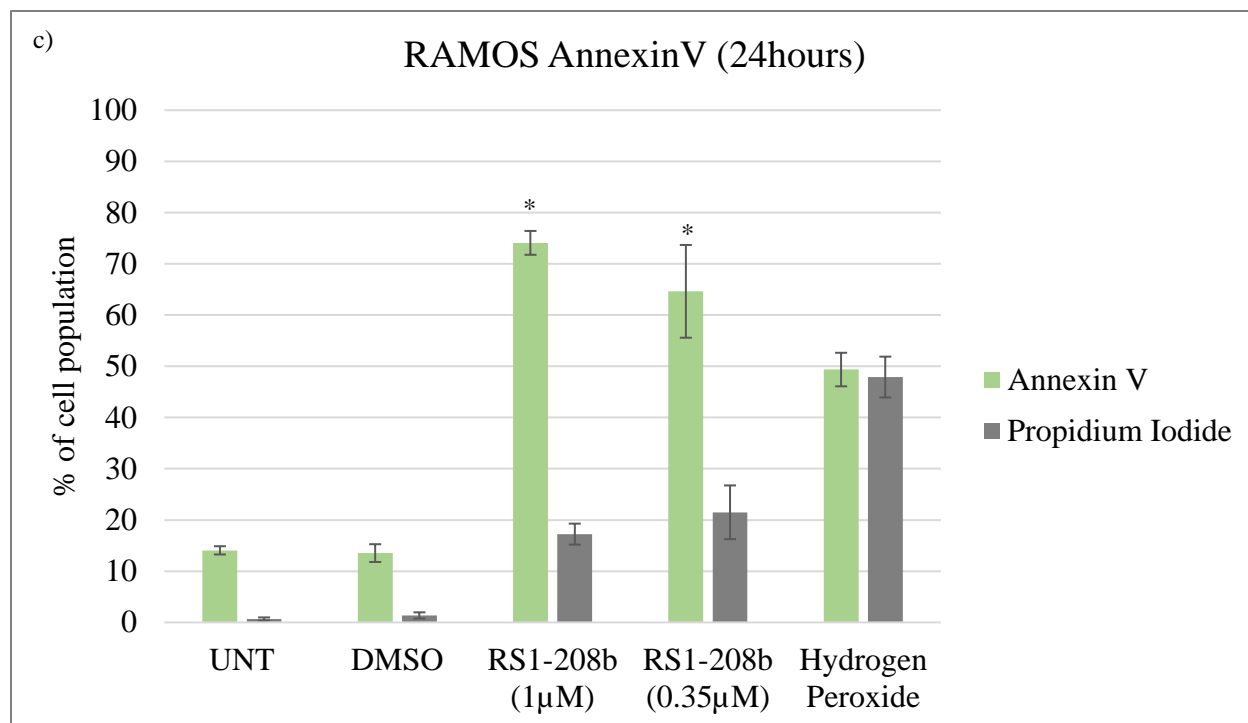
c) Bar graphs (± standard deviation) represent average values (biological replicates = 3) of the percentage of RAMOS (ALL) cells stained with FITC (cells undergoing apoptosis) and cells stained with only PI. RS1-208b induces phosphatidylserine externalization ($p < 0.05$) in RAMOS cells in a concentration dependent manner.

The molecular structure of RS1-208b has been described as having inhibitory effects on the release of inflammatory cytokines[29]. Despite this, the other mechanism of death induced points to the possibility RS1-208b to elicit an inflammatory response *in vivo*. Though chronic inflammation has been linked to carcinogenesis, acute inflammation, such as that caused by chemotherapy, could have beneficial effects by amplifying the cell death and rapidly clearing cellular debris from the tumor site, leading to a reduction in tumor size.

4.2 Assessment of Mitochondrial Involvement in Apoptosis Induced by RS1-208b

The mitochondria is an important organelle that generates ATP for the cell to use[49]. ATP generation depends on the mitochondria's ability to establish and maintain a transmembrane potential[50]. The electron transport chain is responsible for releasing protons into the

26

mitochondria's transmembrane space, which, compared to the mitochondrial matrix and the cytoplasm, is relatively positively charged.

The loss of mitochondrial transmembrane potential is observed at early time points during apoptosis via the intrinsic pathway[49,50]. Through this pathway, pro-apoptotic proteins of the BCL2 family of proteins are thought to oligomerize[50] along the outer membrane of the mitochondria and form pores or channels through which protons and other contents sequestered in the intermembrane space of the mitochondria are released. This results in the loss of the transmembrane potential established through the electron transport chain, and consequently, the loss of ATP generation. Furthermore, cytochrome c (and stored calcium cations) are also released from the intermembrane space and can act as second messengers and participate in the apoptotic signaling pathway[49,50].

The mitochondrial depolarization assay JC-1 uses a cationic dye (5',6,6'-tetrachloro-1,1',3,3'-tetraethylbenzimidazolylcarbocyanine iodide) capable of emitting fluorescence of two different wavelengths, depending on its aggregation status. The dye is permeable to the mammalian cell membrane as well as the mitochondrial membranes. In healthy, viable cells, the cationic dye penetrates the mitochondrial membranes and deposits itself in the mitochondrial matrix (negatively charged), where it forms aggregates in a concentration dependent manner. Dye that isn't found in the matrix is found in the cytosol (negatively charged), where it is unable to form aggregates due to the cytosol's higher relative volume, which decreases the relative concentration of the JC-1. However, in cells undergoing apoptosis, the flux of dye between the matrix and cytosol increases due to oligomerization of Bax/Bak proteins and the subsequent depolarization of the mitochondria, resulting in an increase of monomer to aggregate signal.

27

Cells were seeded at 200,000 cells/mL/well in 24-well plates and treated with RS1-208b for 5 hours. Hydrogen peroxide treated cells, untreated cells, and DMOS treated cells were used as positive control, negative control, and vehicle control, respectively. Cells were collected into 5mL culture tubes and centrifuged for 5 minutes at 1200rpm. The supernatant was decanted and the cells re-suspended in 500µL of PBS along with 5µL of the JC-1 dye, and incubated at 37ºC for 0.5 hours. The cells were then analyzed using a flow cytometer with a 488nm OPSL Sapphire laser to excite the JC-1 and the emission of monomers and aggregates was detected through the FL1 and FL2 channels, respectively. The graphs below represent the monomer/aggregates ratios to indicate the polarization status of the mitochondria; a higher ratio indicates the mitochondria has become depolarized.
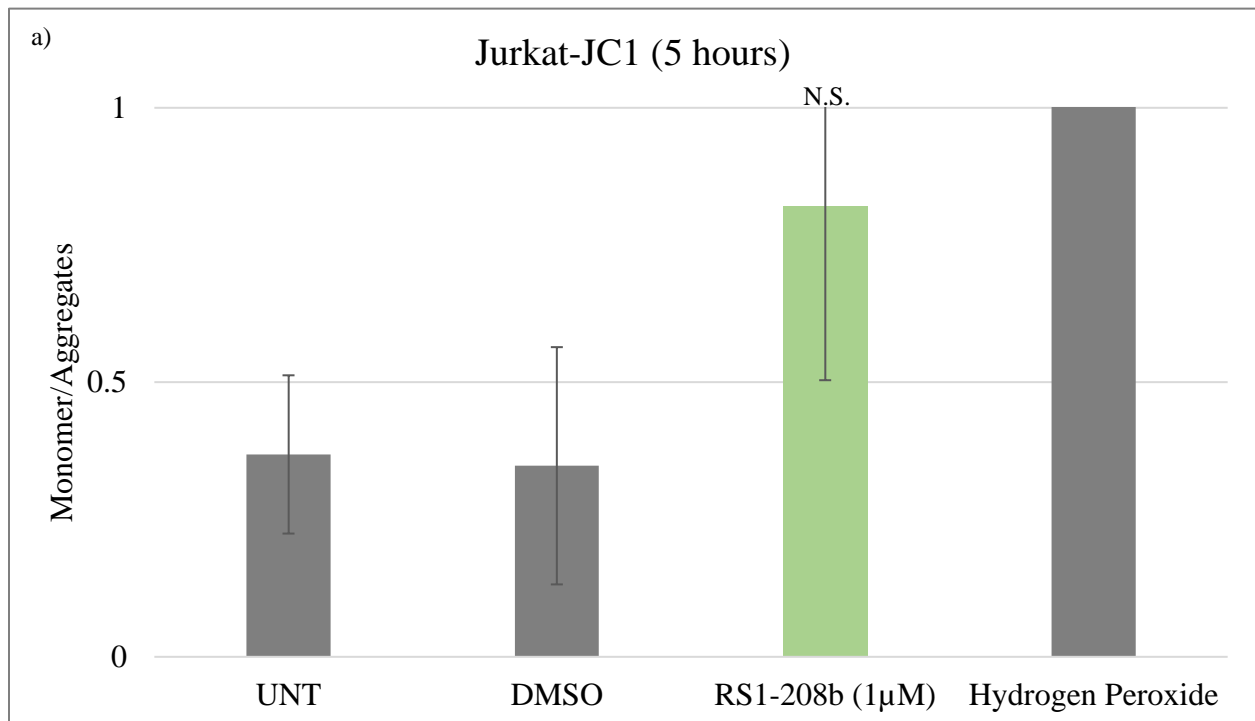
Figure 5. RS1-208b Induces Mitochondrial Depolarization
a) Bar graphs represent the ratio (± standard deviation) of monomers/aggregates (biological replicates = 3). Mitochondrial depolarization is observed in Jurkat following 5 hours of treatment with RS1-208b, though the difference in this experiment was not statistically significant.
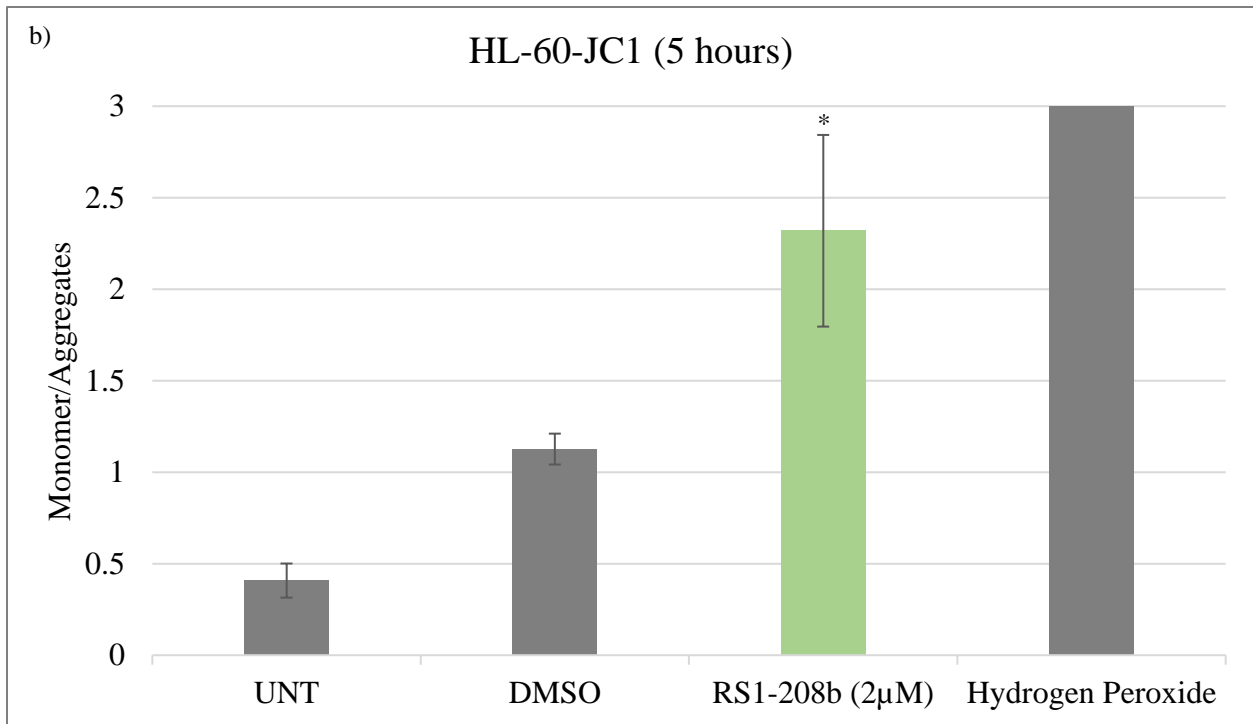
b) Bar graphs represent the ratio (± standard deviation) of monomers/aggregates (biological replicates = 3). Statistically significant ($p < 0.05$) mitochondrial depolarization is observed in HL-60 following 5 hours of treatment with RS1-208b.
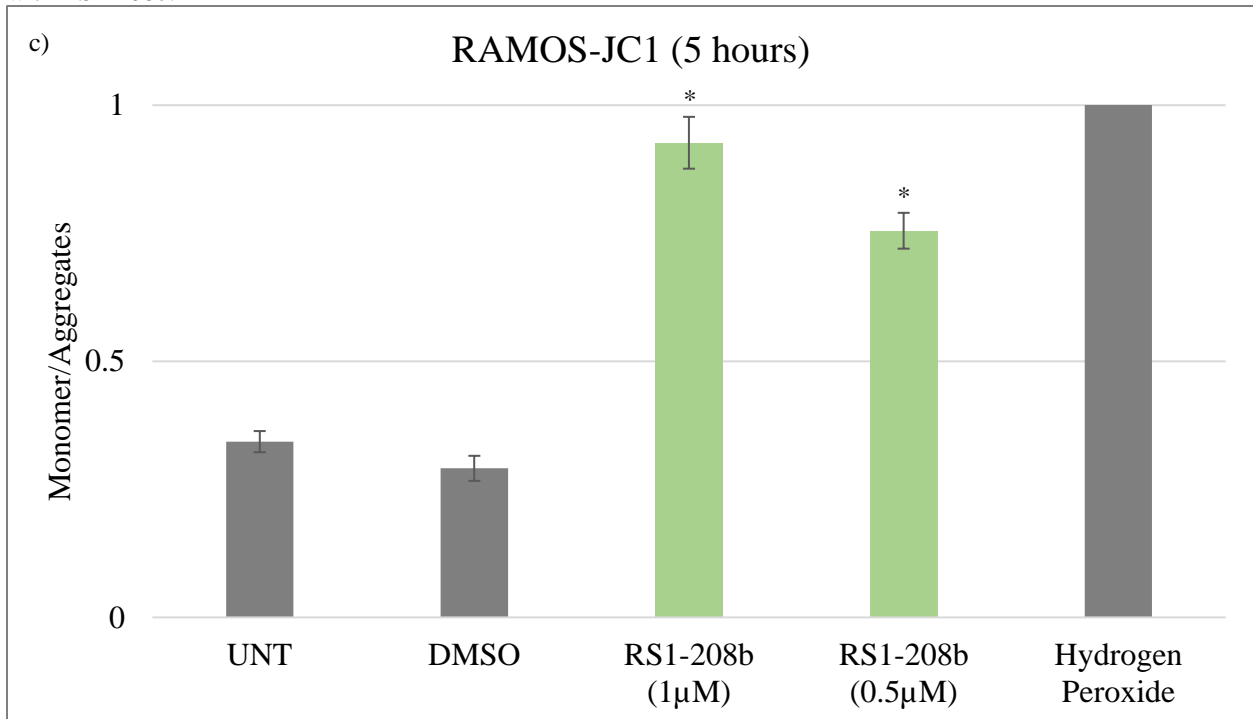
c) Bar graphs represent the ratio (± standard deviation) of monomers/aggregates (biological replicates = 3). Statistically significant ($p < 0.05$) mitochondrial depolarization is observed in RAMOS following 5 hours of treatment with RS1-208b.

Mitochondrial depolarization was assessed in three different hematological cancer cell lines (Jurkat, HL-60, and RAMOS). Though in Jurkat the results did not achieve statistical significance, there was an appreciable increase in the mitochondrial depolarization of the cells treated with RS1-208b compared to vehicle control. In the HL-60 cell line, the mitochondrial depolarization induced by RS1-208b was statistically significant when compared to DMSO. In the RAMOS cell line, the mitochondrial depolarization was shown to be dose dependent, with both concentrations of RS1-208b tested being statistically significant. The mitochondrial depolarization results suggest that RS1-208b induces apoptosis through the intrinsic pathway in the hematological cancer cell lines tested.

4.3 Assessment of the Involvement of Caspase 3 in RS1-208b Induced Apoptosis

Caspases (cysteine-dependent aspartate-directed proteases) are enzymes activated from zymogens that are recruited through the apoptosis signaling pathway to cleave a large number of target molecules at specific sites and aid in the degradation of proteins[51]. Caspases are generally classified into three categories: inflammatory caspases, initiator caspases, and executioner caspases[50,51]. The activation of individual caspases depends on the specific pathway of cell death, though there is experimental data which suggests cross-talk between cell death pathways[51].

The activation of effector caspases is downstream of mitochondrial depolarization, following cytochrome c and calcium release from the intermembrane space into the cytosol[50,51]. Cytochrome c and Apaf-1 molecules combine to form the apoptosome in the presence of calcium[50]. The apoptosome then cleaves pro-caspase-9 and activates caspase-3[49,50]. The activation of Capase-3 in response to treatment with RS1-208b provides a direct link between the RS1-208b induced mitochondrial depolarization observed at 5 hours and the cell death through apoptosis observed following 24 hours of treatment.

30

The Caspase-3 assay uses a substrate composed of a fluoregenic DNA dye that is permeable to the cell membrane and is coupled to a caspase-3 recognition site. Activated caspase-3 in cells undergoing apoptosis cleaves the substrate, releasing the fluoregenic dye, which translocates to the nucleus, where it binds to DNA and emits fluorescence following excitation with an OPSL Sapphire laser.

Cell were seeded at 200,000 cells/mL/well in a 24-well plate and treated with RS1-208b for 7 hours. Hydrogen peroxide treated cells, untreated cells, and DMSO treated cells were used as positive control, negative control, and vehicle control, respectively. Cells were collected into 5mL culture tubes and centrifuged for 5 minutes at 1200rpm. Following centrifugation, the supernatant was decanted and the cells re-suspended in 200µL of PBS and incubated with 5µL of the substrate stock solution for 30 minutes in the dark at room temperature. PBS (200µL) was then added to each tube and the tubes assessed with a flow cytometer using a 488nm OPSL Sapphire laser to excite the fluoregenic dye. The FL1 channel was used for the detection of fluoregenic dye that was released from the substrate by caspase 3 and bound to DNA. Below are bar graphs representing the percentage of the population in each treatment group that had activated caspase 3.

Caspase 3 was activated in both HL-60 and RAMOS cell lines, though the effect was more pronounced in RAMOS. Compared to the vehicle control, the results were shown to be statistically significant ($p < 0.05$). This places caspase 3 activation directly down-stream of mitochondrial depolarization and confirms the intrinsic pathway of apoptosis.

31

Figure 6. RS1-208b Induces Caspase 3 Activation
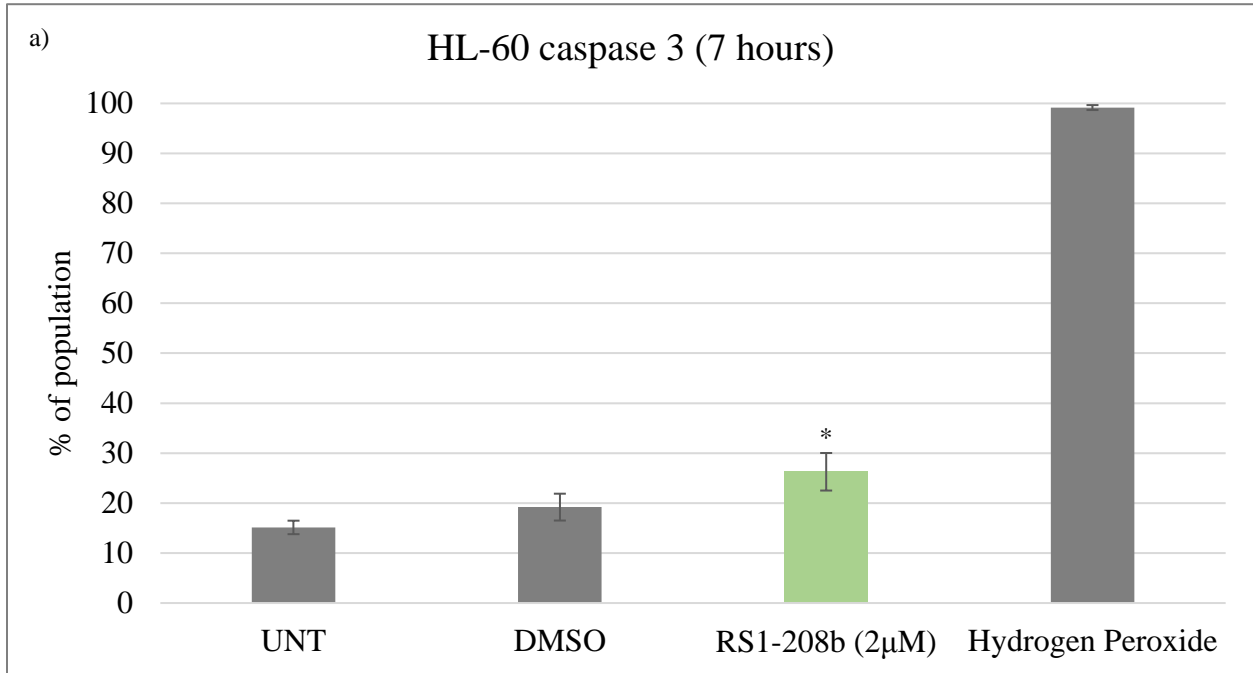
a) Bar graphs represent average (± standard deviations) of the percentage of cells with active caspase 3 (biological replicates = 3). RS1-208b induced the activation of caspase 3 in HL-60 at 7 hours of treatment and the induction is statistically significant ($p < 0.05$), compared to DMSO. The results indicate the intrinsic pathway of apoptosis is induced by RS1-208b.
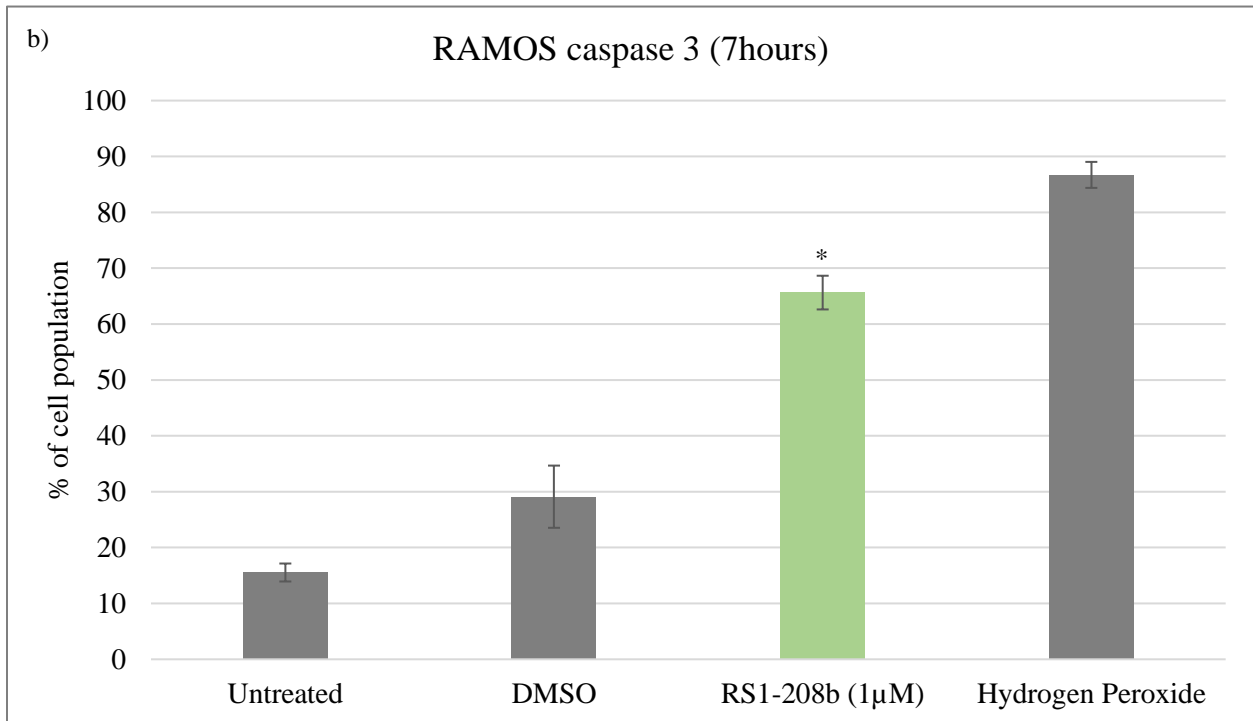
b) Bar graphs represent average (± standard deviations) of the percentage of cells with active caspase 3 (biological replicates = 3). RS1-208b induced the activation of caspase 3 in RAMOS at 7 hours of treatment and the induction is statistically significant ($p < 0.05$), compared to DMSO. The results indicate the intrinsic pathway of apoptosis is induced by RS1-208b.

4.4 Assessment of the Involvement of Caspase 8 in RS1-208b Induced Apoptosis

Caspase-8 is one of two initiator caspases with a death effector domain[44,51]. It is recruited and trans-activated following ligand biding to a death receptor at the surface of the cell membrane[44]. This pathway of apoptosis (initiated by ligand binding to death receptor) is referred to as the extrinsic pathway of apoptosis, and generally bypasses mitochondrial depolarization at the early hours[50,52]. Caspase-8 activation generally peaks at 4 hours following treatment with extrinsic apoptosis inducing compounds[52].

The Caspase-8 assay uses a substrate conjugated to FITC. In cells undergoing apoptosis through the extrinsic pathway, activated Caspase-8 activated at the early hours recognizes and cleaves the substrate, allowing for the detection of the conjugated FITC dye by fluorescent means.

Cells were seeded at 200,000 cells/mL/well in 24-well plates and treated with RS1-208b for 4 hours. Untreated cells and DMSO treated cells were included as negative and vehicle controls. During the optimization of the protocol we were unable to find a suitable positive control for Caspase-8 activation. Following treatment, 300µL of each well were collected into 5mL culture tubes and incubated with 1µL of the Caspase-8 substrate for 1 hour at 37ºC. Culture tubes were then centrifuged for 5 minutes at 1200rpm and the supernatant decanted. Cells were washed with the wash buffer provided in the staining kit, centrifuged (5 minutes at 1200rpm), and the supernatant decanted, twice. Flow cytometry analysis was done using a flow cytometer with a 488nm OPSL Sapphire laser to excite FITC, and the FL1 channel to detect emission of fluorescence. Cells stained with FITC indicate activation of caspase-8 and implicate the extrinsic pathway of apoptosis. The results are represented in bar graphs below.

The activation of caspase-8 by RS1-208b at 4 hours of treatment was not statistically significantly different when compared to the DMSO vehicle control, indicating the extrinsic

33

pathway of apoptosis is not a pathway involved in the observed cell death. This result, along with the caspase-3 data, implicates the mitochondria-mediated intrinsic pathway as the major (if not only) pathway of programmed cell death induced by RS1-208b in hematological cancer cell lines.
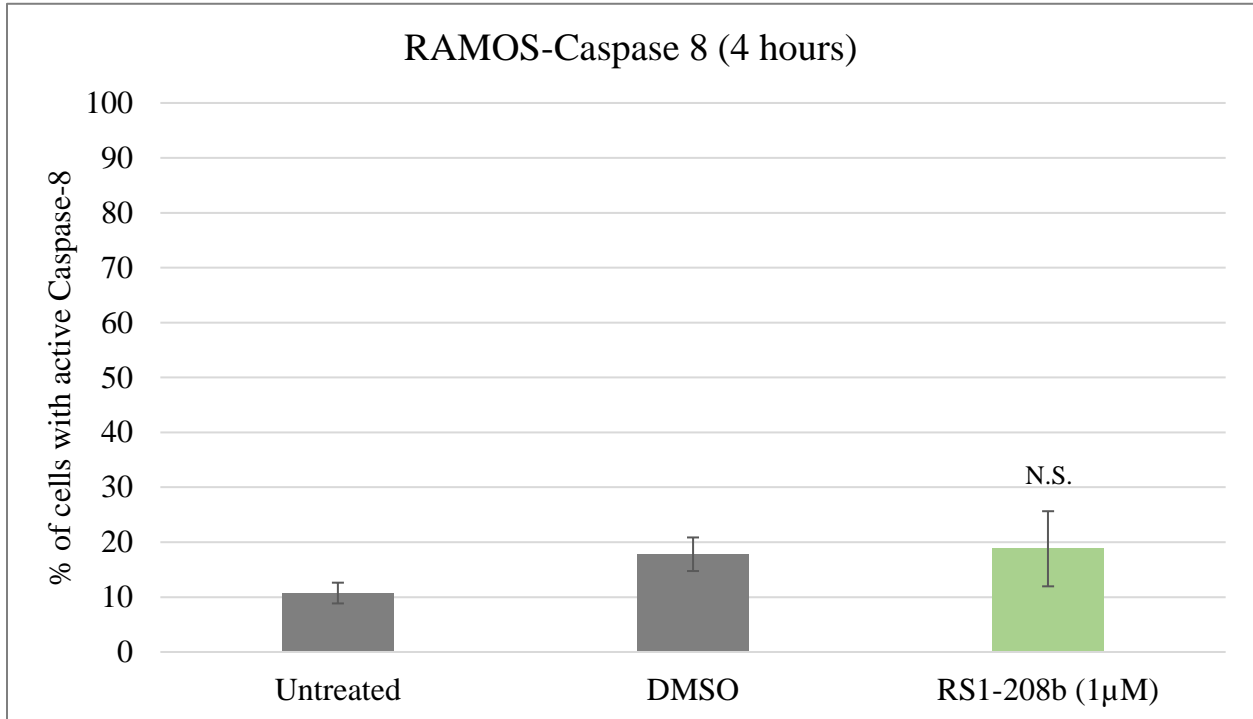
Figure 7. RS1-208b Does Not Induce the Activation of Caspase 8
Bar graphs represent the average values (± standard deviations) of the percentage of cells with activated Caspase-8 (biological replicates = 3) following 4 hours of treatment. Caspase-8 activation was not statistically significantly different ($p > 0.05$) in RS1-208b treated cells compared to DMSO.

4.5 Assessment of Tumor Necrosis Factor α (TNFα) Production

The like curcumin[14], molecular structure of RS1-208b has been reported to inhibit the production of pro-inflammatory cytokine IL-6[29]. Analysis of the Annexin V assay pointed to necrosis as a possible secondary pathway of cell death induced by RS1-208b, a pathway which could elicit an inflammatory response. We independently assessed whether RS1-208b lead to the production of a different pro-inflammatory cytokine (TNFα) that is also involved in the extrinsic

المنارة للاستشارات
www.manaraa.com

pathway of apoptosis and necrosis[53,54]. RS1-208b was not shown to induce the activation of the extrinsic pathway of apoptosis at 4 hours, therefore we assumed that if TNFα was released in response to RS1-208b, the cell death pathway it would trigger would be necrosis. This would help us determine the potential inflammatory response RS1-208b could elicit *in vivo* by identifying the secondary mechanism of cell death we observed in the Annexin V assay.

Necrosis and inflammation play an important and somewhat curious roles in tumor development[54]. On the one hand, tumor cells that underdo necrosis in response to chemotherapeutics lead to an acute inflammatory response that quickly removes them from the system. However, prolonged or chronic inflammation provides an ideal milieu for tumor development. In this way, cell death of a small sub-set of the tumor population through necrosis could prove to be beneficial as long as treatment with RS1-208b does not lead to the perpetual production of inflammatory cytokines.

The Thermo Fisher Scientific Human TNFα ELISA kit (EH3TNFa) was used to determine the production of TNFα in Jurkat cells in response to RS1-208b. Enzyme-linked immunosorbent assays (ELISA) offer a quick and easy way to quantify soluble proteins using a spectrophotometer and a ladder of standards with known concentrations. This particular assay uses a 96-well plate that has been pre-coated with an antibody against human TNFα. For this assay, 100,000 cells/mL were treated with 0.5μM RS1-208b, 1μM RS1-208b, 1% v/v DMSO, or left untreated. Cells were collected into micro-centrifuge tubes following 6 hours of incubation with RS1-208b and centrifuged for 5 minutes at 1200rpm. The supernatant was collected into new micro-centrifuge tubes and stored at -80ºC overnight. The protocol provided by Thermo Fisher Scientific was followed with no modifications. Briefly, the assay consists of adding the supernatant (presumably containing cytokines released in response to treatment with RS1-208b)

35

collected to the wells pre-coated with the antibody against TNFα. A biotinylated antibody is then

added, followed by horseradish peroxidase conjugated streptavidin. Finally, a color changing

substrate is added before reading through a spectrophotometer, reading at a wavelength of

450nm. Optimization of the protocol failed to reveal a trustworthy positive control. Untreated

cells and DMSO treated cells were used as negative and vehicle controls, respectively.
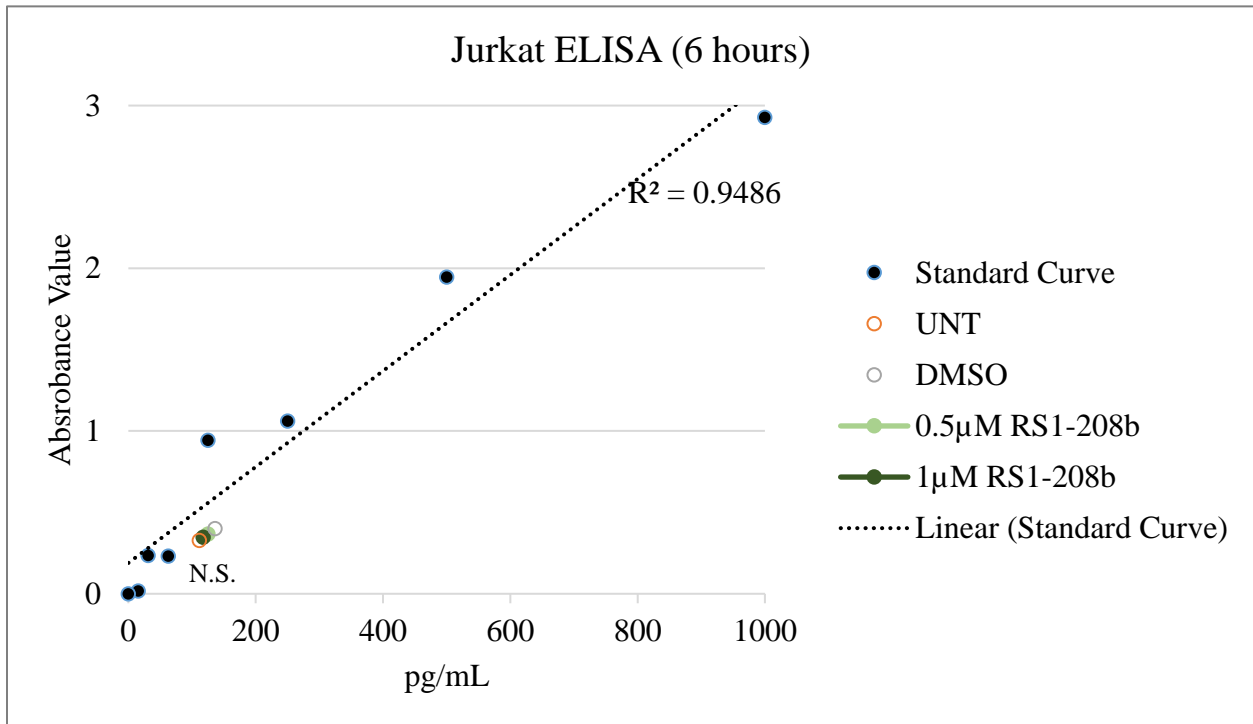
Figure 8. RS1-208b Does Not Lead to the Production and Release of TNFα
Treatment of Jurkat cells (biological replicates = 3) does not lead to the production and subsequent release of pro-inflammatory cytokine TNFα. Points on the graph represent average values.

Treatment of Jurkat cells with RS1-208b at both concentrations resulted in a slight

(though, not statistically significant) inhibition of TNFα production and release, compared to

DMSO, though the inhibition did not appear to be concentration dependent. The data indicates

that RS1-208b does not induce TNFα cytokine release, and would, therefore, not likely elicit a

sustained pro-inflammatory response *in vivo* that would lead to chronic inflammation around the tumor site.

5. Identifying the Molecular Pathway of RS1-208b Induced Apoptosis

5.1 Transcriptome Analysis Using AmpliSeq

Recent advances in RNA sequencing technology have made analysis of transcriptomes economically feasible and have drastically increased the throughput capacity compared to conventional microarrays and RT-qPCR[55]. Though most RNA-sequencing systems employ a similar fluorescence based method of detection, AmpliSeq uses Ion Torrent Proton next generation sequencing (NGS) technology to sequence transcriptomes[56], allowing for decreased background noise on longer transcripts. Briefly, the Ion Torrent Proton NGS uses a semiconductor to detect changes in pH as a nucleotide is added to the pre-amplified transcripts and converts it into an electrical signal[56]. Molecular barcodes enable mapping onto target sequence library[56].

Comparison of Illumina HiSeq (one of the most widely used RNA-seq platforms) and Ion Torrent Proton sequencing platforms using standard RNA reference samples found strong concordance (Pearson's r = 0.92[56]). Furthermore, AmpliSeq outperforms Illumina HiSeq for highly abundant genes while capturing similar patterns of gene expression[56]. AmpliSeq's high accuracy and sensitivity for whole transcriptome analysis is on par with some of the most advanced and widely used RNA-sequencing technologies but at a fraction of the cost[56].

HL-60 cells (400,000 cells/2mLs/well in a 24-well plate) treated with either 2µM RS1-208b or PEG-400 (0.3% v/v) for 6 hours (biological replicates = 3). The cell line and time point were selected for direct comparison against the Broad Institute's Connectivity Map (cMAP). PEG-400 was selected as the vehicle control to minimize the effect contributed to the vehicle (see Figure 17.). Following treatment, cells were collected into microcentrifuge tubes and centrifuged for 5 minutes at 1400rcf. Cells were then washed with ice cold PBS and centrifuged (5 minutes at 1400rcf), twice. PBS was aspirated and the dry pellet stored at -80ºC overnight.

38

The following morning, RNA was extracted using Qiagen's RNeasy Mini Kit (74104), following the protocol provided, along with the optional Qiashredder (79654) and DNAse II digestion steps, to maximize RNA extraction and minimize DNA contamination. RNA quantification and purity assessment was performed using the NanoDrop. The results for individual replicates are summarized below. A_{260}:A_{280} ratios above 2.0 and A_{260}:A_{230} ratios above 1.7 were taken to indicate successful RNA extraction and purity of RNA. RNA sequencing was performed using Ion AmpliSeq Transcriptome Human Gene Expression Kit (ThermoFisher Scientific, A26325).

Table 4. RNA Extraction Results for AmpliSeq Analysis Indicate High Purity RNA

Sample ID	Sample Volume	ng/µL	260/280	260/230
PEG-400-1	30µL	54.60	2.14	1.71
PEG-400-2	30µL	50.91	2.18	1.84
PEG-400-3	30µL	42.88	2.14	1.86
RS1-208-1	30µL	49.87	2.19	1.98
RS1-208-2	30µL	43.99	2.16	1.90
RS1-208-3	30µL	45.08	2.23	1.87

Analysis of AmpliSeq data revealed 604 genes that were more than 2-fold differentially regulated in HL-60 cells treated with RS1-208b for 6 hours. Of those 604 genes, 421 genes were more than 2-fold up-regulated and 183 genes were more than 2-fold down regulated. Table 5 and Table 6 summarize the genes that were more than 5-fold differentially regulated in response to treatment with RS1-208b for 6 hours compared to the vehicle control.

The most up-regulated gene in response to treatment with RS1-208b was HMOX1 (heme oxygenase 1), a gene integral in the regulation of oxidative stress[57]. A quick overview of the most up-regulated genes suggests that RS1-208b induces the transcription of a large number of heat shock genes, suggesting that protein misfolding might play a role in the cell death induced by RS1-208b. ATF3 (activating transcription factor 3), a transcription factor that is important in

39

the signaling pathway of the endoplasmic reticulum stress response[58], was one of the most up-regulated genes in response to RS1-208b. Preliminary analysis of the AmpliSeq data using only the most up-regulated genes pointed towards RS1-208b inducing cell death through oxidative and endoplasmic reticulum stress.

Table 5. List of Genes That Were More Than 5-fold Up-Regulated in Response to Treatment with RS1-208b for 6 Hours Compared to Vehicle Control

ID	EntrezGene	FC	pValue
HMOX1	3162	700.2631	2.14E-237
HSPA6	3310	518.3819	2.21E-150
HSPA1B	3304	425.3722	1.89E-136
HSPA1A	3303	231.6072	4.95E-134
BAG3	9531	139.2204	5.56E-127
DUSP1	1843	100.1904	8.11E-45
ATF3	467	96.70101	4.97E-100
DNAJA4	55466	85.74082	7.98E-136
DNAJB1	3337	53.93731	1.57E-147
CHAC1	79094	51.29061	1.98E-156
DNAJB4	11080	30.96209	1.69E-43
CDKN1A	1026	30.88426	4.53E-34
PPP1R15A	23645	29.9688	1.15E-150
HSPH1	10808	24.41394	2.07E-180
FOSB	2354	23.85085	2.11E-56
SERPINH1	871	22.13491	1.90E-22
FOSL1	8061	21.49553	2.87E-31
SESN2	83667	21.33146	3.75E-149
ADM	133	20.85347	8.81E-81
PMAIP1	5366	20.65687	3.90E-89
USPL1	10208	17.46388	2.95E-36
ZFAND2A	90637	17.41307	1.23E-41
RGS2	5997	17.39775	2.05E-18
DDIT4	54541	17.21004	2.72E-120
PTGS2	5743	12.52229	6.98E-18
HBEGF	1839	12.20392	6.91E-48
LINC00641	283624	9.893837	3.77E-41
EGR1	1958	9.874298	8.25E-11
IER5	51278	9.831486	6.89E-57

40

CHORDC1	26973	9.148122	3.46E-50
VEGFA	7422	9.014776	9.01E-71
DNAJA1	3301	8.961766	2.31E-126
HSP90AA1	3320	8.606375	1.23E-103
TNFRSF10D	8793	8.404733	3.16E-36
MRPL18	29074	8.290333	1.67E-96
HMGCS1	3157	8.242085	2.85E-85
TUFT1	7286	7.902703	1.99E-36
BCAS2	10286	7.550944	7.19E-106
MXD1	4084	7.230572	9.79E-76
TOR1AIP2	163590	7.042911	5.83E-33
HSPA8	3312	6.808084	2.01E-92
HERPUD1	9709	6.688471	1.25E-88
SPATA2	9825	6.247421	6.76E-46

Table 6. List of Genes That Were More Than 5-Fold Down-Regulated in Response to Treatment with RS1-208b for 6 Hours Compared to Vehicle Control

ID	EntrezGene	1/FC	p-Value
HIST1H2BC	8347	10.03775	6.98E-12
THEMIS2	9473	8.676445	1.94E-40
HIST1H1D	3007	8.09482	1.77E-26
HIST1H3C	8352	6.744863	1.15E-67
NFE2	4778	6.358766	4.85E-32
GFI1	2672	5.954293	2.20E-85
P2RY2	5029	5.742057	4.69E-67
CEBPE	1053	5.448144	1.43E-51
MYC	4609	5.133881	4.57E-46
HIST1H2BF	8343	5.046388	1.55E-13

Data analysis of the most down-regulated genes in response to treatment with RS1-208b did not implicate a particular mechanism of cell death. However, it is important to note that RS1-208b down-regulated MYC, an oncogene that is found heavily dysregulated in the majority of leukemia and lymphoma cases of childhood cancer[59,60]. MYC is a transcription factor of pro-survival genes and is partially responsible for a cancerous cell's rapid progression through the cell cycle[60]. Down-regulation of MYC could play an important role in RS1-208b induced cell

41

death by down-regulating MYC pro-survival gene targets and allowing the cell's response to shift to a pro-apoptotic response.

5.2 AmpliSeq Data Mapping onto Gene Ontology

Gene Ontology (http://geneontology.org/page/go-enrichment-analysis) is an online tool used to provide enrichment analysis on a particular set of genes. Inputting the IDs of the differentially regulated genes, we were able to identify which biological processes were most affected by treatment with RS1-208b. Figure 9 represents the number of genes differentially regulated in RS1-208b treated HL-60 cells in each biological process, listed by GO term. Table 7 summarizes the percentage of annotated genes in each biological process that were significantly up- or down-regulated in response to RS1-208b.

The biological pathways with the highest number of genes differentially regulated in response to RS1-208b were (in descending order by GO term): negative regulation of transcription, response to topologically incorrect protein folding, response to temperature stimulus, protein folding, and intrinsic apoptotic signaling pathway in response to endoplasmic reticulum stress.

The large number of significantly up-regulated heat shock genes (Table 5) are heavily involved in four-out-of-the-five processes with the most number of differentially regulated genes. Shifting the focus from total number of genes differentially expressed per biological process to the percentage of annotated genes in each pathway that were differentially expressed in response to RS1-208b, the PERK-mediated unfolded protein response stands out as the main biological process (that leads to apoptosis) affected by RS1-208b at 6 hours. This process is upstream of the up-regulation of many heat shock proteins, but most importantly, upstream to the intrinsic apoptotic signaling pathway in response to endoplasmic reticulum stress.

42
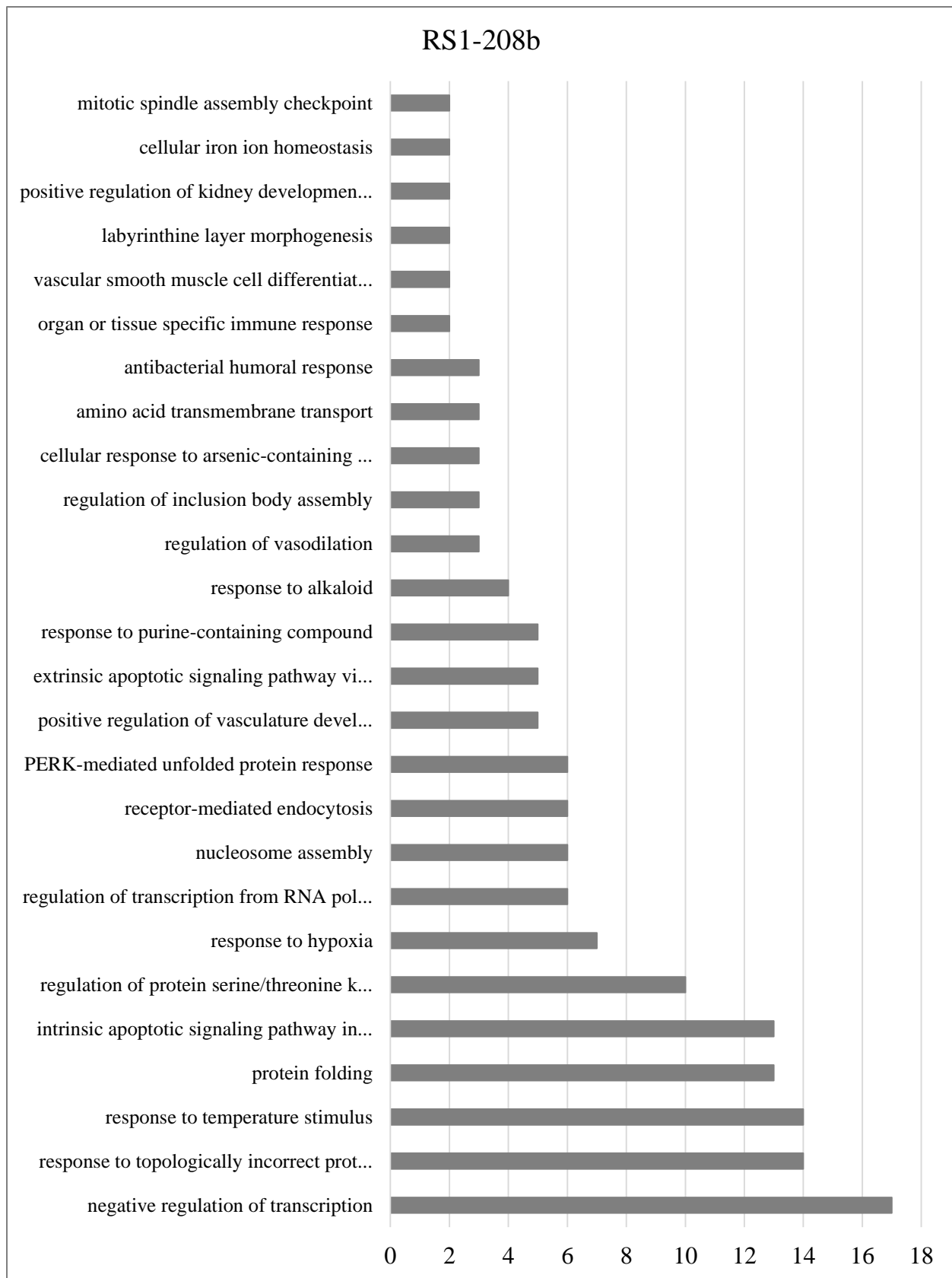
Figure 9. Number of Genes Differentially Regulated Listed by GO Term

Table 7. GO Pathways with the Most Number of Genes Significantly Affected by Treatment with RS1-208b

GO.ID	Biological Process	Annotated	Significant	%
GO:0042312	regulation of vasodilation	5	3	60.0
GO:0090083	regulation of inclusion body assembly	5	3	60.0
GO:0036499	PERK-mediated unfolded protein response	12	6	50.0
GO:0002251	organ or tissue specific immune response	5	2	40.0
GO:0035886	vascular smooth muscle cell differentiat...	5	2	40.0
GO:0060713	labyrinthine layer morphogenesis	5	2	40.0
GO:0090184	positive regulation of kidney developmen...	5	2	40.0
GO:0070059	intrinsic apoptotic signaling pathway in...	34	13	38.2
GO:0071243	cellular response to arsenic-containing ...	9	3	33.3
GO:0003333	amino acid transmembrane transport	10	3	30.0
GO:0019731	antibacterial humoral response	10	3	30.0
GO:1904018	positive regulation of vasculature devel...	20	5	25.0
GO:0043618	regulation of transcription from RNA pol...	31	6	19.4
GO:0009266	response to temperature stimulus	88	14	15.9
GO:0008625	extrinsic apoptotic signaling pathway vi...	32	5	15.6
GO:0035966	response to topologically incorrect prot...	96	14	14.6
GO:0014074	response to purine-containing compound	37	5	13.5
GO:0043279	response to alkaloid	31	4	12.9
GO:0006334	nucleosome assembly	50	6	12.0
GO:0006457	protein folding	114	13	11.4
GO:0006898	receptor-mediated endocytosis	68	6	8.8
GO:0006879	cellular iron ion homeostasis	25	2	8.0
GO:0007094	mitotic spindle assembly checkpoint	27	2	7.4
GO:0001666	response to hypoxia	95	7	7.4
GO:0071900	regulation of protein serine/threonine k...	160	10	6.3
GO:0045892	negative regulation of transcription	376	17	4.5

The annotated genes in the PERK-mediated unfolded protein response are summarized in Table 8. Also included in the table are the fold-count and p-values obtained from the AmpliSeq analysis. Of the annotated genes in the PERK-mediated unfolded protein response, 8 were shown to be up-regulated (FC > 1) and 1 down regulated. Six of the differentially regulated genes in this pathway were significant (p < 0.05). In this biological process, ATF3 was the most up-regulated gene in response to RS1-208b. Interestingly, some of its transcriptional targets are involved in

44

the intrinsic apoptotic signaling pathway in response to endoplasmic reticulum stress[61] (annotated genes, fold-count and p-values are summarized in Table 9). The analysis of the AmpliSeq data implicates RS1-208b as an inducer of the PERK-mediated unfolded protein response.

Table 8. PERK-Mediated Unfolded Protein Response (GO:0036499)

Gene ID	FC	p-Value
ATF3	96.70101	4.97E-100
HERPUD1	6.688471	1.25E-88
NFE2L2	1.720044	9.54E-08
CXCL8	*	*
IGFBP1	0.056119	0.9618482
EIF2S1	1.108594	0.4519698
EIF2AK3	2.34948	1.706E-11
ASNS	1.133256	0.2013979
CCL2	*	*
ATF4	1.975024	6.52E-14
DDIT3	*	*
HSPA5	2.191538	3.591E-16

5.3 PERK-Mediated Unfolded Protein Response and Intrinsic Apoptosis

The endoplasmic reticulum (ER) is one of the important membrane-bound organelles found in eukaryotic cells. The ER membrane, a single lipid bilayer, separates the cytosol from the ER lumen, where much of the folding of over one-third of all proteins occurs [62,63]. More precisely, proteins that are bound for the ER, Golgi apparatus, lysosomes, secretion, or the plasma membrane are translated into, and folded in, the ER lumen. These proteins contain a signal sequence on the N-terminal that targets them to the ER membrane while they are being synthesized on ribosomes[62]. The proteins are then co-translationally translocated into the ER lumen through a translocon complex, where the signal sequence in cleaved and translation is completed[62].

45

In the ER lumen, chaperones and co-chaperones aid in the folding of the polypeptide to achieve the correct native tertiary structure of the protein by binding to client proteins and avoiding foldings that are energetically unfavorable[64]. The process ensures that proteins destined for the ER, Golgi apparatus, lysosomes, secretion, and the plasma membrane are properly folded so they are able to function optimally further downstream.

However, in spite of the use of chaperones and co-chaperones, proper folding in the ER lumen is achieved under 20% of the time[62]. Proteins in the ER lumen that are unable to achieve the correct native structure are degraded through a process called ER-associated degradation (ERAD)[65,66]. Through ERAD, proteins are retro-translocated from the ER lumen into the cytosol, ubiquitinated, and degraded by the 26S proteasome[65,66]. A cell is understood to be experiencing ER stress whenever the folding capacity in the ER lumen is overwhelmed, which generally leads to an accumulation of misfolded proteins within the ER lumen[67].

Protein homeostasis (proteostasis) is tightly regulated in eukaryotic cells[68], with translation, folding, and degradation of proteins all being important components that maintain it. A cell experiences proteotoxic stress when it deviates from proteostasis; which occurs when one or more components are not functioning properly.

The unfolded protein response (UPR) is a highly conserved molecular signaling pathway that allows a cell to return to proteostasis (protein homeostasis) or undergo programmed cell death following proteotoxic stress[62,66,69–73]. The UPR can be initiated by one of three transmembrane proteins found in the ER that function as ER stress sensors: inositol-requiring enzyme 1α (IRE1α), pancreatic endoplasmic reticulum kinase (PERK), or activating transcription factor 6 (ATF6)[62,69,74]. IRE1α, PERK, and ATF6 all contain a luminal domain that is capable of either directly or indirectly sensing misfolded proteins in the ER lumen when the

46

misfolded protein levels surpass a threshold. The sensing of misfolded proteins leads to activation of downstream pathways following oligomerization of the sensor that can help a cell return to proteostasis or initiate programmed cell death[71].

The ATF6 arm of the UPR initiates when ATF6 located on the ER lumen binds misfolded proteins and translocates to the Golgi apparatus. There, it is subsequently cleaved by proteases at the transmembrane domain, and the cytosolic portion of the protein (ATF(N)) is released. The transcription factor then initiates transcription of UPR target genes that aim to increase the size and folding capacity of the ER, and thus, restore proteostasis[62,69,73].

IRE1α is associated with the ER chaperone BiP (binding immunoglobulin protein) on its luminal portion[62,73]. When BiP becomes dissociated, upon the misfolded protein threshold being reached in the ER lumen, IRE1α dimerizes and auto-transphosphorylates on the cytosolic tail, leading to the activation of RNase domain[62,73]. Under mild ER stress conditions, the RNase of IRE1α excises an intron 26 nucleotides long from the X-box protein 1 (XBP1) mRNA, which leads to the translation of the mRNA. XBP1 translocates to the nucleus and initiates the transcription of XBP1 targets that aim to restore proteostasis by increasing the size and folding capacity of the ER. When the stress is prolonged, the RNase degrades select mRNAs with the signal sequence in the N-terminal that targets them to the ER (including recently transcribed chaperone and co-chaperone mRNAs) as well as miRNAs that inhibit the translation of pro-apoptotic proteins, thus increasing ER stress and initiating programmed cell death[62,73].

The PERK-mediated branch of the UPR also begins with the dissociation of BiP from the luminal domain of the ER transmembrane protein PERK following the accumulation of misfolded proteins in the ER lumen, which allows for the dimerization of PERK on the cytosolic domain and trans-autophosphorylation[62,73,75]. Phosphorylation of PERK at threonine residue 980

47

and tyrosine residue 615 appear to be important for the initiation of this signaling pathway[76]. Activated PERK phosphorylates eukaryotic translation factor 2α (eIF2α) at serine residue 51[76–78] which provides cytoprotective effects by delaying global translation initiation to afford the protein folding machinery ample time to re-fold misfolded proteins and return the cell to proteostasis. Though phosphorylation of eIF2α can be accomplished by several eIF2 kinases[76], in the context of proteotoxic stress, PERK appears to be the dominant kinase (Ilustration 1).

The rate-limiting step in the synthesis of nascent polypeptides is translation initiation. eIF2, along with the 40S ribosomal subunit and other translation initiation factors, forms the 43S pre-initiation complex[76–78]. eIF2 facilitates translation initiation by recognizing start codons during the scanning process of transcripts and bringing the translation machinery to start codons when it is bound to GTP and Met-tRNA^{met}[78]. Following the recognition of the start codon, GTP is hydrolysed and eIF2 is released from the translation machinery, at which point GDP is exchanged for GTP, eIF2's affinity for Met-tRNA^{met} is restored, and the pre-initiation complex can form again to begin translation at the next start codon. Phosphorylation of the eIF2α subunit, such as that observed during proteotoxic stress, inhibits the rapid exchange of GDP for GTP, and thus reduces the machinery's ability to initiate translation[76,78].

Under proteotoxic conditions (such as those experienced during ER stress), despite global translation being delayed, mRNAs with upstream open reading frames (uORFs) are preferentially translated[78]. Activating Transcription Factor 4's (ATF4) translation is selectively upregulated during ER stress[62,73,79], which initiates transcription of several UPR targets (including chaperones, co-chaperones, and some XBP1 targets) to return to proteostasis[62,69,74]. Human ATF4 contains two uORFs. Under normal conditions, the quick GDP-GTP turnover of eIF2 allows for the re-formation of the pre-initiation complex by the time the scanning of the

48

transcript reaches the second uORF, which overlaps the ORF of ATF4. The products from both uORFs are quickly degraded. However, during ER stress conditions, the second uORF is bypassed by the translation machinery as GDP-GTP exchange is inhibited, allowing for the recognition of ATF4's ORF and the initiation of translation at the correct start codon, leading to increased expression levels of ATF4 as well as the transcription of its down-stream target genes, such as GADD34, which de-phosphorylates eIF2α when the cell returns to proteostasis[79], or phorbol-12-myristate-13-acetate-induced protein 1 (PMAIP1[68,79]).

Sustained ER stress leads to the transcription of ATF3, a bZIP transcription factor, by ATF4[76]. ATF4/3 are capable of forming heterodimers and transcribe PMAIP1[58,76,80], whose translated product (Noxa) has received recognition as an important mediator in a cell's commitment to apoptosis[81,82] (Illustration 2).

PMAIP1 is translated into Noxa, a pro-apoptotic, Bcl-homology domain 3 (BH3)-only member of the BCL2 family of proteins[82] that selectively binds MCL-1[83], an anti-apoptotic member of the same family. MCL-1 inhibits Bax (another pro-apoptotic member of the BCL2 family of proteins) oligomerization at the outer membrane of the mitochondria[83,84]. By targeting MCL-1 for degradation, Noxa effectively allows for the oligomerization of Bax and leads to the subsequent release of cytochrome c and calcium ions from the mitochondrial intermembrane space and caspase-3 dependent apoptosis[81,84–88] (Illustration 2 and Illustration 3). Silencing Noxa attenuates the cell death induced by proteotoxic stressors, pointing to its crucial role in mediating apoptosis under ER stress conditions[89].
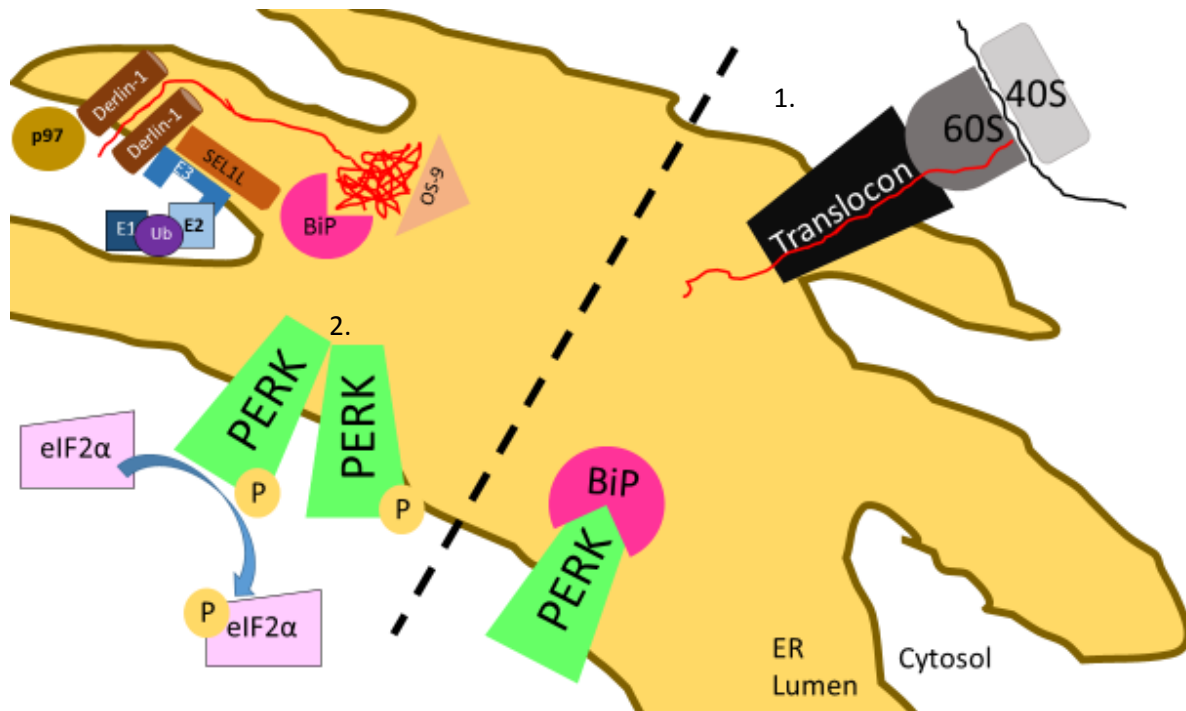
Illustration 1. Activated PERK Phosphorylates eIF2α

1. (Right) Peptides with an N-terminal sequence targeting them for the ER are translocated into the ER lumen and co-translationally modified. BiP normally binds the luminal domain of PERK when it is in excess (during proteostatic conditions). 2. Upon detection of misfolded proteins (left), BiP disassociates from PERK and participates in the retro-translocation of the misfolded protein. The misfolded protein becomes ubiquitinated and marked as it returns to the cytoplasm in an ATP-dependent manner. PERK is then able to dimerize and auto-transphosphorylate. Phosphorylated PERK then phosphorylates the eIF2α subunit, which inhibits GDP-GTP exchange and thus delays global translation under ER stress conditions.

Cytosol
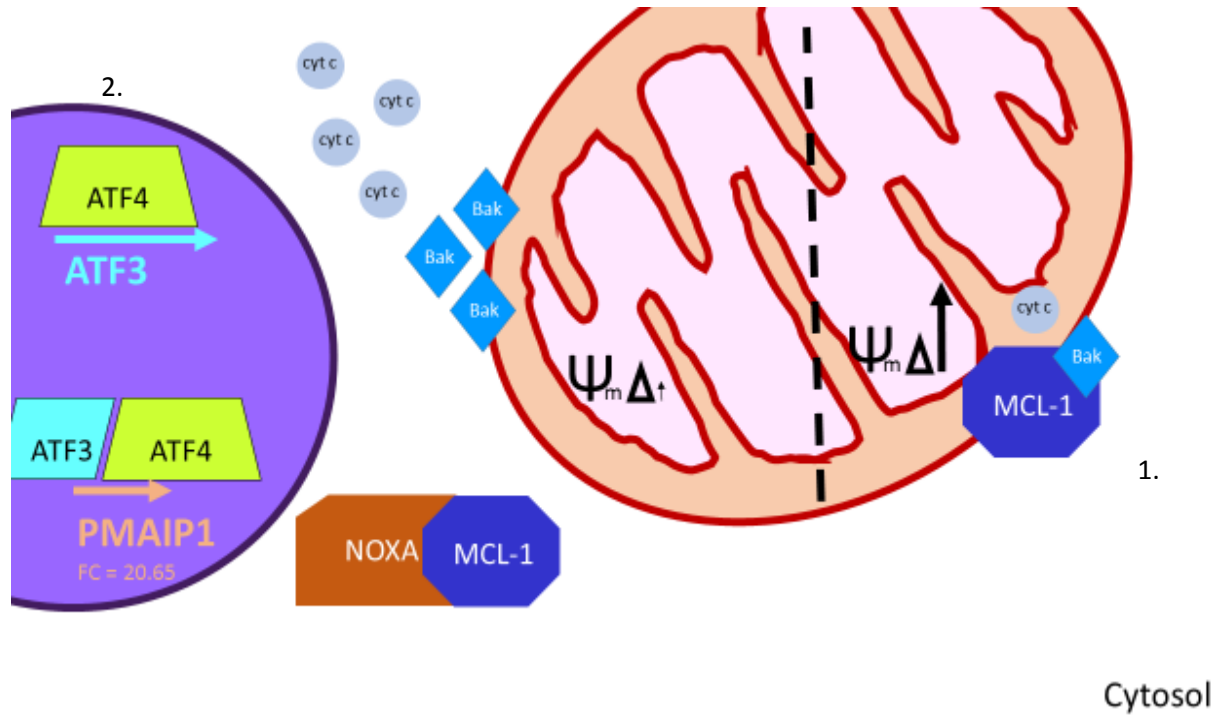
Illustration 2. ATF4/3 Up-Regulate PMAIP1

1. Under normal conditions (right), the mitochondrial transmembrane potential is maintained by the electron transport chain and cytochrome c is contained within the mitochondrial intermembrane space. MCL-1 inhibits Bak oligomerization at the mitochondrial outer membrane. 2. Under ER stress conditions (left), ATF4 transcripts are preferentially translated due to their uORFs. ATF4 transcribes ATF3, and they are thought to heterodimerize to transcribe PMAIP1. Noxa is the translated product of PMAIP1, and is crucial in initiating the intrinsic pathway of apoptosis when the cell is subjected to ER stress. Noxa selectively binds MCL-1, thus allowing oligomerization of Bak and leading to the release of cytochrome c into the cytosol and mitochondrial membrane depolarization.

51
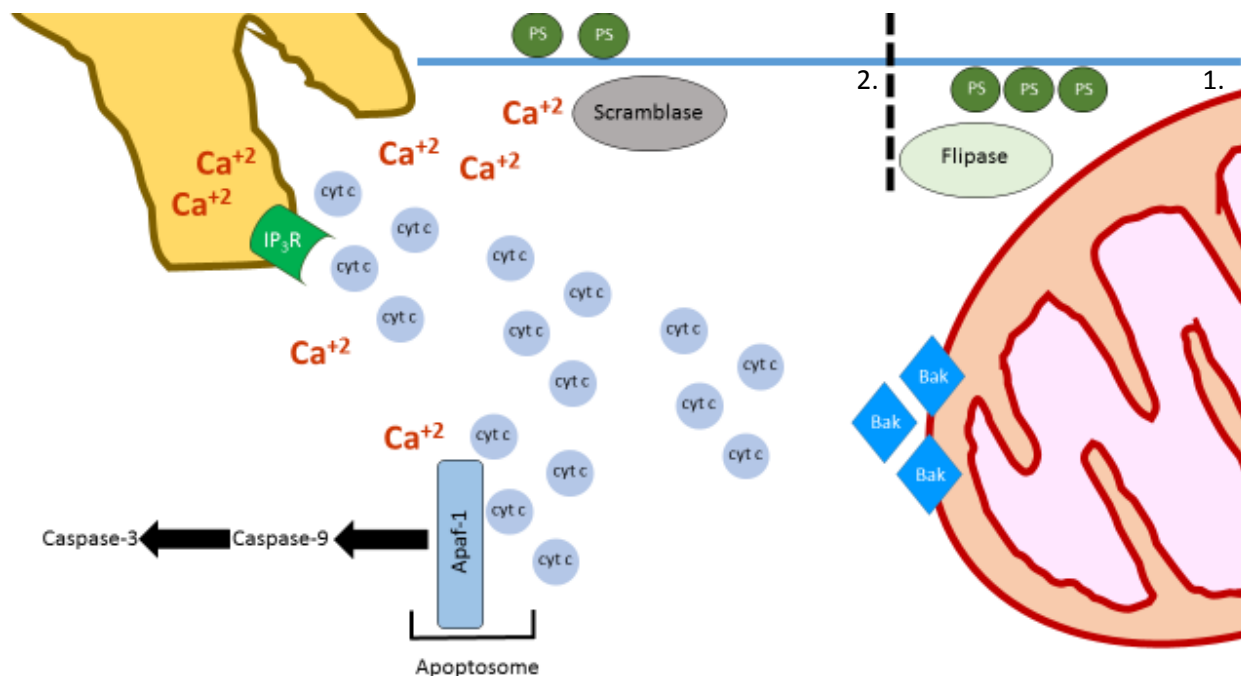
Illustration 3. Phosphatidylserine Externalization and Caspase 3 Activation Following Mitochondrial Depolarization

1. Under normal conditions (right), ATP-dependent flippases maintain phosphatidylserine asymmetry. 2. After the intrinsic pathway of apoptosis is initiated by oligomerization of Bak, cytochrome c released into the cytosol, along with Apaf-1, form the apoptosome, which leads to the activation of caspase-3. Also, cytochrome c acts as a ligand for IP$_3$R to release stored calcium ions from the ER lumen. The calcium ion increase in the cytosol activates calcium-dependent scramblases that externalize phosphatidylserine.

Table 9. Intrinsic Apoptotic Signaling Pathway in Response to Endoplasmic Reticulum Stress (GO:0070059)

Gene ID	FC	p-Value
BAX	0.849778	0.1435573
SELK	3.104602	1.01E-23
UBE2K	1.861324	2.70E-08
TRAF2	*	*
MAP3K5	*	*
TRIB3	5.074816	3.65E-65
ERO1L	*	*
ERN2	*	*
DAB2IP	*	*
CASP12	*	*
TNFRSF10B	2.300088	2.17E-09
PPP1R15A	29.9688	1.15E-150
CHAC1	51.29061	1.98E-156
PMAIP1	20.65687	3.90E-89
BCL2	0.789518	0.0978836

52

CASP4	1.288813	0.0178311
BRSK2	*	*
APAF1	1.884722	4.43E-08
ERN1	2.688022	5.28E-14
PML	0.913207	0.5029359
BBC3	*	*
DNAJC10	*	*
CEBPB	*	*
GSK3B	1.23268	0.0701281
ITPR1	1.11542	0.33162
ATF4	1.975024	6.52E-14
AIFM1	0.873896	0.1059551
TMBIM6	1.319751	0.0037422
XBP1	1.918808	4.81E-20
BAG6	1.072066	0.5245356
BAK1	0.863233	0.1873349
DDIT3	*	*
ATP2A1	*	*

ATF4, which initiates transcription of ATF3 (up-regulated 96-fold in response to RS1-208b, see Table 9) and heterodimerizes with ATF3 to transcribe PMAIP1[58,78–80], which is significantly up-regulated in response to RS1-208b (see Table 9). Its preferential translation under ER stress conditions increases the mRNA levels of its target genes ATF3 and PMAIP1. Of the genes involved in the intrinsic apoptotic signaling pathway in response to endoplasmic reticulum stress (see Table 9), PMAIP1 (up-regulated 20-fold in response to RS1-208b) is crucial for apoptosis to proceed[8184–86,90]. These three genes (ATF4, ATF3 and PMAIP1) are significantly up-regulated in response to RS1-208b, and provide a link between the PERK-mediated unfolded protein response (determined by GO enrichment analysis of the AmpliSeq data) and the intrinsic pathway of apoptosis induced by RS1-208b in hematological cancer cell lines that our *in vitro* assays had characterized.

6. Identifying the Molecular Target of RS1-208b

6.1 Connectivity Map Analysis

The cMAP was first introduced by the Broad Institute of Massachusetts Institute of Technology and Harvard University as a resource to help find connections between reference drugs (perturbagens) and mechanisms of action[91]. The cMAP was generated using a small panel of cell lines including MCF7 (breast cancer), PC3 (prostate cancer), HL-60 (AML), and SKML5 (melanoma)) and 164 perturbagens[91], though both the number of cell lines and the number of perturbagens have expanded since its initial implementation of cMAP. Gene expression profiles were collected from human cell lines treated with distinct small molecule perturbagens[91]. The collection is paired with a software to find patterns of gene expression that match the query and returns the perturbagen that most closely resembles the mechanism of action as the small molecule in question. Gene expression profiles in the collection were initially composed of microarrays with the data normalized to the vehicle control, though the collection is also compatible with whole transcriptome analysis. Two different time points were used in cMAP, with 6 hours after start of treatment representing a relatively early time point and a later time point, 12 hours after start of treatment, available for comparison[91]. We selected to use the 6 hour data to compare the molecular signature of RS1-208b to the collection of perturbagens given that we had characterized the intrinsic apoptotic pathway being activated by 5 hours.

The Broad Institute opted for a rank-based pattern matching system to avoid some of the drawback of hierarchical clustering, which would require that all gene expression profiles come from the same microarray platform[91]. This way, researchers are able to compare gene expression profiles obtained by microarrays or transcriptome analyses. Gene expression profiles from cells treated with novel small molecules are compared to the reference database and the output returns a file with the perturbagens ranked from the ones that most closely resemble the expression

54

profile in the query to the ones that have the least number of genes, either up- or down-regulated, in common.

Table 10. Molecular Signature of RS1-208b Compared to Perturbagens in cMAP

Rank	cMap_drug	KS_p-Value
1	MG-132[92–94]	4.6E-72
2	MG-262[95]	8.58E-72
3	PUROMYCIN[96]	1.2E-71
4	15-DELTA PROSTAGLANDIN J2[97]	2.07E-69
5	PARTHENOLIDE[98]	5E-62
6	PIPERLONGUMINE[99–101]	6.68E-62
7	DISULFIRAM[102]	9.6E-59
8	SECURININE[103]	1.5E-58
9	PHENOXYBENZAMINE	3.81E-54
10	CELASTROL[104]	3.14E-53
11	LANATOSIDE C[105]	8.71E-51
12	WITHAFERIN A[106]	1.22E-50
404	CURCUMIN	0.0000013

Table 10 ranks the perturbagens whose molecular signature is more like that of RS1-208b's. Of the top 12 compounds listed in the cMAP as being most similar to RS1-208b, 7 have been described to induce proteotoxic stress[92–106]. This supports the GO enrichment analysis of the biological pathways involved in apoptosis induced by RS1-208b by providing an upstream molecular target. Moreover, MG-132 and MG-262, which have molecular signatures most like that of RS1-208b induce cell death through a mechanism like RS1-208b by inhibiting the proteasome directly[92–95]. Therefore, we hypothesized that the proteasome was the main molecular target of RS1-208b and that the inhibition of the proteasome, and subsequent proteotoxic stress, initiates the signaling pathway that culminates in noxa-dependent apoptosis.

Chaperones in the ER lumen aid in the folding of nascent polypeptides but also regulate the decision to degrade terminally misfolded proteins[64,107]. Under ER stress conditions, ERAD

pathways involve the dissociation of BiP from IRE1α and PERK after the levels of misfolded proteins surpass the threshold that allows BiP to bind to terminally misfolded proteins[65,66].

Though the exact mechanism by which misfolded proteins are retro-translocated is not fully understood, OS-9, SEL1L, Derlin-1, and p97 are thought to be heavily involved in the process[62,65]. OS-9 and BiP transport the misfolded protein in the ER lumen to the ER membrane associated protein SEL1L. The misfolded protein is then retro-translocated through a channel composed of Derlin-1 proteins by the ATP-dependent p97[62]. The misfolded protein is then ubiquitinated through an E3 ubiquitin ligase with an ER transmembrane domain and tagged for degradation by the 26S proteasome (Illustration 1).

The UPS is an important component of the ERAD which degrades many of the misfolded proteins[65,66]. Following retro-translocation, the misfolded proteins are ubiquitinated and tagged for degradation through lysine residues[62]. Ubiquitination begins with E1 (ubiquitin-activating enzyme) activation of ubiquitin. Then E2 (ubiquitin-conjugating enzymes) transfers the activated ubiquitin from E1 to the target substrate (in this case, the misfolded protein that has been retro-translocated to the cytoplasm) through E3 (ubiquitin-protein ligase) binding of both E2 and target substrate. The misfolded proteins are subsequently deubiquitinated by the 19S regulatory particle prior to being catalytically cleaved by the 20S catalytic core particle.

Interference with the UPS has been shown to induce the UPR[66,108], though the mechanism by which the ER transmembrane proteins sense this interference is poorly understood. The use of Bortezomib, a small molecule that irreversibly binds to and inhibits the 26S proteasome[109], in the clinical setting demonstrates the effect proteasome inhibitors can have in combating cancer by selectively inducing apoptosis through the generation of proteotoxic stress. Proteasome inhibition results in the rapid accumulation of poly-ubiquitinated proteins, which triggers the

56

intrinsic pathway of apoptosis[93,109], and due to cancer cells having higher protein turnovers they tend to be especially susceptible to the proteotoxic stress induced. However, despite its success[109], there have been incidences of cells developing resistance to Bortezomib.

6.2 RS1-208b Inhibits the Proteasome Indirectly

Curcumin has recently been shown to circumvent acquired resistance to Bortezomib[110], suggesting that, given curcumin analogs' improved cytotoxicity profile, combining RS1-208b with other proteotoxic stressors could increase survival rates in high-risk cancer patients. One of the many molecular targets proposed for curcumin, and for which there is experimental evidence, is the proteasome[11,16]. *In vitro* evaluation of curcumin and several structural analogs revealed the decreased proteasome function[38].

The 26S proteasome is an important component of the ERAD that degrades misfolded proteins from the ER lumen that have been tagged with a chain of ubiquitin molecules[66]. Treatments with proteasome inhibitors increase proteotoxic stress and induce the unfolded protein response that results in apoptosis[58,66,79]. There are two major components of the 26S proteasome: the 19S regulatory particle and the 20S catalytic core. The 20S particle is responsible for cleaving proteins marked for degradation while the 19S regulatory particle binds these proteins and removes the poly-ubiquitin chain to increase efficiency of degradation[111]. Though curcumin and some structural analogs were shown to decrease the function of the 26S proteasome[38], follow up research indicates that the 20S core particle's catalytic activity is not adversely affected, with its caspase-like, trypsin-like, and chymotrypsin-like functions not being diminished following treatment with structural analogs of curcumin[112]. Instead, these analogs affect the proteasome by inhibiting the deubiquitination activity of deubiquitinases[112–114]

57

POH1, UCHL5[115,116], and USP14[117] are three deubiquitinases localized to the 19S regulatory particle that carry out the deubiquitinating activity of the 26S proteasome[112]. b-AP15 (3,5-bis[(4-nitrophenyl)methylidene]-1-prop-2-enoylpiperidin-4-one), a compound with similar molecular structure to RS1-208b, was shown to specifically inhibit the deubiquitinating activity of UCHL5 and USP14, two cysteine proteases associated with the 19S regulatory particle, but not the metallo-protease POH1[112]. Cysteine proteases, such as UCHL5 and USP14, contain a cysteine residue that is crucial for their catalytic function. It is thought that the thiolate in this catalytically crucial cysteine residue could interact in a Michael Reaction with the β-carbon of the α,β-unsaturated moiety[113] of curcumin analogs. Like b-AP15 and other monoketone curcumin analogs, RS1-208b contains two sites of conjugated α,β-unsaturated carbonyls[118] capable of acting as Michael Acceptors in Michael Reactions[113] with catalytic cysteine thiolates in the enzymatic activity pocket of deubiquitinases, leading to proteotoxic stress and the UPR (Figure 10).

Despite not directly inhibiting the catalytic activity of the 26S proteasome, the molecule b-AP15 has been described as an inhibitor of the UPS[113,112,118]. Targeted inhibition of both cysteine deubiquitinating enzymes UCHL5 and USP14 has been reported to lead to programmed cell death[114]. The microarray analysis of the expression profile of cells treated with b-AP15 is similar to those of proteasome inhibitors in cMAP[112]. Interestingly, b-AP15 selectively inhibits the deubiquitinating activity of the proteasome-associated cysteine deubiquitinases but not the overall deubiquitinating activity by cysteine proteases in the cytosol not associated with the 19S regulatory particle[112].

The molecular structure similarity between RS1-208b and b-AP15 (Figure 10) and the gene expression profiles suggesting their molecular mechanisms of action are similar, we

performed *in silico* experiments to compare their docking onto proteasome-associated cysteine deubiquitinases. b-AP15 docks onto UCHL5 and USP14 (near Cys88 and Cys114, respectively) to inhibit their deubiquitinating activity, presumably by inhibiting the catalytically active cysteine residue in each deubiquitinase[113,114,118].
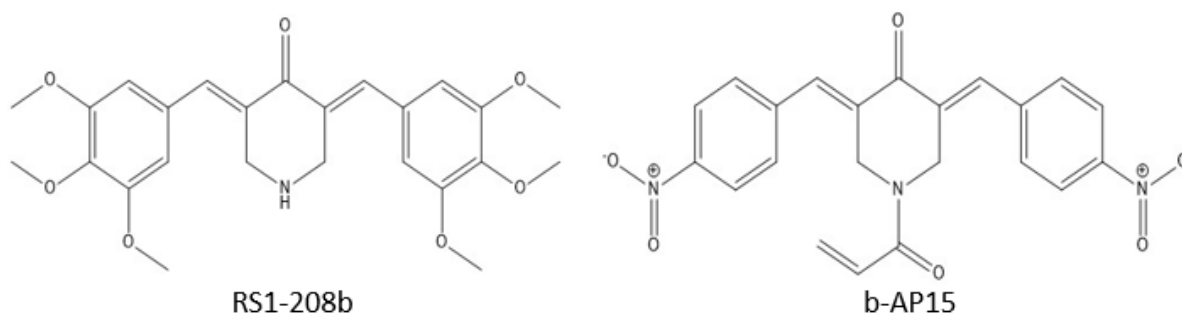
Figure 10. Molecular Structures of RS1-208b and b-AP15
RS1-208b and b-AP15 share structural similarity and have β-carbonyls sterically accessible to interact with thiolates in a Michael reaction.

Docking onto UCHL5 (PDB:3IHR[118]) was performed using Glide by Dr. Skouta's Lab. Comparison of docking scores between RS1-208b and b-AP15 (see Table 11) suggest RS1-208b is a more specific ligand for the pocket surrounding the catalytically active cysteine residue on UCHL5 (Figure 11a.). The functional groups on the aromatic rings and the aromatic rings themselves interact with several key amino acids surrounding the groove around Cys88 that help orient the β-carbonyl toward the cysteine residue (Figure 11b). The aromatic rings of RS1-208b are involved in pi-pi stacking with the phenylalanine in position 165 and the tryptophan in position 58. Moreover, hydrogen bonds form between the oxygen atoms on the functional groups on the aromatic rings of RS1-208b and phenylalanine in position 163 and tryptophan in position 58 and between the oxygen atom of the ketone moiety of RS1-208b and histidine in position 164 (Figure 11c).

59

Docking onto USP14 (PDB:2AYN) was performed using SiteMap by Dr. Skouta's lab. Docking scores comparing RS1-208b and b-AP15 indicate that for this docking site situated around the catalytically active cysteine at position 114 are summarized in Table 12. For USP14, b-AP15 is likely a better inhibitor of catalytic activity. Though RS1-208b can dock on the same pocket, albeit it with lower affinity (Table 12), the likely orientation of the molecule positions the β-carbonyl far from the Cys114 (Figure 12a). The effect of RS1-208b on USP14 is not as clear but since both cysteine deubiquitinases must be inhibited in order for the accumulation of poly-ubiquitinated proteins to occur[112], our working hypothesis is that on USP14 RS1-208b competes with ubiquitinated proteins for the site around Cys114 and in this way reduces its capacity to effectively cleave ubiquitin chains from proteins targeted for proteasomal degradation.

The *in silico* docking of RS1-208b onto proteasome-associated deubiquitinases provides a molecular target for the compound that is directly upstream of the signaling pathway (PERK-mediated unfolded protein response) that culminates in noxa-dependent apoptosis through the up-regulation of PMAIP1 transcripts, mitochondrial depolarization, and caspase-3 activation. RS1-208b occupies a groove that brings it in close proximity to the catalytic cysteine residue on UCHL5. This could bring the β-carbonyl in close enough range to interact with the thiolate functional group in Cys88 (Figure 11b.) via a Michael reaction that inactivates (reversibly) the deubiquitinase. However, the *in silico* docking onto USP14 showed that RS1-208b has less affinity for the pocket than b-AP15. Furthermore, the β-carbonyl of the compound is likely too far to interact with the thiol group of Cys114 in a Michael reaction (Figure 12a).

60
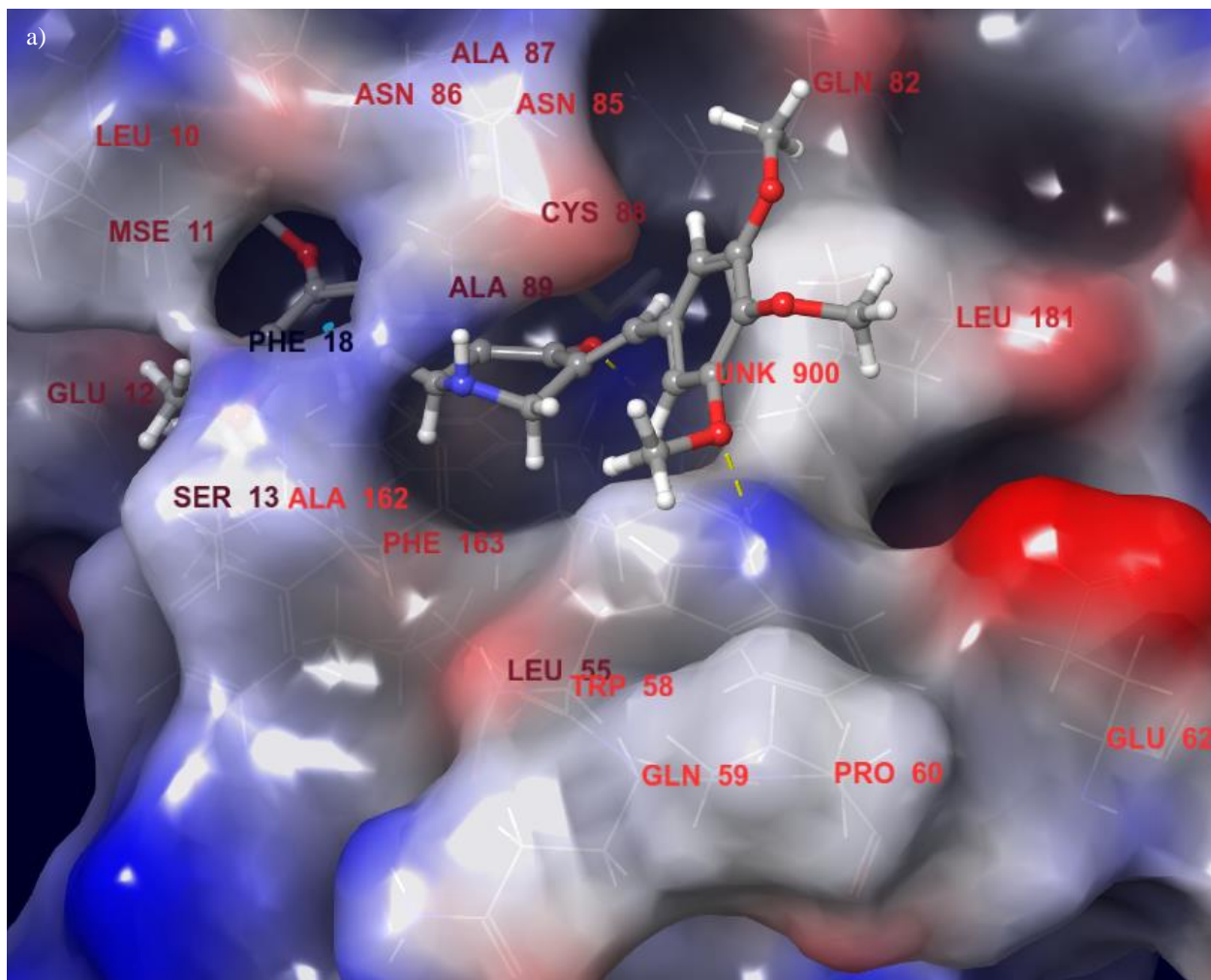
Figure 11. *In Silico* **Docking of RS1-208b onto UCHL5**
a) RS1-208b fits into the groove surrounding the Cys88 residue of UCHL5. The electrostatic colored surface is of UCHL5 is shown above to depict the groove where RS1-208b deposits itself.

61
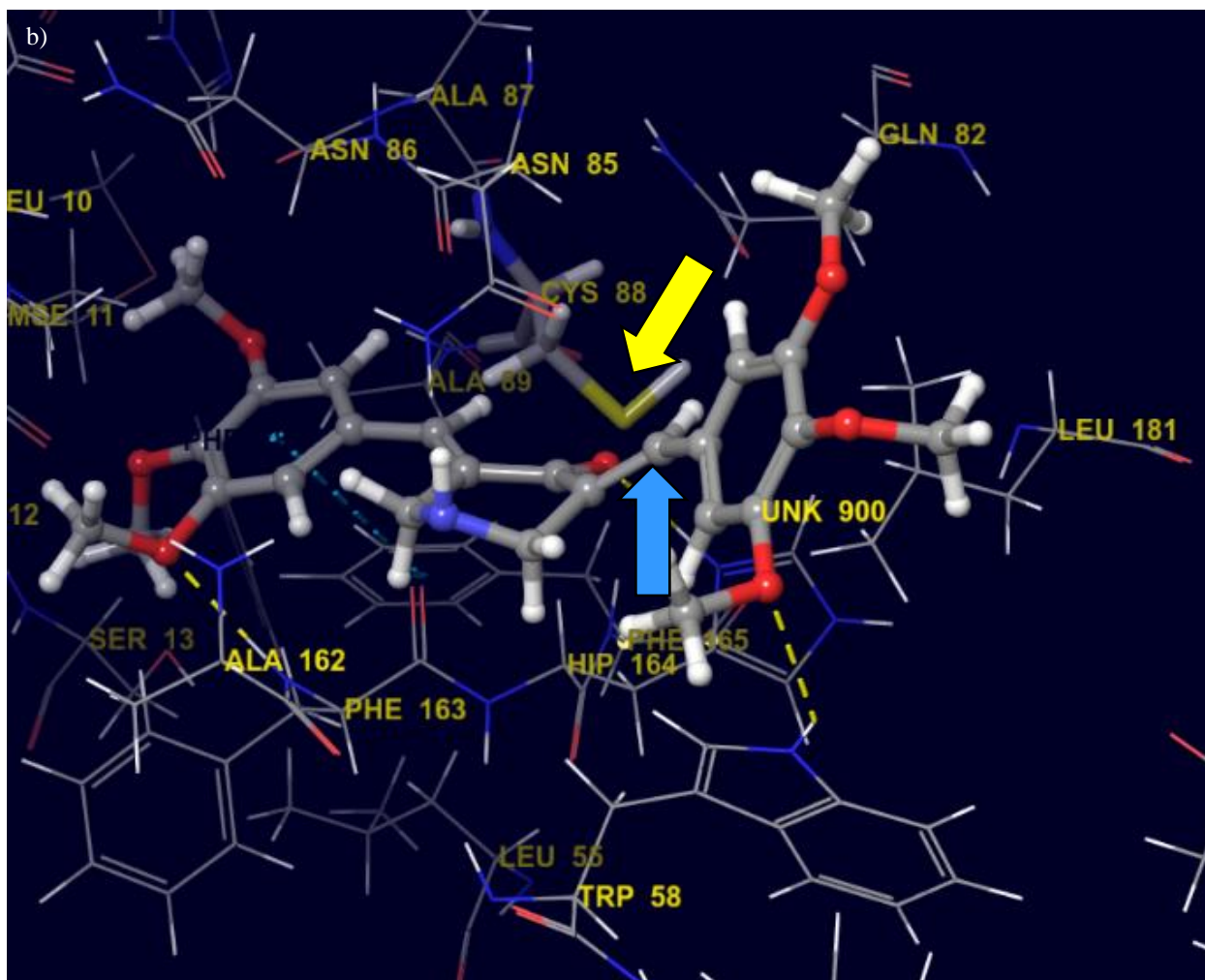
b) Docking of RS1-208b onto the groove surrounding the catalytically crucial Cys88 brings the β-carbonyl (blue arrow) in close proximity to the thiolate (yellow arrow).

www.manaraa.com

c)
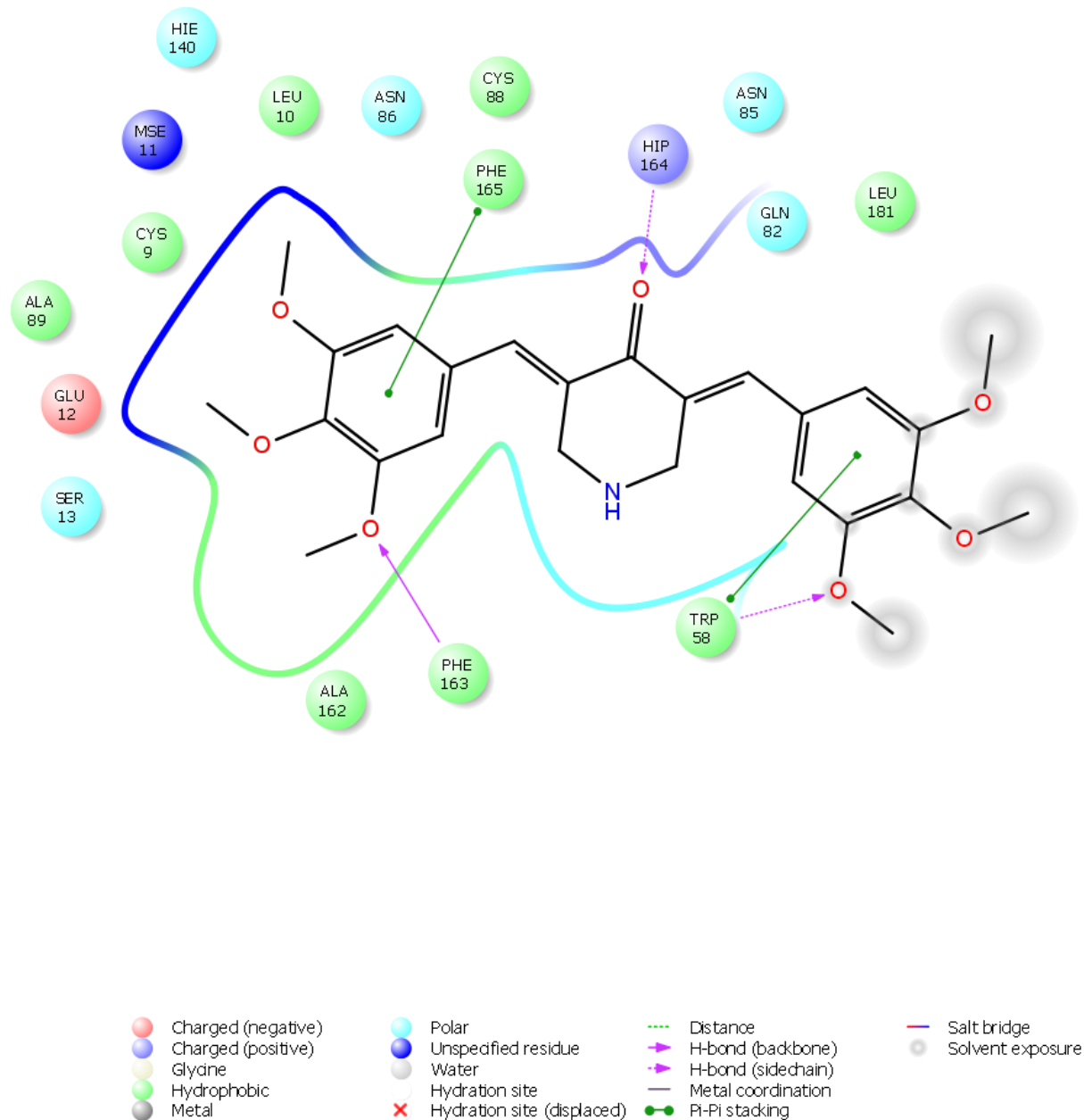
c) PHE165 and TRP58 involved in pi-pi stacking interactions with the aromatic rings of RS1-208b. PHE163 and TRP58 provide hydrogen bonds with the oxygen atoms of the functional groups on the aromatics rings. HIS164 forms a hydrogen bond with the ketone moiety.

Table 11. Docking Scores of RS1-208b and b-AP15 to UCHL5

Ligand	Docking Score
RS1-208b	-4.54
b-AP15	-3.30

63
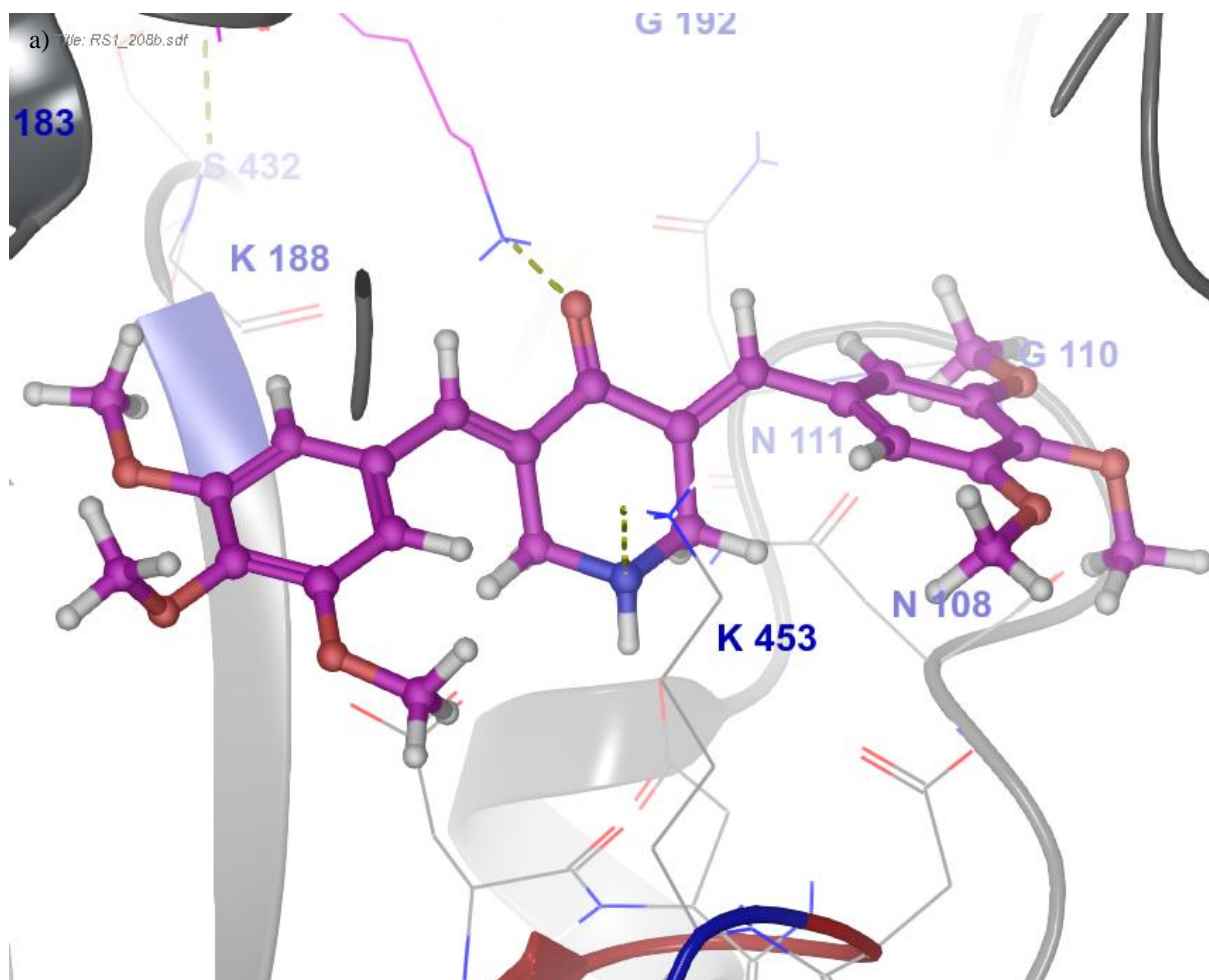
Figure 12. *In Silico* **Docking of RS1-208b onto USP14**
a) RS1-208b is capable of binding onto the groove of USP14 that surrounds the catalytic cysteine at position 114.

b)
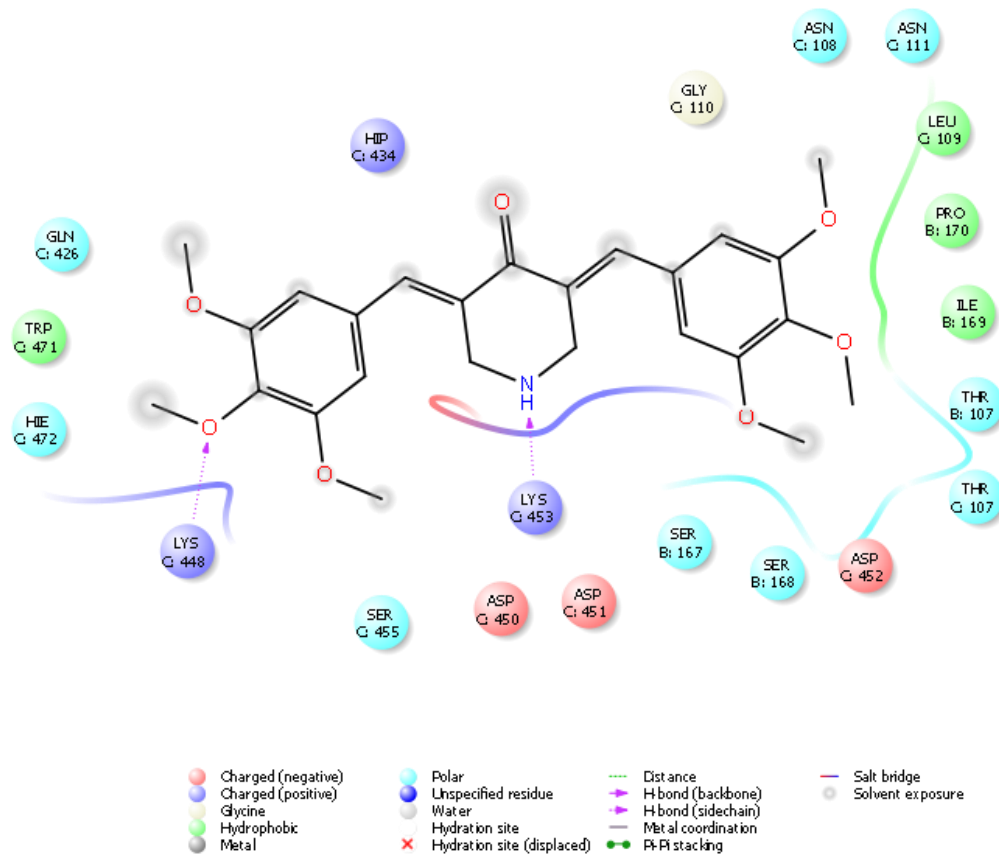
b) Lysine residues at positions 448 and 453 are involved in hydrogen bonding with the oxygen atom of the methoxy functional group on the aromatic ring and the nitrogen atom from the 4-piperidinone, respectively, stabilizing the molecule on the groove near Cys114.

Table 12. Docking Scores of RS1-208b and b-AP15 to USP14

Ligand	Docking Score
RS1-208b	-4.26
b-AP15	-5.12

7. Confirming Up-Regulation of Transcripts Using RT-qPCR

7.1 PMAIP1 Up-Regulation

The confirmation of up-regulation of transcripts induced in HL-60 cells by RS1-208b, detected through AmpliSeq analysis, was performed using real-time reverse transcriptase polymerase chain reaction (RT-qPCR). Due to Noxa's crucial role in apoptosis following ER stress[81,84–86,88–90], confirmation of PMAIP1 up-regulation was prioritized.

HL-60 cells (400,000 cells/2mLs/well in a 24-well plate) treated with either 2µM RS1-208b or PEG-400 (0.3% v/v) for 6 hours. Three separate experiments (each with 3 biological replicates per treatment) were conducted. The cell line and time point were selected for direct comparison to AmpliSeq data. Again, PEG-400 was selected as the vehicle control to minimize the effect contributed to the vehicle (see Figure 17.). Following treatment, cells were collected into micro-centrifuge tubes and centrifuged for 5 minutes at 1400rcf. Cells were then washed with ice cold PBS and centrifuged (5 minutes at 1400rcf), twice. PBS was aspirated and the dry pellet stored at -80ºC overnight. The following morning, RNA was extracted using Qiagen's RNeasy Mini Kit (74104), following the protocol provided, along with the optional Qiashredder (79654) and DNAse II digestion steps, to maximize RNA extraction and minimize DNA contamination. RNA quantification and purity assessment was performed using the NanoDrop. The results for individual replicates are summarized below (Table 13). A_{260}:A_{280} ratios above 2.0 and A_{260}:A_{230} ratios above 1.7 were taken to indicate successful RNA extraction and purity of RNA.

Table 13. RNA Extraction for RT-qPCR Shows High Purity

Sample ID	Sample Volume	ng/µL	260/280	260/230
PEG-400-1-1	30µL	126.94	2.09	1.77
PEG-400-1-2	30µL	111.37	2.13	1.87

PEG-400-1-3	30µL	103.92	2.12	1.81
PEG-400-2-1	30µL	82.86	2.07	2.02
PEG-400-2-2	30µL	57.47	2.00	1.84
PEG-400-2-3	30µL	63.01	2.06	2.04
PEG-400-3-1	30µL	90.87	2.07	2.22
PEG-400-3-2	30µL	65.18	2.04	1.94
PEG-400-3-3	30µL	77.43	2.00	1.87
RS1-208b-1-1	30µL	67.62	2.10	2.14
RS1-208b-1-2	30µL	71.93	2.12	1.79
RS1-208b-1-3	30µL	118.72	2.08	1.76
RS1-208b-2-1	30µL	77.06	2.03	1.92
RS1-208b-2-2	30µL	92.96	2.07	2.29
RS1-208b-2-3	30µL	65.86	2.06	2.09
RS1-208b-3-1	30µL	85.90	2.07	2.29
RS1-208b-3-2	30µL	92.39	2.05	2.18
RS1-208b-3-3	30µL	93.94	2.07	2.20

The synthesis of cDNA was performed using Qiagen's RT^2 HT First Strand Kit (330411) immediately following RNA extraction and purification. The genomic DNA elimination step, along with the DNAse II digestions performed during the RNA extraction and purification, reduces the possibility of DNA contamination. Total RNA used for each reaction was 500ng, with the volume adjusted to 9µL per reaction using nuclease free water. Reverse transcription was performed using Bio-Rad iCycler with the following program: 15 minutes at 42ºC, 5 minutes at 95ºC, hold at 4ºC.

Primers for the RT-qPCR verification of transcript up-regulation of select genes in response to treatment with RS1-208b were purchased from Bioneer. β-Actin (ACTB) was used as a control gene. The sequences of the primers used are found in Table 14.

Table 14. Primer Sequences Used in RT-qPCR Experiments

Gene	Forward Primer	Reverse Primer
ACTB[85]	5'-GGCACCCAGCACAATGAAG-3'	5'-GCCGATCCACACGGAGTACT-3'
PMAIP1[85]	5'-GCTGGAAGTCGAGTGTGCTA-3'	5'-CCTGAGCAGAAGAGTTTGGA-3'

67

The PCR reaction was performed in 0.2mL thin walled tubes. The reaction consisted of 12.5µL of 2x SYBR Green I, 3.5µL of each forward and reverse primer, 4µL of cDNA, and 1.5µL of nuclease free water. Total PCR reaction volume was 25µL. Final primer concentration was 700nM. Annealing temperature was determined for each set of primers using New England Biolab's Tm calculator (http://tmcalculator.neb.com/#!/). Primer sequence specificity was independently verified by Primer-BLAST (https://www.ncbi.nlm.nih.gov/tools/primer-blast/). The real-time PCR protocols used are summarized in Table 15. Melt curves were included to confirm target sequence amplification specificity (data not shown).

Table 15. Real-Time PCR Protocol

	Cycle(s)	Step	ACTB	PMAIP1
Initial Denaturation	1		95ºC:10(min)	95ºC:10(min)
PCR	40	Denaturation	95ºC:10(sec)	95ºC:10(sec)
		Annealing (Tm)	54ºC:10(sec)	53ºC:10(sec)
		Extension	72ºC:4(sec)	72ºC:4(sec)
Final Extension	1		72ºC:10(min)	72ºC:10(min)
Melt Curve	80		Start 54ºC (+0.5ºC)	Start 53ºC (+0.5ºC)
Hold	1		10ºC:∞	10ºC:∞

Analysis of up-regulation (fold-count) is summarized and compared to AmpliSeq in Table 16. Data represented below is the average (± standard deviation) up-regulation from three separate experiments (biological replicates = 3). ACTB was used as the housekeeping gene[85]. Fold-count up-regulation is normalized to PEG-400 (0.3% v/v) treated cells.

Table 16. Comparison of Up-Regulation Fold-Count (FC) between AmpliSeq and RT-qPCR

Gene	AmpliSeq (FC)	RT-qPCR (FC)
PMAIP1	20.66	14.91 ± 5.46

Though fold-count differed slightly between the two methods used to detect up-regulation of PMAIP1 transcripts, RT-qPCR confirms up-regulation of PMAIP1 in response to treatment of HL-60 cells with RS1-208b.

69

8. Evaluating Proteotoxic Stress and Noxa Translation Induced by RS1-208b

8.1 Accumulation of Poly-Ubiquitinated Proteins in Response to RS1-208b

Like the proteasome inhibitor Bortezomib, b-AP15 leads to the rapid accumulation of poly-ubiquitinated proteins[112]. However, b-AP15 does not inhibit either the caspase-like, trypsin-like, or chymotrypsin-like activity of the proteasome[112], suggesting b-AP15, and RS1-208b, could be a useful chemotherapeutic option for patients who initially respond well to proteasome inhibitors, such as Bortezomib, but develop resistance.

Enrichment analysis of AmpliSeq data (later confirmed through RT-qPCR) along with the *in vitro* assessment of apoptosis, which confirmed the intrinsic pathway induced by the compound, provided a signaling pathway that began with the ER response to stress and resulted in apoptosis. *In silico* docking of RS1-208b onto cysteine deubiquitinases UCHL5 and USP14 provided a molecular target of the compound that is upstream of ER stress. To confirm that treatment with RS1-208b lead to proteotoxic stress, which initiates the molecular signaling cascade we have observed, we performed immunoblot analysis to detect the accumulation of poly-ubiquitinated proteins[112–114] (proteotoxic stress) and link deubiquitinase inhibition to the PERK-mediated unfolded protein response.

Cells were incubated at a concentration of 200,000 cells/mL with either 2μM MG132, 2μM RS1-208b, or 0.3% v/v of PEG-400 and collected at 1 hour and 5 hours. Cells were then centrifuged at 1400rcf for 5 minutes and subsequently washed in PBS. Cells were then pelleted by centrifugation at 1400rcf for 5 minutes and the PBS removed by vacuum. Laemmli buffer (2x) was added to each pellet (150μL) in a micro-centrifuge tube and boiled at 100ºC for 10 minutes. The samples were then re-suspended in the Laemmli buffer by pipette and centrifuged at 1400rcf for 5 minutes. The supernatant was collected into a new micro-centrifuge tube and the samples were quantified using NanoDrop. Untreated cells were used as a negative control.

70

Accumulation of poly-ubiquitinated proteins following 1 hour of treatment was resolved using an 8% SDS-PAGE gel, run at 100 volts for 1 hour, and transferred to a PVDF membrane at 100 volts for 1 hour. The membrane was blocked overnight at 4ºC using 5% non-fat milk in TBS. The PVDF membrane was then probed with primary antibody against glyceraldehydy 3-phsphate dehydrogenase (GAPDH), used as a loading control, in 5% BSA-TBST(0.1%) for one hour at room temperature at a dilution of 1:1000. The secondary antibody (Goat anti-mouse) was incubated for 1 hour in TBS at a dilution of 1:2000, and the film developed. Primary antibody against ubiquitin was incubated at room temperature at a dilution of 1:1000. Goat anti-mouse was then incubated for 1 hour in TBS at a dilution of 1:2000, and the film developed.

The Un-SCAN It software was used to perform the densitometry analysis of the Western blots. Pixel counts for high molecular weight (> 250kDa) and ubiquitination of proteins (50kDa-250kDa) were normalized to the loading control, GAPDH, for every treatment. All treatments were then normalized to the untreated, negative control. The results are found in Figure 13.

The rapid accumulation of poly-ubiquitinated proteins has been observed as early as 1 hour following treatment with DUBs inhibitor b-AP15[112]. Treatment with RS1-208b showed a drastic change in the accumulation of high molecular weight (> 250kDa) poly-ubiquitinated proteins compared to MG-132 (see Figure 13a). The data presented below confirm RS1-208b's ability to inhibit, albeit, indirectly, the 26S proteasome.

71
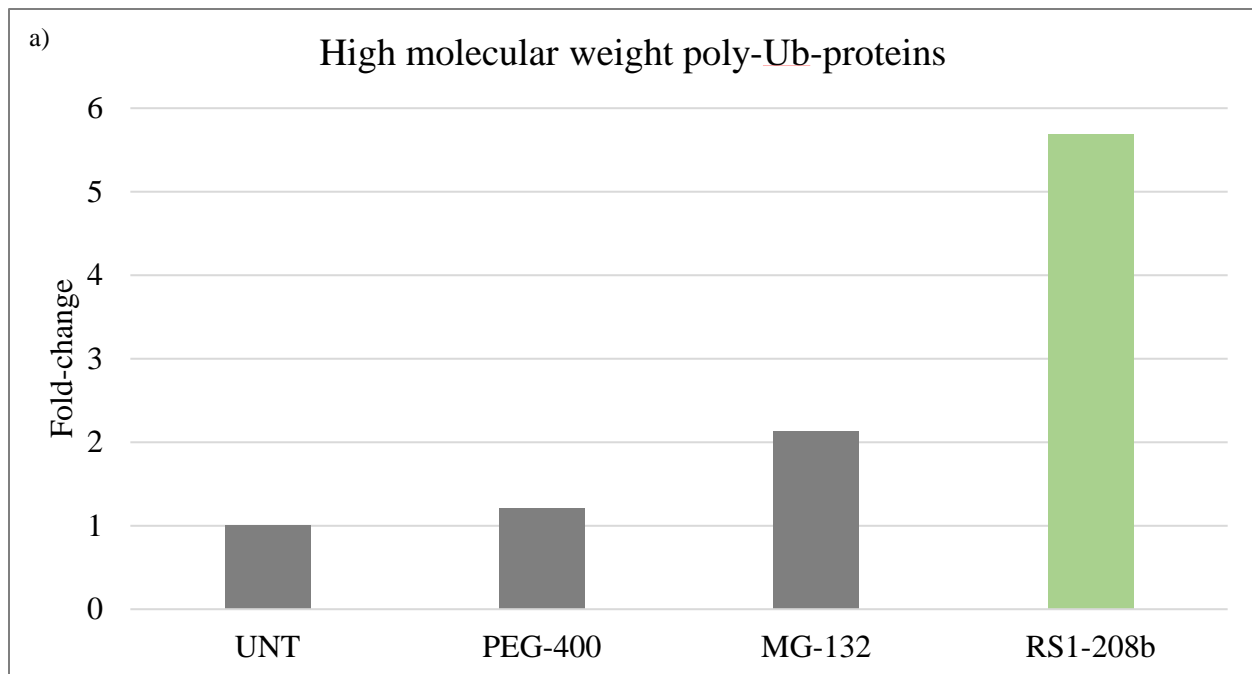
Figure 13. Accumulation of Poly-Ubiquitinated Proteins after 1 Hour of Treatment with RS1-208b

a) RS1-208b induces the rapid accumulation of poly-ubiquitinated proteins of high molecular weight (> 250kDa). This effect is greater than that observed with MG-132.
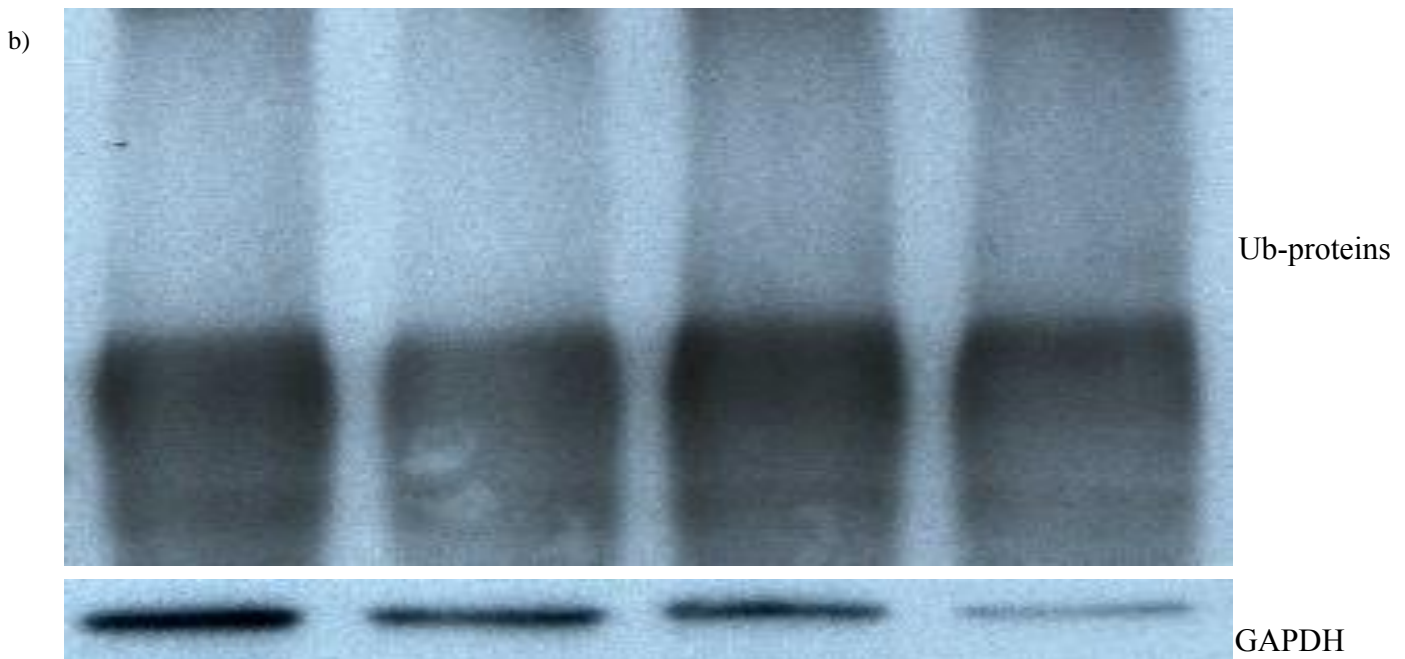
b) Western blot showing GAPDH and poly-ubiquitinated proteins. High molecular weight poly-ubiquitinated proteins were taken to be proteins weighing above 250kDa.
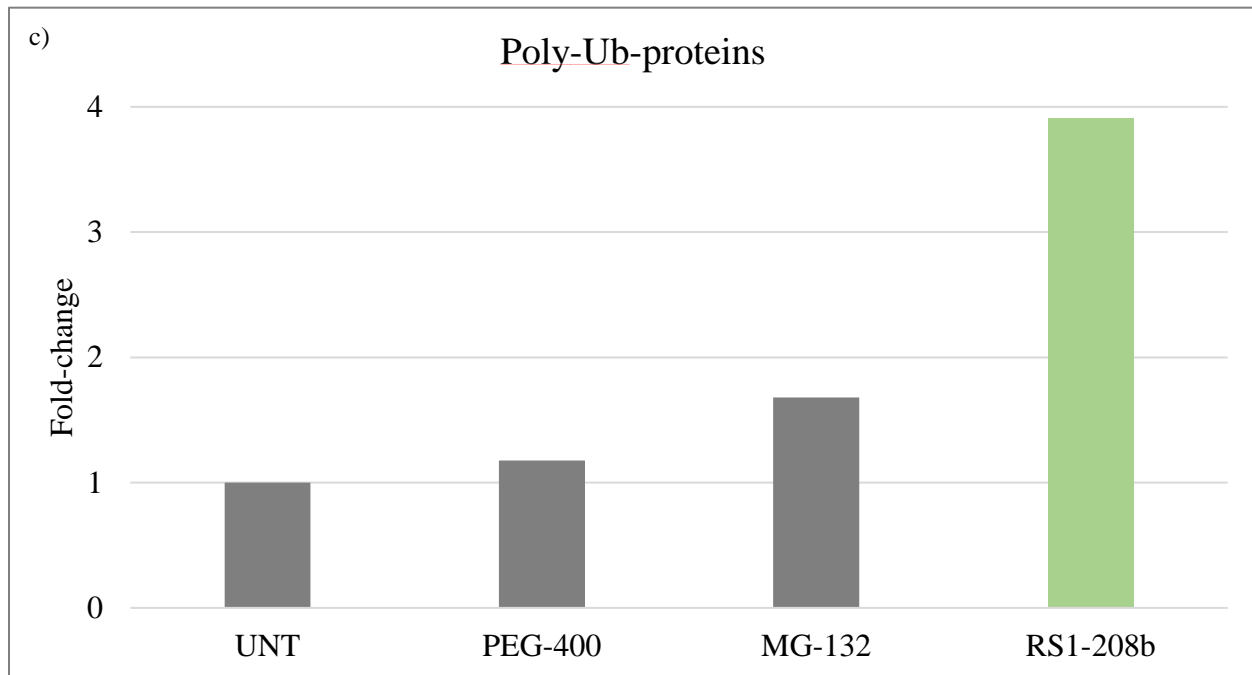
c) Fold-change of poly-Ub-proteins in response to DUB inhibition by RS1-208b after 1 hour. The observed accumulation of total poly-ubiquitinated proteins was markedly higher than treatment with MG-132. The vehicle control treatment was similar to the untreated controls.

8.2 Noxa Expression in Response to RS1-208b

Noxa selectively binds to and inhibits MCL-1[84], initiating the mitochondrial dependent intrinsic apoptotic pathway. Noxa has been shown to be a crucial factor in apoptotic death induced by proteotoxic stress[82,88,89].

Expression of Noxa as a result of ER stressors MG-132 and Bortezomib has been detected as early as 4 hours after treatment[88]. Due to the mitochondrial depolarization we observed in RS1-208b treated cells at 5 hours, we figured Noxa expression should be induced by this time point if we are observing Noxa dependent death. Furthermore, the 5 hour time point falls within the experimental observations of Noxa expression peaking between 4 and 8 hours after treatment[87].
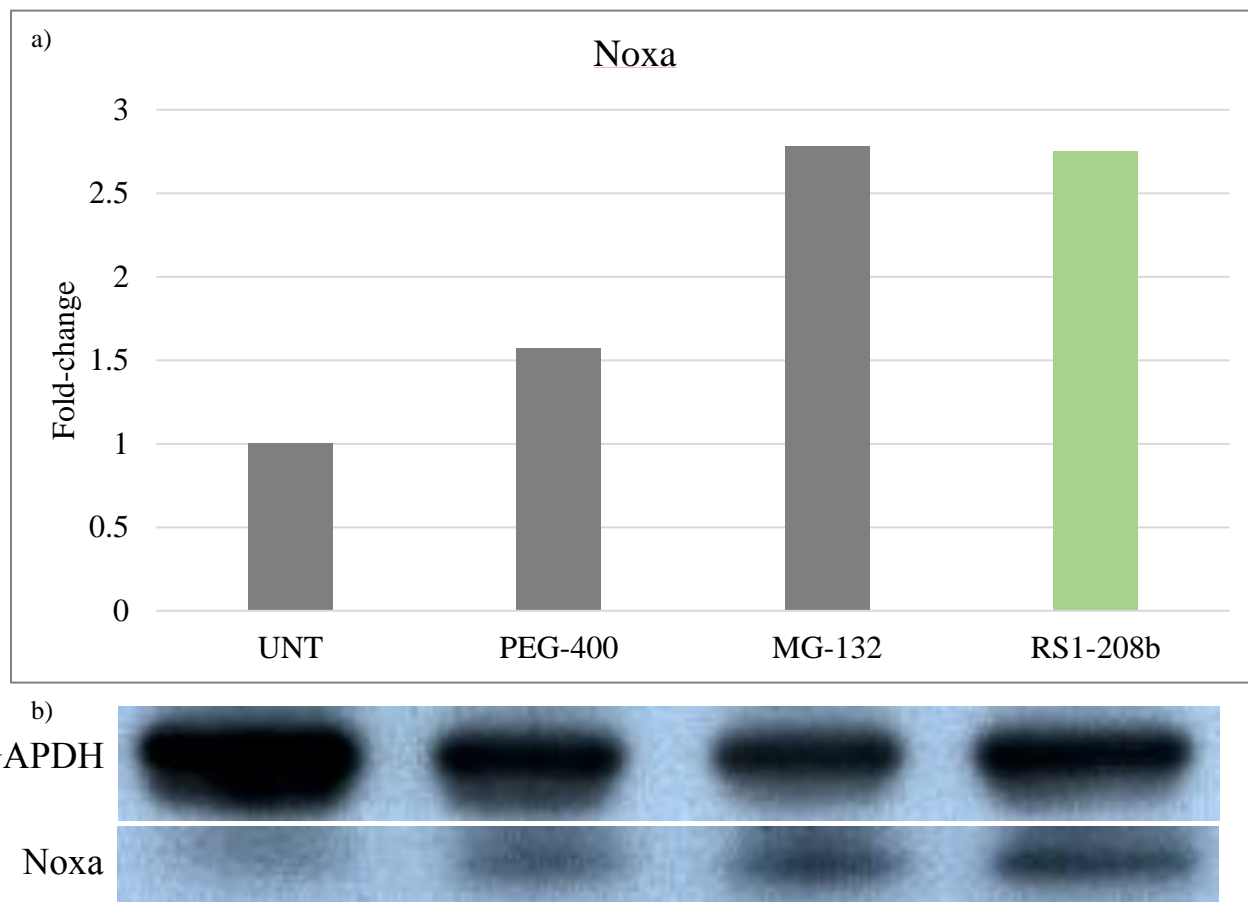
Figure 14. Noxa Up-Regulation after 5 Hours of Treatment with RS1-208b
a) Fold-change in Noxa expression following 5 hours of treatment. Noxa up-regulation of protein expression is comparable to the positive control, MG-132. Expression of Noxa was normalized to GAPDH, and all treatments were normalized to the untreated control. b) Western blot for loading control GAPDH and Noxa.

Cells were incubated at a concentration of 200,000 cells/mL and treated with either 2µM MG132, 2µM RS1-208b, or 0.3% v/v of PEG-400 and collected at 1 hour and 5 hours. Cells were then centrifuged at 1400rcf for 5 minutes and subsequently washed in PBS. Cells were then pelleted by centrifugation at 1400rcf for 5 minutes and the PBS removed by vacuum. Laemmli buffer (2x) was added to each pellet (150µL) in a micro-centrifuge tube and boiled at 100ºC for 10 minutes. The samples were then re-suspended in the Laemmli buffer by pipette and centrifuged at 1400rcf for 5 minutes. The supernatant was collected into a new micro-centrifuge

tube and the samples were quantified using NanoDrop. Untreated cells were used as a negative control.

Noxa expression was assessed at 5 hours after treatment. Noxa has been reported to peak between 4-8 hours after proteotoxic stress. Due to the mitochondrial depolarization observed at 5 hours after treatment, we hypothesized that by this time point, Noxa expression will be prevalent and that the subsequent inhibition on MCL1 allows for oligomerization of Bak.

Noxa expression was resolved using a 10% SDS-PAGE gel run at 100 volts for 1 hour, and transferred to a PVDF membrane at 100 volts for 1 hour. The membrane was blocked overnight at 4ºC using 5% non-fat milk in TBS. The PVDF membrane was then probed with primary antibody against Noxa in 5% BSA-TBST (0.1% Tween-20) for one hour at room temperature at a dilution of 1:1000. The secondary antibody (Goat anti-mouse) was incubated for 1 hour in TBST (0.1% Tween-20) at a dilution of 1:2000, and the film developed. GAPDH (loading control) in 5% BSA-TBST(0.1%) for one hour at room temperature at a dilution of 1:1000. The secondary antibody (Goat anti-mouse) was incubated for 1 hour in TBST (0.1% Tween-20) at a dilution of 1:2000, and the film developed. Primary antibody against ubiquitin was incubated at room temperature at a dilution of 1:1000. Goat anti-mouse was then incubated for 1 hour in TBST (0.1% Tween-20) at a dilution of 1:2000, and the film developed.

The Un-SCAN It software was used to perform the densitometry analysis of the Western blots. Pixel counts for Noxa were normalized to the loading control, GAPDH, for every treatment. All treatments were then normalized to the untreated, negative control. The results are found in Figure 14.

Noxa is constitutively expressed in hematological cancer cell lines[119]. Despite this, there was an appreciable increase in Noxa expression following treatment with either MG-132 or RS1-

208b. Moreover, densitometry analysis confirmed the up-regulation in expression in these treatments compared to the negative control. The fold-change calculated for MG-132 was 2.78 and for RS1-208b was 2.75, showing comparable Noxa expression between our compound and the positive control.

The expression of Noxa we observed at 5 hours could be what leads to the depolarization of the mitochondrial membrane induced by RS1-208b following DUB inhibition, accumulation of poly-ubiquitinated proteins, preferential translation of ATF4, and transcription of ATF3 and PMAIP1.

9. Evaluating RS1-208b *in Vivo*

9.1 Severe Compromised Immuno-Deficient (SCID) Mice and Cell Line Selection for *in Vivo* Studies

C.B-17/lcrHsd-*Prkdc^scid*, SCID mice, were selected for *in vivo* modeling due to their lack of functional T and B cells, which allow for xenotransplantation[120]. One female SCID mouse was injected subcutaneously ($5e^6$ cells suspended in 200µL of serum-free RPMI) on the right flank with RAMOS and on the left flank with BJAB in order to test the tumorigenicity and growth rate of the cell lines. There is no evidence suggesting the cell lines are capable of metastasizing when injected subcutaneously[121], therefore we attributed tumor growth as successful engraftment of the cell line, depending on which side of the mouse it grew.

The cytotoxicity assays performed identified Burkitt's Lymphoma as particularly susceptible to RS1-208b treatment. Furthermore, measuring tumor progression in subcutaneous models is more economically feasible, and less time consuming, than tracking disease progression of disseminated models and Burkitt's Lymphoma is a hematological malignancy that generally manifests itself in patients as a solid tumor. Both Burkitt's lymphoma cell lines (RAMOS and BJAB) have been reported to engraft subcutaneously in immune-deficient mice[122], though there are also studies which contradict the potential engraftment of BJAB[123]. The tumor growth rates appear to be similar from the palpable detection of a tumor to the time it takes to reach ~1500mm^3 [124].

In our hands, the BJAB model failed to engraft subcutaneously by day 28, consistent with several studies[123], whereas the Ramos model grew to ~1300mm^3 in that amount of time, and was palpable 20 days after inoculation of cells. We therefore selected the RAMOS cell line for xenotransplantation and *in vivo* modeling and evaluation of RS1-208b.

77

Table 17. Tumor Size after 28 Days

Cell Line	Tumor Volume (mm^3)
Ramos	1345.65
BJAB	0.00

Tumor Volume = *L x 2W x π/6*

9.2 Pilot Experiment-RAMOS Subcutaneous Model

Tumor cells grown in mice and serially re-passaged typically have better engraftment rates and the time from inoculation to measurable tumor is usually shortened[125]. Therefore, when conducting the pilot experiment to test the therapeutic potential of RS1-208b, the cells harvested from the previously mentioned experiment were selected for subcutaneous inoculation of 6 SCID mice (3 males and 3 females). However, we observed a markedly slower time to detection of palpable tumor (33 days compared to 20 days) and the time to ~1300mm^3 was 39 days (compared to 28 days), though the sample size does not allow for proper conclusions to be made. Despite this, the growth rate from when the tumors were first palpable to when they reached ~1300mm^3 in vehicle control mice was not drastically different to the previous experiment (5.5 days compared to 8 days). The engraftment rate for this pilot experiment was 66.67% (4/6; 2 males and 2 females).

Mice with palpable tumors were randomized on day 33 into vehicle (DMSO) control and treatment (RS1-208b 50mg/kg) groups, each containing 1 male and 1 female. We opted for intratumoral (IT) delivery to localize the biodistribution[126] of the compound and, theoretically, maximize the effect exerted. Vehicle control mice received 200µL of 10%v/v DMSO and the RS1-208b treated mice received 50 mg/kg in 200µL of 10%v/v DMSO intratumorally, a concentration that had previously been deemed safe (causing no discernable systemic toxicity) in an escalating dose pilot experiment using a syngeneic subcutaneous model of breast cancer. The

mice were treated 3 times a week after being weighed, examined visually for signs of systemic
toxicity, and having their tumors measured.
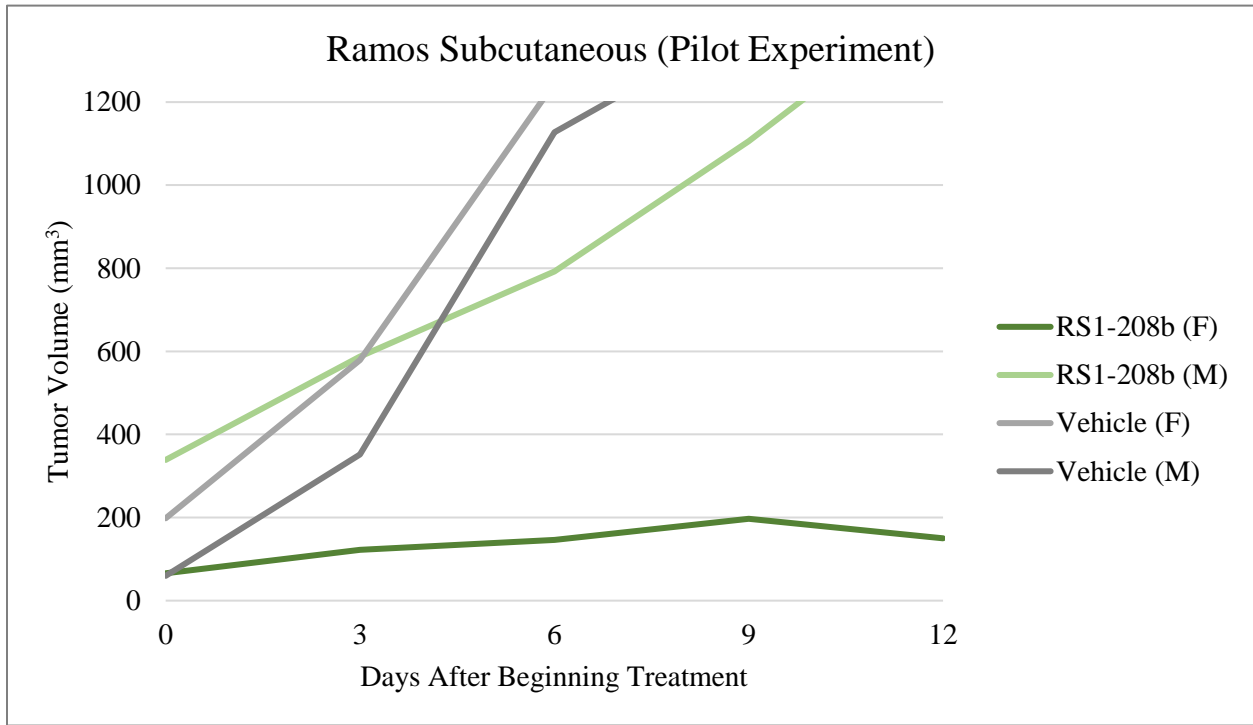
Figure 15. Pilot Experiment of Subcutaneous Model of RAMOS
The end-point for this experiment was >1200mm^3 or 12 days. RS1-208b doubled the number of survival days after initiation of treatment of compared to vehicle control mice. Vehicle control mice survived an average of 5.5 days after treatment initiation, whereas RS1-208b treated mice survived for 11.5 days. Sample size too small to determine statistical significance.

In the pilot experiment, we observed a delay in tumor growth rates in mice treated with
RS1-208b, with one tumor remaining below 200mm^3 for the duration of the pilot experiment.
The slower tumor growth rate allowed for longer survival (time to end point) compared to
vehicle control mice, though no statistical significance can be determined given the small sample
size.

9.3 Development of Intraperitoneal Model of RAMOS

Three SCID mice (2 females, 1 male) were injected intraperitoneally (IP) with 5e^6 cells
of the Ramos cell line suspended in 200µL of serum-free RPMI. The mice were weighed 3 times

a week and were visually inspected for intraperitoneal fluid or mass, indicative of successful

engraftment. All SCID mice (3/3) developed intraperitoneal tumors accompanied by a small

volume of ascites fluid formation by day 56 and were euthanized due to compromised

movement.
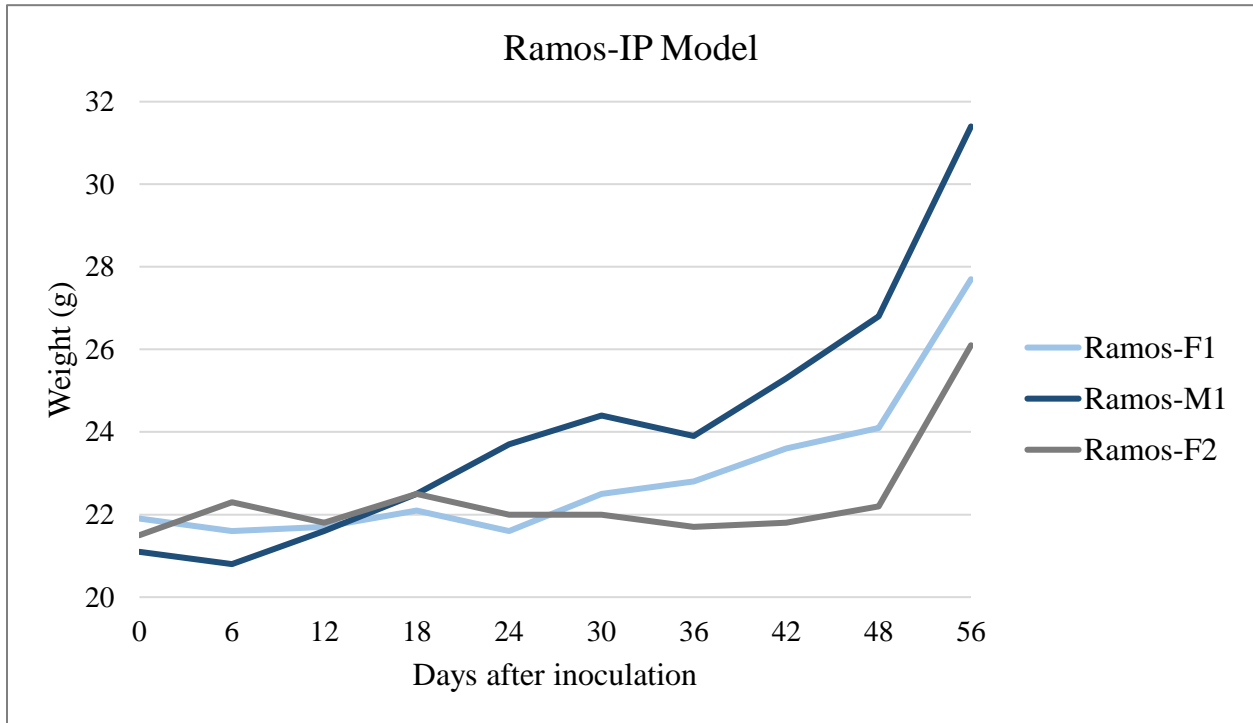
Figure 16. Weight Trends of Mice Injected Intraperitoneally with RAMOS
Weights remained steady for 24 days. Mice began gaining weight at a faster rate after day 36, which correlated with
IP tumor growth. Ramos-F1: female mouse 1, Ramos-F2: female mouse 2, Ramos-M1: male mouse 1.

The successful intraperitoneal engraftment rate of RAMOS provided us with yet another

in vivo model of the disease on which we could test the efficacy of RS1-208b. However,

detection of ascites fluid and tumor growth was not visually apparent until day about day 50,

providing only a small window for treatment, by which point the cancer burden on the mouse

could be too great to overcome. We therefore analyzed the weight trends to identify the point in

which the tumors and fluid could have begun to develop, which could be a proper point to begin.

After day 36, the mice began gaining weight at an increased rate, which we attributed to IP

80

tumor growth and ascites formation, suggesting that successful engraftment might have been achieved before this time point.

9.4 PEG-400 Selection for the Vehicle

Upon necropsis of pilot experiment mice, tumors treated with RS1-208b showed precipitated compound, indicating the formulation was coming out of solution *in vivo*. Despite this, in the RAMOS subcutaneous pilot experiment, an effect was observed in the treatment mice compared to vehicle controls and we attributed this effect to the compound.

To avoid using a higher percentage of DMSO and risking systemic toxicity due to the vehicle, polyethylene glycol 400 (PEG-400) was looked into as a more suitable vehicle for RS1-208b. PEG-400 has been used to dissolve compounds with poor solubility[127]. Furthermore, PEGs have been evaluated and found to be safe vehicles for drug administration and it is only at concentrations higher than are generally used in common practice that they exhibit systemic toxicity[128]. However, there are concerns when using PEG-400 intravenously or intraperitoneally due to its potential to induce hemolysis or reduce plasma volume, but not osmolality, at high doses (3.5g/kg-8g/kg), though the LD_{50} isn't observed until the concentration reaches 9.2g/kg[127]. For our modelling purposes, we decided to err on the side of caution and limit our use of PEG-400 to concentrations well below the LD_{50} reported and the concentrations where reduction of plasma volume begins to be a concern (9.2g/kg and 3.5g/kg, respectively).

PEG-400 is a viscous substance and we had trouble loading a syringe for injection. Therefore, we tested dilutions of PEG-400 in PBS (another inert vehicle) at 100% v/v PEG-400, 50% v/v PEG-400, 30% v/v PEG-400, and 10% v/v PEG-400 in order to determine at which concentration by volume it was feasible to load a syringe using a 28 gauge needle, selected to minimize discomfort to the mice at time of administration. Solutions containing <50% v/v PEG-

81

400 were able to be loaded into a syringe fitted with a 28 gauge needle with relative ease. We decided on using 30% v/v PEG-400 to help the compound remain in solution and minimize the amount of vehicle used.

Moreover, we diluted the compound using this solution prior to testing *in vivo* to ensure the compound remained in solution. We found that at a concentration of 5mg/kg the compound remained in solution but at higher concentrations, observable precipitation occurred even after vigorous vortexing. We next tested the 30% v/v PEG-400 formulation of RS1-208b for cytotoxicity compared to DMSO using the PI exclusion assay on a small panel of hematological cancer cell lines at 1% concentration of final volume. Overall, we observed a greater cytotoxic effect when using DMSO ($p < 0.05$) as the vehicle control, indicating that perhaps PEG-400 was a more suitable vehicle for studying the cytotoxic effects of RS1-208b by minimizing the effect of the vehicle (see Figure 17).
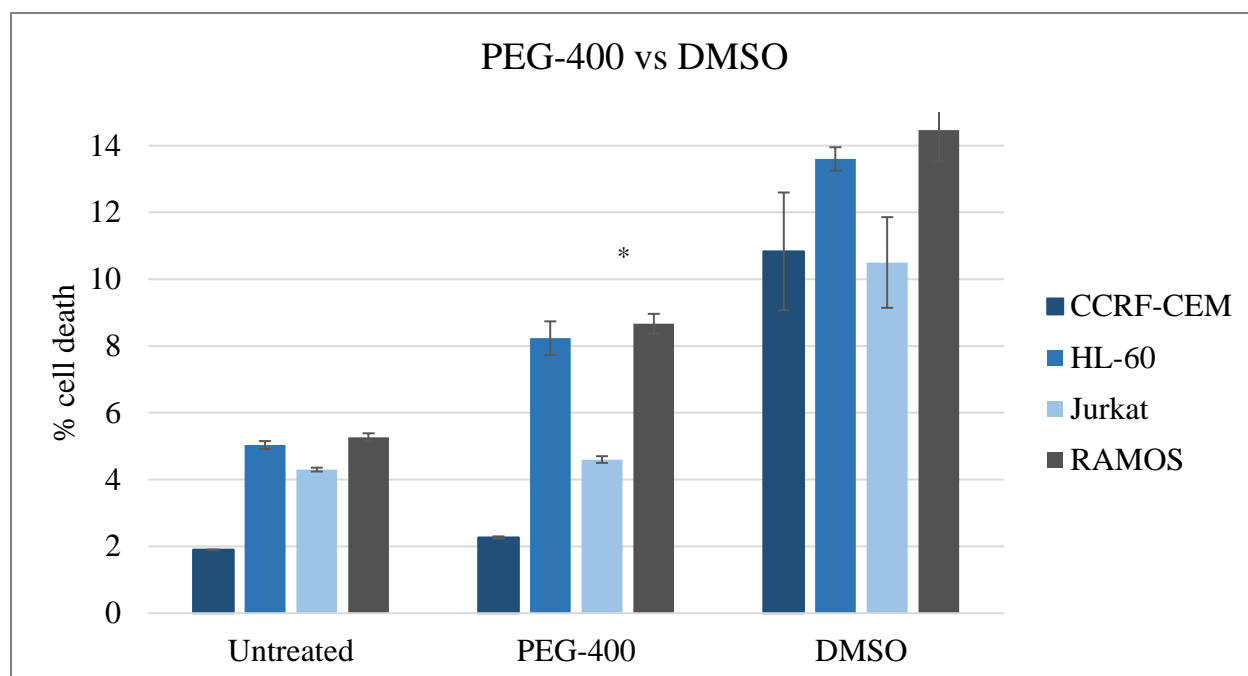
Figure 17. Assessment of Cell Death Induced by Vehicles PEG-400 and DMSO
The cytotoxic effects of the two vehicles were assessed in four different hematological cancer cell lines. PEG-400 exhibited less cytotoxicity than DMSO after 24 hour treatment ($p < 0.05$).

9.5 RAMOS Subcutaneous Model

Curcumin and EF-24 have been tested on mice bearing subcutaneous tumors[39], with minimum effective dose calculated to be 20mg/kg[33,129]. However, we were unable to dissolve RS1-208b in the 30% v/v PEG-400 formulation at a concentration higher than 5mg/kg. Encouragingly, SCID mice bearing FaDu tumor xenografts treated with b-AP15 (5mg/kg) through subcutaneous injection showed a significant delay in tumor growth when compared to vehicle[112]. This suggested that even at these lower concentrations, given RS1-208b's structural similarity to b-AP15 and its improved cytotoxicity profile compared to both EF-24 and curcumin, we would be able to achieve tumor growth delay.

RAMOS cells obtained from a previous subcutaneous engraftment were injected into SCID mice (n = 19). The mice were randomized into an RS1-208b treatment group (n = 10) and a vehicle control group (n = 9) when the tumors reached ~200mm^3. After the tumors reached this

size, they were dosed 3 times a week with 5mg/kg[112] RS1-208b or vehicle and tumor

measurements (Tumor volume = $L\ x\ 2W\ x\ \pi/6$) and mouse weights were taken 3 times a week.

The end point selected was tumor volume >1200mm^3. Compound stability was assessed via

mass spectrometry before the initiation of *in vivo* modelling (data not shown).
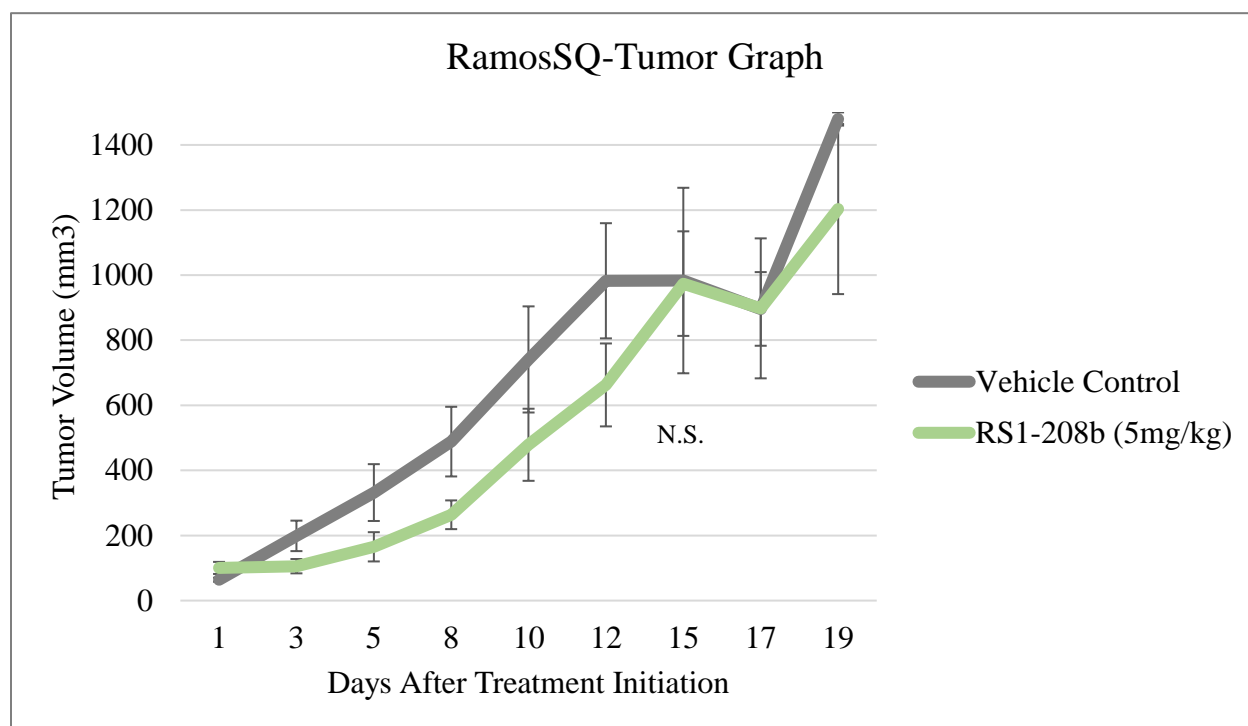
Figure 18. RS1-208b Delays Tumor Growth in RAMOS Subcutaneous Model
RS1-208b delays the tumor growth for 12 days. Tumor growth progression (± SEM) is shown above. No statistical significance was observed between RS1-208b treated and vehicle treated tumors at each measuring point, though there was an apparent delay in tumor growth, with RS1-208b treated tumors measuring, roughly, between ½ and 2/3 of the vehicle treated for 12 days.

Table 18. Ratio of Tumor Growth Comparing RS1-208b Treated Mice with Vehicle Treated Mice in Subcutaneous Model of RAMOS

Days After Treatment Initiation	RS1-208b/Control
3	0.53
5	0.49
8	0.54
10	0.65
12	0.67
15	0.99

84

www.manaraa.com

Though not statistically significant, there was an appreciable delay in RAMOS tumor growth between RS1-208b treated and vehicle treated mice that lasted through the first 12 days of treatment. The ratio of RS1-208b to vehicle treated tumor size at each measuring point was between ½ and 2/3 for the first 12 days.
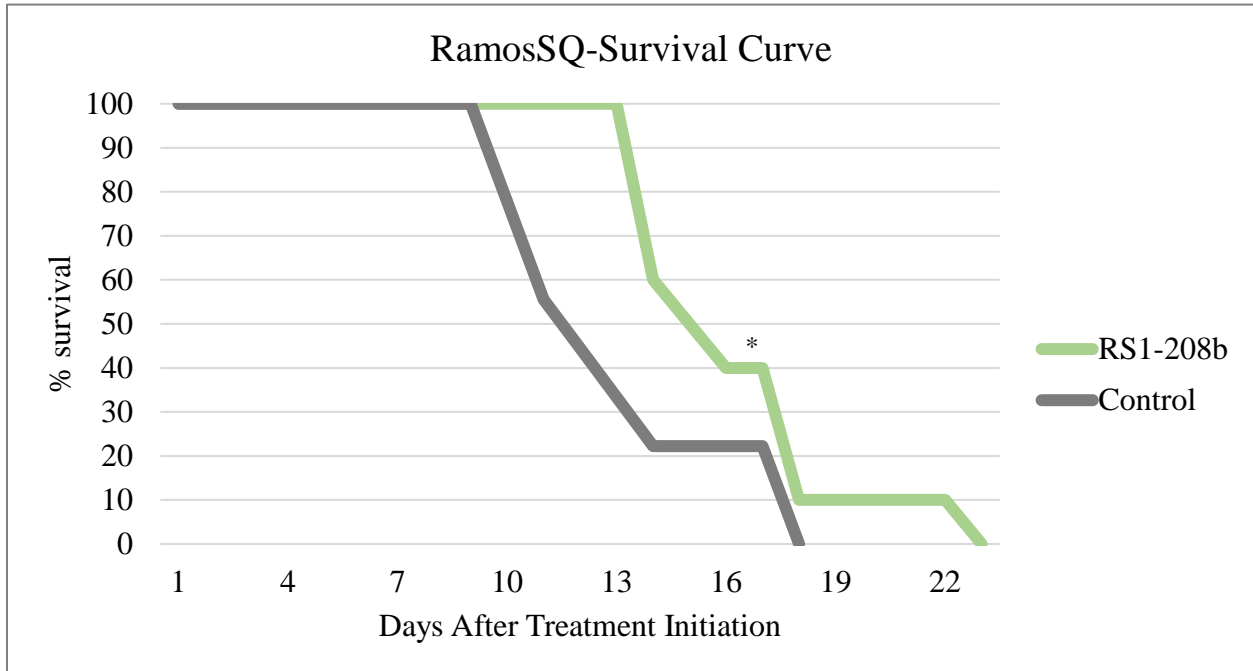
Figure 19. RS1-208b Extends Event-Free Survival Time in RAMOS Subcutaneous Model
RS1-208b extends event-free survival time in RAMOS subcutaneous model ($p < 0.05$). Median event-free survival for vehicle treated mice was 11 days compared to 14.5 days for RS1-208b treated mice.

The Kaplan-Meier survival curve (Figure 19) shows treatment with RS1-208b on the RAMOS subcutaneous model significantly ($p < 0.05$) increased event-free survival, as measured by the Chi-Square test. Though not statistically significant when compared to vehicle control tumor size, the delay in tumor growth observed in RS1-208b treated mice lead to a significant increase in the number of mice surviving past the expected number of days established by the vehicle control.

85

9.6 RAMOS Intraperitoneal Model

Ramos cells obtained from previously successful intraperitoneal engraftment were injected intraperitoneally into the lower right quadrant of SCID mice (n=9). Mice were randomized into RS1-208b treatment and vehicle control groups 24 days after the injection, at which point, treatment began: 10µM RS1-208b (n = 5) or vehicle (n = 4), delivered 5 times a week intraperitoneally. Mice were visually inspected daily for behavioral and body condition score changes. Furthermore, the mice were weighed 3 times a week to track tumor engraftment. The end point selected was 30% weight gain (compared to initial average weight), before tumor burden compromised quality of life, or appreciable drop in body condition score.
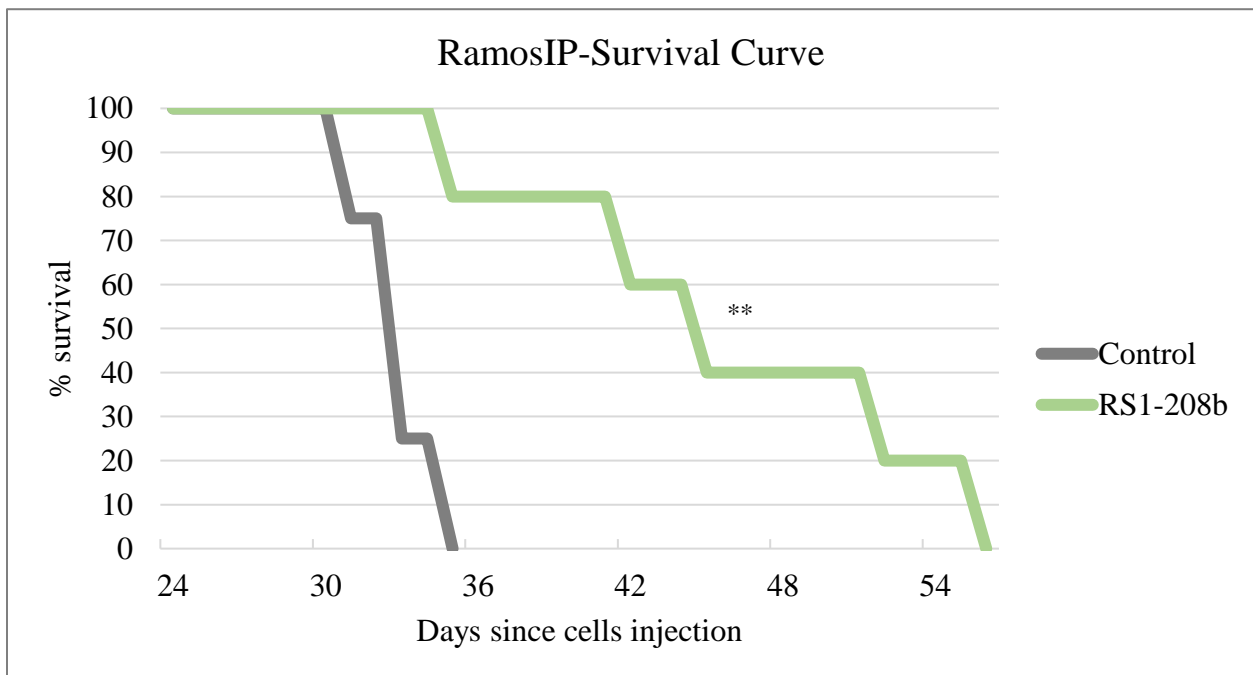
Figure 20. RS1-208b Extends Event-Free Survival Time in the RAMOS Intraperitoneal Model
RS1-208b significantly ($p < 0.005$) increases event-free survival in the RAMOS intraperitoneal model. Median survival for vehicle treated mice was 33 days compared to 46 days median survival for RS1-208b treated mice.

The median survival time was increased in the RS1-208b treated mice by about 50% compared to vehicle control (see Figure 20). The event-free survival time difference between RS1-208b treatment and vehicle control group was very significant (p < 0.005).

Despite being about 1/10 of the dose used in the subcutaneous model of RAMOS, the effect in the intraperitoneal model was much more pronounced. Method of delivery would be a potential explanation for the increased efficacy in the intraperitoneal model. However, despite delivering RS1-208b intraperitoneally, there were solid tumors in the peritoneal cavity upon necropsis, suggesting the delivery could also be considered intratumoral. We hypothesize that the increase in efficacy is due largely to the increased frequency of RS1-208b doses. The rapid systemic clearance of curcumin[19] could also affect its analogs, suggesting more frequent and smaller doses could be more effective in treating cancers *in vivo*.

10. Conclusion

10.1 Discussion

RS1-208b inhibits the deubiquitinating activity of cysteine DUBs that associate with the 19S regulatory particle of the 26S proteasome. *In silico* docking of RS1-208b onto UCHL5 indicates the aromatic rings and the functional groups that surround it, along with the ketone moiety of the compound, orient RS1-208b so that the unsaturated β-carbonyl comes in close proximity to the catalytically crucial cysteine residue, and, presumably, initiate a Michael reaction with the thiol group[38]. However, the effect on USP14 is likely due to the compound competing with ubiquitin chains for the pocket surrounding the catalytic Cys114 since the orientation we observed through *in silico* docking experiments suggest the unsaturated β-carbonyl does not come in close proximity to the cysteine's thiol group. The inhibition of deubiquitinating activity results in the accumulation of poly-ubiquitinated proteins within 1 hour of treatment which induces proteotoxic stress and initiates a cellular signaling cascade that culminates in apoptosis.

Though the exact mechanism by which proteasome inhibition leads to the PERK-mediated unfolded protein response is not clearly understood[62,65], data analysis of our AmpliSeq results indicated that the PERK-mediated UPR is activated in HL-60 cells following 6 hours of treatment with RS1-208b. Activated PERK is a kinase that phosphorylates eIF2α, an important subunit of the 43S translation initiation complex whose phosphorylation inhibits the rapid exchange of GDP-GTP, essentially halting global translation. Under these conditions, transcripts with uORFs are preferentially translated. ATF4 is one such transcript with two uORFs whose preferential translation during ER stress conditions is important for the transcription of PMAIP1. Noxa, the translated product of PMAIP1, crucial for the intrinsic apoptotic pathway[82], selectively binds the anti-apoptotic protein of the Bcl-2 family MCL-1, releasing MCL-1's inhibitory effect

88

of Bak[82,84]. This allows for Bak oligomerization, which leads to the depolarization of the mitochondrial outer membrane and the release of protons, cytochrome c, and calcium ions into the cytosol. Cytochrome c, along with Apaf-1, combine to form the apoptosome, cleaving and activating caspase-9, which in turn activates the effector caspase, caspase-3, resulting in cell death. Furthermore, cytochrome c acts as a ligand for the inositol triphosphate receptor on the ER membrane, leading to more calcium ion release into the cytosol. Calcium dependent scramblases externalize phosphatidylserine to signal that the cell is undergoing apoptosis and allow for recognition by macrophages.

In vivo assessment of the effects of the compound indicate RS1-208b is very well tolerated at concentrations up to 50mg/kg and that it has a positive effect in extending event-free survival time in two different xenograft models, even at low concentrations.

These results suggest treatment with RS1-208b could be a legitimate alternative chemotherapeutic option, especially for high-risk leukemia cases in the U.S. Hispanic population, whose disproportional mortality rates due to childhood cancers highlight the need for improved chemotherapy options. Moreover, RS1-208b could be used in cases where patients initially respond favorably to proteasome inhibitors but develop resistance by offering an alternative which results in the same pathway of cell death but targets deubiquitinases.

In addition, the low systemic toxicity we observed, along with its inhibition of inflammatory cytokines IL-6[36] and TNFα emphasizes RS1-208b's ability to be used in combination therapy, though preliminary *in vitro* data hasn't shown a synergistic effect with established chemotherapy compounds (data not shown).

89

10.2 Future directions

Proteomics is a fascinating and quickly expanding field that promises to provide researchers with data about the proteome (the entire proteins present in the cell)[130,131]. Much like with the RNA-sequencing analysis, the changes in the proteome as the cell responds to treatment with RS1-208b will allow us to quickly identify the molecular pathway and the proteins involved in the execution of apoptosis. Despite the usefulness of transcriptome analysis, up-regulation in transcription does not necessarily result in an up-regulation in translation[131], making corroboration of results with proteomics important in identifying the major molecular players.

We have recently submitted RS1-208b treated and vehicle treated samples for proteomics analysis at the Biomolecule Analysis Core Facility (BACF) of the Border Biomedical Research Center (BBRC) at UTEP. We hope to be able to identify overexpressed (compared to vehicle control) proteins in the PERK-mediated UPR that had transcripts up-regulated in RS1-208b treated cells, thus, strengthening the argument for RS1-208b inducing apoptosis through proteotoxic stress. Moreover, proteomics analysis of Noxa expression should corroborate our Western blot data showing an increase in expression following treatment with RS1-208b.

Noxa's central role in cell death due to RS1-208b could be further explored to confirm the compound induces Noxa-dependent apoptosis. Evaluation of other proteotoxic stressors indicate transient silencing of Noxa expression using siRNAs attenuates apoptotic cell death[89].

Lastly, our Annexin V data implicated a non-apoptotic pathway of cell death that the ELISA assay for TNFα and the cytokine production inhibition[29] of RS1-208b suggest is not necrosis. Autophagy has garnered much interest lately and some of the up-regulated genes we observed in response to RS1-208b have been implicated in this form of cell death[66,85,103]. BAG3 (Bcl2 associated athanogene) has received attention as a gene that is important for the transition to autophagy and it is believed this transition occurs as a result of proteasome inhibition[132–134].

90

Though the mechanism is still being investigated, it seems that switch to autophagy results from the cell's attempts to degrade proteins that are normally degraded by the 26S proteasome and reduce proteotoxic stress[132,133]. By re-analyzing our transcriptome data and using the data we will obtain from the proteomics study, we might be able to contribute valuable insights into this switch to autophagy and help elucidate the molecular mechanism underlying the switch.

References

1. American Cancer Society. Global Cancer Facts & Figures 3rd Edition. *Am Cancer Soc*. 2015;(800):1-64. doi:10.1002/ijc.27711.

2. Bray F, Jemal A, Grey N, Ferlay J, Forman D. Global cancer transitions according to the Human Development Index (2008-2030): A population-based study. *Lancet Oncol*. 2012;13(8):790-801. doi:10.1016/S1470-2045(12)70211-5.

3. American Cancer Society. Cancer Facts & Figures for Hispanics/Latinos 2012-2014. *Am Cancer Soc*. 2012:40. http://www.cancer.org/research/cancerfactsfigures/cancerfactsfiguresforhispanicslatinos/cancer-facts-figures-hispanics-2012-2014.

4. Reynolds CP, Stallings DG, Knight AK, Hargrave KA, Phillips BU. Disparity in governmental cancer resource allocation between East and West Texas. *J Clin Oncol*. 29.

5. Schwartz CL. Long-term survivors of childhood cancer: the late effects of therapy. *Oncologist*. 1999;4(1):45-54. http://theoncologist.alphamedpress.org/content/4/1/45.full.

6. Ackler S, Mitten MJ, Chen J, et al. Navitoclax (ABT-263) and bendamustine +/- rituximab induce enhanced killing of non-Hodgkin's lymphoma tumours in vivo. *Br J Pharmacol*. 2012;167(4):881-891. doi:10.1111/j.1476-5381.2012.02048.x.

7. Lipshultz SE, Adams MJ, Colan SD, et al. Long-term cardiovascular toxicity in children, adolescents, and young adults who receive cancer therapy: Pathophysiology, course, monitoring, management, prevention, and research directions: A scientific statement from the American Heart Association. *Circulation*. 2013;128(17):1927-1955. doi:10.1161/CIR.0b013e3182a88099.

8. Shanmugam MK, Rane G, Kanchi MM, et al. *The Multifaceted Role of Curcumin in Cancer Prevention and Treatment*. Vol 20.; 2015. doi:10.3390/molecules20022728.

9. Kuttan R, Bhanumathy P, Nirmala K, George MC. Potential anticancer activity of turmeric (Curcuma longa). *Cancer Lett*. 1985;29(2):197-202. doi:10.1016/0304-3835(85)90159-4.

10. Devassy JG, Nwachukwu ID, Jones PJH. Curcumin and cancer: Barriers to obtaining a health claim. *Nutr Rev*. 2015;73(3):155-165. doi:10.1093/nutrit/nuu064.

11. Gupta SC, Prasad S, Kim JH, et al. Multitargeting by curcumin as revealed by molecular interaction studies. *Nat Prod Rep*. 2011;28(12):1937-1955.

12. Rahmani AH, Al Zohairy MA, Aly SM, Khan MA. Curcumin: A Potential Candidate in Prevention of Cancer via Modulation of Molecular Pathways. *Biomed Res Int*. 2014;2014(Figure 1). doi:10.1155/2014/761608.

13. Hasima N, Aggarwal BB. Cancer-linked targets modulated by curcumin. *Int J Biochem Mol Biol*. 2012;3(4):328-351.

14. Das L, Vinayak M. Curcumin attenuates carcinogenesis by down regulating proinflammatory cytokine interleukin-1 (IL-1?? and IL-1??) via modulation of AP-1 and NF-IL6 in lymphoma bearing mice. *Int Immunopharmacol*. 2014;20(1):141-147. doi:10.1016/j.intimp.2014.02.024.

15. Kewitz S, Volkmer I, Staege MS. Curcuma Contra Cancer? Curcumin and Hodgkin's Lymphoma. *Cancer Growth Metastasis*. 2013;6:35-52. doi:10.4137/CGM.S11113.

16. Zhou H, Beevers CS, Huang S. Targets of curcumin. *Curr Drug Targets*. 2011;12(3):332-347. doi:BSP/CDT/E-Pub/00185 [pii].

17. Bielak-Zmijewska A, Koronkiewicz M, Skierski J, Piwocka K, Radziszewska E, Sikora E.

Effect of curcumin on the apoptosis of rodent and human nonproliferating and proliferating lymphoid cells. *Nutr Cancer*. 2009;38(1):131-138.

18. Fan S, Xu Y, Li X, Tie L, Pan Y, Li X. Opposite angiogenic outcome of curcumin against ischemia and Lewis lung cancer models: In silico, in vitro and in vivo studies. *Biochim Biophys Acta - Mol Basis Dis*. 2014;1842(9):1742-1754. doi:10.1016/j.bbadis.2014.06.019.

19. Anand P, Kunnumakkara AB, Newman RA, et al. Bioavailability of Curcumin : Problems and Promises reviews Bioavailability of Curcumin : Problems and Promises. *Mol Pharm*. 2007;4(November):807-818. doi:10.1021/mp700113r.

20. Gupta SC, Patchva S, Aggarwal BB. Therapeutic roles of curcumin: lessons learned from clinical trials. *AAPS J*. 2013;15(1):195-218. doi:10.1208/s12248-012-9432-8.

21. Dhillon N, Aggarwal BB, Newman RA, et al. Phase II trial of curcumin in patients with advanced pancreatic cancer. *Clin Cancer Res*. 2008;14(14):4491-4499. doi:10.1158/1078-0432.CCR-08-0024.

22. Wang L, Shen Y, Song R, Sun Y, Xu J, Xu Q. An anticancer effect of curcumin mediated by down-regulating phosphatase of regenerating liver-3 expression on highly metastatic melanoma cells. *Mol Pharmacol*. 2009;76(6):1238-1245. doi:10.1124/mol.109.059105.

23. Palipoch S, Punsawad C, Koomhin P, Suwannalert P. Hepatoprotective effect of curcumin and alpha-tocopherol against cisplatin-induced oxidative stress. *BMC Complement Altern Med*. 2014;14(1):111. doi:10.1186/1472-6882-14-111.

24. Chan MM, Huang HI, Fenton MR, Fong D. In vivo inhibition of nitric oxide synthase gene expression by curcumin, a cancer preventive natural product with anti-inflammatory properties. *Biochem Pharmacol*. 1998;55(98):1955-1962. doi:10.1016/S0006-2952(98)00114-2.

25. Prasad S, Tyagi AK, Aggarwal BB. Recent developments in delivery, bioavailability, absorption and metabolism of curcumin: The golden pigment from golden spice. *Cancer Res Treat*. 2014;46(1):2-18. doi:10.4143/crt.2014.46.1.2.

26. Yallapu MM, Khan S, Maher DM, et al. Anti-cancer activity of curcumin loaded nanoparticles in prostate cancer. *Biomaterials*. 2014;35(30):8635-8648. doi:10.1016/j.biomaterials.2014.06.040.

27. Yin HT, Zhang D geng, Wu X li, Huang XE, Chen G. In vivo evaluation of curcumin-loaded nanoparticles in a A549 xenograft mice model. *Asian Pacific J Cancer Prev*. 2013;14(1):409-412. doi:10.7314/APJCP.2013.14.1.409.

28. Santiago-vázquez Y, Das U, Varela-ramirez A, et al. Tumor-selective Cytotoxicity of a Novel Pentadiene Analogue on Human Leukemia / lymphoma Cells. 2016;(Cll):1-9. doi:10.2174/2212697X0366616083016.

29. Wu J, Zhang Y, Cai Y, et al. Discovery and evaluation of piperid-4-one-containing mono-carbonyl analogs of curcumin as anti-inflammatory agents. *Bioorganic Med Chem*. 2013;21(11):3058-3065. doi:10.1016/j.bmc.2013.03.057.

30. Thakur A, Manohar S, Velez Gerena CE, et al. Novel 3,5-bis(arylidiene)-4-piperidone based monocarbonyl analogs of curcumin: anticancer activity evaluation and mode of action study. *Medchemcomm*. 2014;5:576-586. doi:10.1039/C3MD00399J.

31. Wu J, Cai Z, Wei X, et al. Anti-lung cancer activity of the curcumin analog JZ534 in vitro. *Biomed Res Int*. 2015;2015. doi:10.1155/2015/504529.

32. Mosley CA, Liotta DC, Snyder JP. Highly active anticancer curcumin analogues. *Adv Exp Med Biol*. 2007;595:77-103. doi:10.1007/978-0-387-46401-5-2.

93

33. Liu H, Liang Y, Wang L, et al. In Vivo and In Vitro Suppression of Hepatocellular Carcinoma by EF24, a Curcumin Analog. *PLoS One*. 2012;7(10). doi:10.1371/journal.pone.0048075.

34. Thomas SL, Zhong D, Zhou W, et al. EF24, a novel curcumin analog, disrupts the microtubule cytoskeleton and inhibits HIF-1. *Cell Cycle*. 2008;7(15):2409-2417. doi:6410 [pii].

35. Aravindan S, Natarajan M, Awasthi V, Herman TS, Aravindan N. Novel Synthetic Monoketone Transmute Radiation-Triggered NF??B-Dependent TNF?? Cross-Signaling Feedback Maintained NF??B and Favors Neuroblastoma Regression. *PLoS One*. 2013;8(8):1-12. doi:10.1371/journal.pone.0072464.

36. Zhao C, Yang J, Wang Y, et al. Synthesis of mono-carbonyl analogues of curcumin and their effects on inhibition of cytokine release in LPS-stimulated RAW 264.7 macrophages. *Bioorganic Med Chem*. 2010;18(7):2388-2393. doi:10.1016/j.bmc.2010.03.001.

37. Jha A, Duffield KM, Ness MR, et al. Curcumin-inspired cytotoxic 3,5-bis(arylmethylene)-1-(N-(ortho-substituted aryl)maleamoyl)-4-piperidones: A novel group of topoisomerase II alpha inhibitors. *Bioorganic Med Chem*. 2015;23(19):6404-6417. doi:10.1016/j.bmc.2015.08.023.

38. Tan K-L, Ali A, Du Y, et al. Synthesis and evaluation of bisbenzylidenedioxotetrahydrothiopranones as activators of endoplasmic reticulum (ER) stress signaling pathways and apoptotic cell death in acute promyelocytic leukemic cells. *J Med Chem*. 2014;57(14):5904-5918. doi:10.1021/jm401352a.

39. Reid JM, Buhrow SA, Gilbert JA, et al. Mouse pharmacokinetics and metabolism of the curcumin analog, 4-Piperidione,3,5-bis[(2-fluorophenyl)methylene]-acetate(3E,5E) (EF-24; NSC 716993). *Cancer Chemother Pharmacol*. 2014;73(6):1137-1146.

40. Buttke T, McCubrey J, Owen T. Use of an aqueous soluble tetrazolium/formazan assay to measure viability and proliferation of lymphokine-dependent cell lines. *J Immunol Methods*. 1993;157(1-2):233-240.

41. Barridge M, Tan A. Characterization of the cellular reduction of 3-(4,5-dimethylthiazol-2-yl)-2,5-diphenyltetrazolium bromide (MTT): Subcellular localization, substrate dependence, and involvement of mitochondrial electron transport in MTT reduction. *Arch Biochem Biophys*. 1993;303:474-482.

42. Chavan Ravindranath A, Perualila-Tan N, Adetayo K, et al. Connecting Gene Expression Data from Connectivity Map and In Silico Target Predictions For Small Molecule Mechanism-of-Action Analysis. *Mol BioSyst*. 2014;11(1):86-96. doi:10.1039/C4MB00328D.

43. Suzuki T, Fujikura K, Higashiyama T, Takata K. DNA staining for fluorescence and laser confocal microscopy. *J Histochem Cytochem*. 1997;45(1):49-53. doi:10.1177/002215549704500107.

44. Elmore S. Apoptosis: a review of programmed cell death. *Toxicol Pathol*. 2007;35(4):495-516. doi:10.1080/01926230701320337.

45. Taylor RC, Cullen SP, Martin SJ. Apoptosis: controlled demolition at the cellular level. *Nat Rev Mol Cell Biol*. 2008;9(3):231-241. doi:10.1038/nrm2312.

46. Hannah M. Hankins, Ryan D. Baldridge, Peng Xu TRG. Role of flippases, scramblases, and transfer proteins in phophatidylserine subcellular distribution. *Traffic*. 2015;16(1):35-47. doi:10.1126/scisignal.2001449.Engineering.

47. Fadok V a, Bratton DL, Frasch SC, Warner ML, Henson PM. The role of

94

phosphatidylserine in recognition of apoptotic cells by phagocytes. *Cell Death Differ*. 1998;5(7):551-562. doi:10.1038/sj.cdd.4400404.

48. Armstrong A, Ravichandran KS. Phosphatidylserine receptors: what is the new RAGE? *EMBO Rep*. 2011;12(4):287-288. doi:10.1038/embor.2011.41.

49. Parsons MJ, Green DR. Mitochondria in cell death. *Essays Biochem Essays Biochem*. 2010;47(47):99-114. doi:10.1042/BSE0470099.

50. Xiong S, Mu T, Wang G, Jiang X. Mitochondria-mediated apoptosis in mammals. *Protein Cell*. 2014;5(10):737-749. doi:10.1007/s13238-014-0089-1.

51. Slee EA, Harte MT, Kluck RM, et al. Ordering the Cythochrome-c-initiated Caspase Cascade: Hierarchical Activation of Caspases-2, -3, -6, -7, -8, and -10 in Caspase-9-dependent Manner. *J Cell Biol*. 1999;144(2):281-292.

52. Sundquist T, Moravec R, Niles A, O'Brien M, Riss T, Corporation P. Timing your apoptosis assays. *Protoc Appl Guid*. 2006;(16):18-21. www.promega.com/paguide/chap3.html.

53. Morgan MJ, Kim Y-S, Liu Z. TNFalpha and reactive oxygen species in necrotic cell death. *Cell Res*. 2008;18(3):343-349. doi:10.1038/cr.2008.31.

54. de Bruin EC, Medema JP. Apoptosis and non-apoptotic deaths in cancer development and treatment response. *Cancer Treat Rev*. 2008;34(8):737-749. doi:10.1016/j.ctrv.2008.07.001.

55. Zhang JD, Schindler T, Küng E, Ebeling M, Certa U. Highly sensitive amplicon-based transcript quantification by semiconductor sequencing. *BMC Genomics*. 2014;15(1):565. doi:10.1186/1471-2164-15-565.

56. Li W, Turner A, Aggarwal P, et al. Comprehensive evaluation of AmpliSeq transcriptome, a novel targeted whole transcriptome RNA sequencing methodology for global gene expression analysis. *BMC Genomics*. 2015;16:1069. doi:10.1186/s12864-015-2270-1.

57. Reichard JF, Motz GT, Puga A. Heme oxygenase-1 induction by NRF2 requires inactivation of the transcriptional repressor BACH1. *Nucleic Acids Res*. 2007;35(21):7074-7086. doi:10.1093/nar/gkm638.

58. Joo JH, Ueda E, Bortner CD, Yang XP, Liao G, Jetten AM. Farnesol activates the intrinsic pathway of apoptosis and the ATF4-ATF3-CHOP cascade of ER stress in human T lymphoblastic leukemia Molt4 cells. *Biochem Pharmacol*. 2015;97(3):256-268. doi:10.1016/j.bcp.2015.08.086.

59. Dang C V. MYC on the path to cancer. *Cell*. 2012;149(1):22-35. doi:10.1016/j.cell.2012.03.003.

60. Lüscher B, Vervoorts J. Regulation of gene transcription by the oncoprotein MYC. *Gene*. 2012;494(2):145-160. doi:10.1016/j.gene.2011.12.027.

61. Matthew Thompson, Dakang Xu BRGW. ATF3 transcription factor and its emerging role in immunity and cancer. *J Mol Med*. 2009;87(11):1053-1060. doi:10.1007/s00109-009-0520-x.ATF3.

62. Oakes S a, Papa FR. The Role of Endoplasmic Reticulum Stress in Human Pathology. *Annu Rev Pathol*. 2014;(October 2014):173-194. doi:10.1146/annurev-pathol-012513-104649.

63. Hedge RS, Ploegh HL. Quality and Quantity Control at the Endoplasmic Reticulum. *Curr Opin Cell Biol*. 2010;22(4):437-446.

64. Ma Y, Hendershot LM. ER chaperon functions during normal and stress conditions. *J Chem Neuroanat*. 2004;28(1-2):51-65.

65. Meusser B, Hirsch C, Jarosch E, Sommer T. ERAD: the long road to destruction. *Nat Cell Biol*. 2005;7:766-772.

66. Cybulsky A V. The intersecting roles of endoplasmic reticulum stress, ubiquitin-proteasome system, and autophagy in the pathogenesis of proteinuric kidney disease. *Kidney Int*. 2013;84(1):25-33. doi:10.1038/ki.2012.390.

67. Tabas I, Ron D. Integrating the mechanism of apoptosis induced by endoplasmic reticulum stress. *Nat Cell Biol*. 2011;13:184-190.

68. Teske BF, Fusakio ME, Zhou D, et al. CHOP induces activating transcription factor 5 (ATF5) to trigger apoptosis in response to perturbations in protein homeostasis. *Mol Biol Cell*. 2013;24(15):2477-2490. doi:10.1091/mbc.E13-01-0067.

69. Sano R, Reed JC. ER stress-induced cell death mechanisms. *Biochim Biophys Acta - Mol Cell Res*. 2013;1833(12):3460-3470. doi:10.1016/j.bbamcr.2013.06.028.

70. Bi M, Naczki C, Koritzinsky M, et al. *Endoplasmic Reticulum Stress in Malignancy*. Vol 35.; 2013. doi:10.1016/B978-0-12-407704-1.00005-1.Endoplasmic.

71. Walter P, Ron D. The Unfolded Protein Response: From Stress Pathway to Homeostatic Regulation. *Science (80-)*. 2011;334(6059):1081-1086.

72. Yoneda T, Urano F, Ron D. Transmission of proteotoxicity across cellular compartments. *Genes Dev*. 2002;16(11):1307-1313. doi:10.1101/gad.1000902.

73. Bravo R, Parra V, Gatica D, et al. Endoplasmic Reticulum and the Unfolded Protein Response: Dynamics and Metabolic Integration. *Int Rev Cell Mol Biol*. 2013;301:215-290.

74. Ri M. Endoplasmic-reticulum stress pathway-associated mechanisms of action of proteasome inhibitors in multiple myeloma. *Int J Hematol*. 2016;104(3):273-280. doi:10.1007/s12185-016-2016-0.

75. Chakrabarti A, Chen AW, Varner JD. A review of the Mammalian Unfoded Protein Response. *Biotechnol Bioeng*. 2012;108(12):2777-2793. doi:10.1002/bit.23282.A.

76. Donnelly N, Gorman AM, Gupta S, Samali A. The eIF2?? kinases: Their structures and functions. *Cell Mol Life Sci*. 2013;70(19):3493-3511. doi:10.1007/s00018-012-1252-6.

77. Rajesh K, Krishnamoorthy J, Kazimierczak U, et al. Phosphorylation of the translation initiation factor eIF2α at serine 51 determines the cell fate decisions of Akt in response to oxidative stress. *Cell Death Dis*. 2015;6(1):e1591. doi:10.1038/cddis.2014.554.

78. Wek RC, Jiang H-Y, Anthony TG. Coping with stress: eIF2 kinases and translational control. *Biochem Soc Trans*. 2006;34(Pt 1):7-11. doi:10.1042/BST20060007.

79. Armstrong JL, Flockhart R, Veal GJ, Lovat PE, Redfern CPF. Regulation of endoplasmic reticulum stress-induced cell death by ATF4 in neuroectodermal tumor cells. *J Biol Chem*. 2010;285(9):6091-6100. doi:10.1074/jbc.M109.014092.

80. Hai T, Hartman MG. The molecular biology and nomenclature of the activating transcription factor/cAMP responsive element binding family of transcription factors: activating factor proteins and homeostasis. *Gene*. 2001;273(1):1-11.

81. Albert M-C, Brinkmann K, Kashkar H. Noxa and cancer therapy. *Mol Cell Oncol*. 2014;1(1):e29906. doi:10.4161/mco.29906.

82. Ploner C, Kofler R, Villunger A. Noxa: at the tip of the balance between life and death. *Oncogene*. 2008;27(Suppl 1):S84-S92. doi:10.1038/onc.2009.46.

83. Willis SN, Chen L, Dewson G, et al. Proapoptotic Bak is sequestered by Mcl-1 and Bcl-xL, but not Bcl-2, until displaced by BH3-only proteins. *Genes Dev*. 2005;19(11):1294-1305.

84. Nakajima W, Hicks M a, Tanaka N, Krystal GW, Harada H. Noxa determines localization

and stability of MCL-1 and consequently ABT-737 sensitivity in small cell lung cancer. *Cell Death Dis*. 2014;5(2):e1052. doi:10.1038/cddis.2014.6.

85. Liu YL, Lai F, Wilmott JS, et al. Noxa upregulation by oncogenic activation of MEK/ERK through CREB promotes autophagy in human melanoma cells. *Oncotarget*. 2014;5(22):11237-11251. http://www.pubmedcentral.nih.gov/articlerender.fcgi?artid=4294377&tool=pmcentrez&rendertype=abstract.

86. Aikawa T, Shinzawa K, Tanaka N, Tsujimoto Y. Noxa is necessary for hydrogen peroxide-induced caspase-dependent cell death. *FEBS Lett*. 2010;584(4):681-688. doi:10.1016/j.febslet.2010.01.026.

87. Verfaillie T, van Vliet A, Garg AD, et al. Pro-apoptotic signaling induced by photo-oxidative ER stress is amplified by Noxa, not Bim. *Biochem Biophys Res Commun*. 2013;438(3):500-506. doi:10.1016/j.bbrc.2013.07.107.

88. Baou M, Kohlhaas SL, Butterworth M, et al. Role of noxa and its ubiquitination in proteasome inhibitor-induced apoptosis in chronic lymphocytic leukemia cells. *Haematologica*. 2010;95(9):1510-1518. doi:10.3324/haematol.2010.022368.

89. Davis AL, Qiao S, Lesson JL, et al. The Quinone Methide Aurin Is a Heat Shock Response Inducer That Causes Proteotoxic Stress and Noxa-dependent Apoptosis in Malignant Melanoma Cells *. *J Biol Chem*. 2015;290(3):1623-1638. doi:10.1074/jbc.M114.592626.

90. Ploner C, Kofler R, Villunger a. Noxa: at the tip of the balance between life and death. *Oncogene*. 2008;27(Suppl 1):S84-S92. doi:10.1038/onc.2009.46.

91. Lamb J, Crawford ED, Peck D, et al. The Connectivity Map : Using Gene-Expression Signatures to Connect Small Molecules, Genes, and Disease. *Science (80-)*. 2006;313(September):1929-1935. doi:10.1126/science.1132939.

92. Jüllig M, Zhang W V., Ferreira A, Stott NS. MG132 induced apoptosis is associated with p53-independent induction of pro-apoptotic Noxa and transcriptional activity of ??-catenin. *Apoptosis*. 2006;11(4):627-641. doi:10.1007/s10495-006-4990-9.

93. Park HS, Jun DY, Han CR, Woo HJ, Kim YH. Proteasome inhibitor MG132-induced apoptosis via ER stress-mediated apoptotic pathway and its potentiation by protein tyrosine kinase p56 lck in human Jurkat T cells. *Biochem Pharmacol*. 2011;82(9):1110-1125. doi:10.1016/j.bcp.2011.07.085.

94. Guo N, Peng Z. MG132, a proteasome inhibitor, induces apoptosis in tumor cells. *Asia Pac J Clin Oncol*. 2012;9(1):6-11.

95. Frase H, Hudak J, Lee I. Identification of the Proteasome Inhibitor MG262 as a Potent ATP-Dependent Inhibitor of the Salmonella enterica serovar Typhimurium Lon Protease. *Biochemistry*. 2006;45(27):8264-8274.

96. Hammadi M, Oulidi A, Gackiere F, et al. Modulation of ER stress and apoptosis by endoplasmic reticulum calcium leak via translocon during unfolded protein response: involvement of GRP78. *FASEB J*. 2013;27(4):1600-1609.

97. Su R-Y, Chi K-H, Huang D-Y, Tai M-H, Lin W-W. 15-deoxy-Δ12,14-prostaglandin J2 up-regulates death receptor 5 gene expression in HCT116 cells: involvement of reactive oxygen species and C/EBP homologous transcription factor gene transcription. *Mol Cancer Ther*. 2008;7(10):3429-3440.

98. Zhao X, Liu X, Su L. Parthenolide induces apoptosis via TNFRSF10B and PMAIP1 pathways in human lung cancer cells. *J Exp Clin Cancer Res*. 2014;33(3).

97

99. Han SS, Son DJ, Yun H, Kamberos NL, Janz S. Piperlongumine inhibits proliferation and survival of Burkitt lymphoma in vitro. *Leuk Res*. 2013;37(2):146-154. doi:10.1016/j.leukres.2012.11.009.

100. Jarvius M, Fryknäs M, D'Arcy P, et al. Piperlongumine induces inhibition of the ubiquitin-proteasome system in cancer cells. *Biochem Biophys Res Commun*. 2013;431(2):117-123. doi:10.1016/j.bbrc.2013.01.017.

101. Kim TH, Song J, Kim S-H, et al. Piperlongumine treatment inactivates peroxiredoxin 4, exacerbates endoplasmic reticulum stress, and preferentially kills high-grade glioma cells. *Neuro Oncol*. 2014;16(10):1354-1364.

102. Huang H, Liao Y, Liu N, et al. Two clinical drugs deubiquitinase inhibitor auranofin and aldehyde dehydrogenase inhibitor disulfiram trigger synergistic anti-tumor effects in vitro and in vivo. *Oncotarget*. 2016;7(3):2796-2808.

103. Liu B, Wen X, Cheng Y. Survival or death: disequilibrating the oncogenic and tumor suppressive autophagy in cancer. *Cell Death Dis*. 2013;4.

104. Feng L, Zhang D, Fan C, et al. ER stress-mediated apoptosis induced by celastrol in cancer cells and important role of glycogen synthase kinase-3B in the signal network. *Cell Death Dis*. 2013;4.

105. Badr CE, Wurdinger T, Nilsson J, et al. Lanatoside C sensitizes glioblastoma cells to tumor necrosis factor-related apoptosis-inducing ligand and induces an alternative cell death pathway. *Neuro Oncol*. 2011;13(11):1213-1224.

106. Choi MJ, Park EJ, Min KJ, Park J-W, Kwon TK. Endoplasmic reticulum stress mediates withaferin A-induced apoptosis in human renal carcinoma cells. *Toxicol Vitr*. 2011;25(3):692-698.

107. Mayer MP, Bukau B. Hsp70 chaperones: Cellular functions and molecular mechanism. *Cell Mol Life Sci*. 2005;62(6):670-684. doi:10.1007/s00018-004-4464-6.

108. Menéndez-Benito V, Verhoef LGGC, Masucci MG, Dantuma NP. Endoplasmic reticulum stress compromises the ubiquitin-proteasome system. *Hum Mol Genet*. 2005;14(19):2787-2799. doi:10.1093/hmg/ddi312.

109. Pérez-Galán P, Roue G, Villamor N, Montserrat E, Campo E, Colomer D. The proteasome inhibitor bortezomib induces apoptosis in mantle-cell lymphoma through generation of ROS and Noxa activation independent of p53 status. *Blood*. 2006;107(1):257-264. doi:10.1182/blood-2005-05-2091.

110. Sung B, Kunnumakkara AB, Sethi G, Anand P, Guha S, Aggarwal BB. Curcumin circumvents chemoresistance in vitro and potentiates the effect of thalidomide and bortezomib against human multiple myeloma in nude mice model. *Mol Cancer Ther*. 2009;8(4):959-970. doi:10.1158/1535-7163.MCT-08-0905.

111. Livneh I, Cohen-Kaplan V, Cohen-Rosenzweig C, Avni N, Cierchanover A. The life cycle of the 26S proteasome: from birth, through regulation and function, and onto its death. *Cell Res*. 2016;26:869-885.

112. D'Arcy P, Brnjic S, Olofsson MH, et al. Inhibition of proteasome deubiquitinating activity as a new cancer therapy. *Nat Med*. 2011;17(12):1636-1640. doi:10.1038/nm.2536.

113. Wang X, Stafford W, Mazurkiewicz M, et al. The 19S Deubiquitinase inhibitor b-AP15 is enriched in cells and elicits rapid commitment to cell death. *Mol Pharmacol*. 2014;85(6):932-945. doi:10.1124/mol.113.091322.

114. Chitta K, Paulus A, Akhtar S, et al. Targeted inhibition of the deubiquitinating enzymes, USP14 and UCHL5, induces proteotoxic stress and apoptosis in Waldenstr??m

macroglobulinaemia tumour cells. *Br J Haematol*. 2015;169(3):377-390. doi:10.1111/bjh.13304.

115. VanderLinden RT, Hemmis CW, Schmitt B, et al. Structural Basis for the Activation and Inhibition of the UCH37 Deubiquitylase. *Mol Cell*. 2015;57(5):901-911. doi:10.1016/j.molcel.2015.01.016.

116. Tushar K. Maiti, Michelle Permaul, David A. Boudreaux, Christina Mahanic S, Mauney and C Das. Crystal structure of the catalytic domain of UCHL5, a proteasome-associated human deubiquitinating enzyme, reveals an unproductive form of the enzyme. 2012;100(2):130-134. doi:10.1016/j.pestbp.2011.02.012.Investigations.

117. Lee JH, Shin SK, Jiang Y, et al. Facilitated Tau Degradation by USP14 Aptamers via Enhanced Proteasome Activity. *Sci Rep*. 2015;5:10757. doi:10.1038/srep10757.

118. Wang X, D'Arcy P, Caulfield TR, et al. Synthesis and Evaluation of Derivatives of the Proteasome Deubiquitinase Inhibitor b-AP15. *Chem Biol Drug Des*. 2015;86(5):1036-1048. doi:10.1111/cbdd.12571.

119. Lowman XH, McDonnell MA, Kosloske A, et al. The Proapoptotic Function of Noxa in Human Leukemia Cells Is Regulated by the Kinase Cdk5 and by Glucose. *Mol Cell*. 2010;40(5):823-833. doi:10.1016/j.molcel.2010.11.035.

120. Bosma MJ, Carroll AM. The SCID mouse mutant: definition, characterization, and potential uses. *Annu Rev Immunol*. 1991;9:323-350. doi:10.1146/annurev.iy.09.040191.001543.

121. Blase L, Daniel PT, Koretz K, Schwartz-Albiez R, Moller P. The capacity of human malignant B-lymphocytes to disseminate in scid mice is correlated with functional expression of the fibronectin receptor α5β1 (CD49E/CD29). *Int J Cancer*. 1995;60(6):860-866.

122. Daniel D, Yang B, Lawrence D a, et al. Cooperation of the proapoptotic receptor agonist rhApo2L / TRAIL with the CD20 antibody rituximab against non-Hodgkin lymphoma xenografts Cooperation of the proapoptotic receptor agonist rhApo2L / TRAIL with the CD20 antibody rituximab against non-Hodgkin. *Heal (San Fr*. 2008;110(12):4037-4046. doi:10.1182/blood-2007-02-076075.

123. Manders JMB, Postema EJ, Corstens FHM, Boerman OC. Enhancing tumor implantation and growth rate of Ramos B-cell lymphoma in nude mice. *Comp Med*. 2002;52(1):36-38.

124. Zauli G, Corallini F, Zorzet S, Grill V, Marzari R, Secchiero P. In vivo anti-lymphoma activity of an agonistic human recombinant anti-TRAIL-R2 minibody. *Invest New Drugs*. 2012;30:405-407. doi:10.1007/s10637-010-9519-y.

125. Bosch R, Moreno MJ, Dieguez-Gonzalez R, et al. Subcutaneous passage increases cell aggressiveness in a xenograft model of diffuse large B cell lymphoma. *Clin & Exp metastasis*. 2012;29(4):339-347. doi:10.1007/s10585-012-9454-8.

126. Lammers T, Peschke P, Kühnlein R, et al. Effect of intratumoral injection on the biodistribution and the therapeutic potential of HPMA copolymer-based drug delivery systems. *Neoplasia*. 2006;8(10):788-795. doi:10.1593/neo.06436.

127. Pellegrini G, Starkey Lewis PJ, Palmer L, et al. Intraperitoneal administration of high doses of polyethylene glycol (PEG) causes hepatic subcapsular necrosis and low-grade peritonitis with a rise in hepatic biomarkers. *Toxicology*. 2013;314(2-3):262-266. doi:10.1016/j.tox.2013.06.003.

128. Fruijtier-Pölloth C. Safety assessment on polyethylene glycols (PEGs) and their derivatives as used in cosmetic products. *Toxicology*. 2005;214(1-2):1-38.

doi:10.1016/j.tox.2005.06.001.

129. Mach CM, Mathew L, Mosley SA, Kurzrock R, Smith JA. Determination of minimum effective dose and optimal dosing schedule for liposomal curcumin in a xenograft human pancreatic cancer model. *Anticancer Res*. 2009;29(6):1895-1899. doi:29/6/1895 [pii].

130. Larance M, Lamond AI. Multidimensional proteomics for cell biology. *Nat Rev Mol Cell Biol*. 2015;16(5):269-280. doi:10.1038/nrm3970.

131. Vogel C, Marcotte EM. Insights into regulation of protein abundance from proteomics and transcriptomis analyses. *Nat Rev Genet*. 2013;13(4):227-232. doi:10.1038/nrg3185.Insights.

132. Minoia M, Boncoraglio A, Vinet J, et al. BAG3 induces the sequestration of proteasomal clients into cytoplasmic puncta Implications for a proteasome-to-autophagy switch. *Autophagy*. 2014;10(9):1603-1621. doi:10.4161/auto.29409.

133. Liu BQ, Du ZX, Zong ZH, et al. BAG3-dependent noncanonical autophagy induced by proteasome inhibition in HepG2 cells. *Autophagy*. 2013;9(6):905-916. doi:10.4161/auto.24292.

134. Doong H, Rizzo K, Fang S, Kulpa V, Weissman AM, Kohn EC. CAIR-1/BAG-3 abrogates heat shock protein-70 chaperone complex-mediated protein degradation. Accumulation of poly-ubiquitinated Hsp90 client proteins. *J Biol Chem*. 2003;278(31):28490-28500. doi:10.1074/jbc.M209682200.

135. Kang MH, Wang J, Makena MR, et al. Activity of MM-398, nanoliposomal irinotecan (nal-IRI), in Ewing's family tumor xenografts is associated with high exposure of tumor to drug and high SLFN11 expression. *Clin Cancer Res*. 2015;21(5):1139-1150. doi:10.1158/1078-0432.CCR-14-1882.

Glossary

*	$p < 0.05$
**	$p < 0.005$
ACTB	Beta-actin
AIDS	Acquired Immune Deficiency Syndrome
Akt	Protein Kinase B
ALL	Acute Lymphoblastic Leukemia
AML	Acute Myeloid Leukemia
ATF3	Activating Transcription Factor 3
ATF4	Activating Transcription Factor 4
ATF6	Activating Transcription Factor 6
ATP	Adenosine Triphosphate
BACF	Biomolecule Analysis Core Facility
BAG3	BCL2 Associated Athanogene 3
BBRC	Border Biomedical Research Center
BCL2	B-cell Lymphoma 2
BH3	Bcl2 Homology Domain 3
BiP	Binding Immunoglobulin Protein
BL	Burkitt's Lymphoma
BSA	Bovine Serum Albumin
bZIP	Basic Leucine Zipper Domain
cMAP	Connectivity Map
Contraction	Definition
CPRIT	Cancer Prevention Research Institute of Texas
DAPI	4',6-diamidino-2-phenylindole, dihydrochloride
DMSO	Dimethyl Sulfoxide
DOD	Department of Defense
DUB	Deubiquitinase
E1	Ubiquitin Activating Enzyme
E2	Ubiquitin Conjugating Enzyme
E3	Ubiquitin Ligase
eIF2α	Eukariotic Initiation Factor 2α
ELISA	Enzyme-Linked Immunosorbent Assay
ER	Endoplasmic Reticulum
ERAD	ER Associated Degradation
FITC	Fluorescein isothiocyanate
GADD34	Growth Arrest and DNA Damage-Inducible Protein 34
GAPDH	Glyceraldehyde 3-phosphate dehydrogenase
GDP	Guanosine Diphosphate
GO	Gene Ontology
GTP	Guanosine Triphosphate
HMOX1	Heme Oxygenase 1

IC50	Inhibitory Concentration
IL-6	Interleukin-6
IP	Intraperitoneal
IRE1α	Inositol Requiring Enzyme 1α
IT	Intratumoral
JAK/STAT	Janus Kinase/Signal Transducers and Activators of Transcription
JC-1	5',6,6'-tetrachloro-1,1',3,3'-tetraethylbenzimidazolylcarbocyanine iodide
MAPK	Mitogen-Activated Protein Kinase
MCL-1	Myeloid Cell Leukemia 1
MTS	3-(4,5-dimethylthiazol-2-yl)-5-(3-carboxymethoxyphenyl)-2-(4-sulfophenyl)-2H-tetrazolium, inner salt
MYC	c-MYC
NADH	Nicotinamide adenine dinucleotide
NADPH	Nicotinamide adenine dinucleotide phosphate
NCI	National Cancer Institute
NF-kB	Nuclear Factor kB
NGS	Next Generation Sequencing
NHL	Non-Hodgkin's Lymphoma
ORF	Open Reading Frame
PAGE	Polyacrylamide gel electrophoresis
PBMC	Peripheral Blood Mononuclear Cells
PBS	Phosphate Buffered Saline
PEG-400	Polyethylene Glycol 400
PERK	PKR-like ER Kinase
PMAIP1	Phorbol-12-Myristate-13-Acetate Induced Protein 1
PMS	Phenazine Methosulfate
POH1	RPN11, a Ubiquitin C-Terminal Hydrolase
proteostasis	Protein Homeostasis
PS	Phosphatidylserine
PVDF	Polyvinylidene Fluoride
RT-qPCR	Real-Time Quantitative Reverse Transcription
SCID	Severe Compromised Immuno-Deficient
SDS	sodium dodecyl sulfate
SI	Selectivity Index
SQ	Subcutaneous
TBS	Tris Buffered Saline
TBST	Tris Buffered Saline (0.1% Tween-20)
TNFα	Tumor Necrosis Factor-α
UCHL5	Ubiquitin C-Terminal Hydrolase L5
uORF	Upstream Open Reading Frame
UPR	Unfolded Protein Response
UPS	Ubiquitin-Proteasome System
USP14	Ubiquitin Specific Peptidase 14

UTEP   The University of Texas at El Paso
XBP1   X-Box Protein 1

Vita

Ruben was born in El Paso and graduated from Del Valle High School in 2006. He spent the next four years as an Ehrlich Scholar at Brown University, earning his B.A. in Human Biology in 2010. During his undergraduate career, Ruben was heavily involved in Latino organizations, serving as a mentor to fellow undergraduates through the Connexiones program and M.E.Ch.A. de Brown, where he served as Chair (2008-2009). After graduating, Ruben worked under the direction of C. Pat Reynolds, MD, PhD., at the Texas Tech Health Sciences Cancer Center from 2011-2014, where he participated in the establishment of patient derived cell lines and xenografts as well as research experiments testing novel compounds and chemotherapy combinations[135]. Ruben matriculated to the graduate school at UTEP in the fall of 2014. He will be submitting his research work for publication in the fall of 2016 and hopes it will be accepted and published by the end of 2017.